Multiple light scattering in random discrete media

Coherent backscattering and imaging

Gedrukt bij: Optima Druk, Molenaarsgraaf

Multiple light scattering in random discrete media

Coherent backscattering and imaging

Academisch proefschrift

ter verkrijging van de graad van doctor
aan de Universiteit van Amsterdam op gezag van
de Rector Magnificus prof. dr P.W.M. de Meijer
ten overstaan van een door het college van dekanen
ingestelde commissie in het openbaar te verdedigen
in de Aula der Universiteit
op maandag 15 mei 1995 te 15.30 uur.

door

Peter Niels den Outer

geboren te Nijmegen

Amsterdam 1995

Promotor:	Prof. dr. A. Lagendijk
Commissie:	Prof. dr. J.W. Hovenier
	Prof. dr. J.A. van Paradijs
	Prof. dr. J.T.M. Walraven
	Dr. M.P. van Albada
	Dr. W.L. Vos

Faculteit der Natuur- en Sterrenkunde

The work described in this thesis was part of the research program
of the 'Stichting voor Fundamenteel Onderzoek der Materie (FOM)',
which is financially supported by the
'Nederlandse Organisatie voor Wetenschappelijk Onderzoek (NWO)',
and carried out at the

Van der Waals-Zeeman Laboratorium
Universiteit van Amsterdam
Valcknierstraat 65-67
1018 XE Amsterdam
The Netherlands

where a number of copies of this thesis are available.

Contents

Chapter 1

Introduction

1.1 A strongly scattering medium

Light impinging on a random discrete medium will be multiply scattered. Multiple scattering means more than once to a few *thousand* times typically. In a random discrete medium the scattering is caused by particles that can be located at a random position or scatter with a random efficiency. Examples of strongly scattering media in everyday life are milk, fog, snow etc. In fact, everything that appears white is a strongly scattering medium. A scattering medium usually consists of a mixture of two or more non-absorbent transparent materials (water and air for instance). Scattering of light occurs because the indices of refraction of the transparent materials differ, and *multiple* scattering occurs because the average distance between two scattering events is much smaller than the dimensions of the medium. If one of the materials absorbs the light, the medium will be grey, or coloured if the absorption is restricted to a particular wavelength range. A nice example of an absorbent multiply scattering medium is blood.

In order to have multiple scattering in the sense as aforementioned, the fraction of absorbed light per scattering event must be extremely small (say $<10^{-5}$). For instance, the silver grains that absorb only a few percent per scattering event, produce already a black region on a photo. Absorption will be of minor importance in the systems that are studied in this thesis.

The only relevant length scale in a non-absorbent multiply scattering medium is the mean-free path. The mean-free path is the average distance between two successive scattering events, and tells us, for instance, how far one can see into the fog; i.e. one mean-free path.

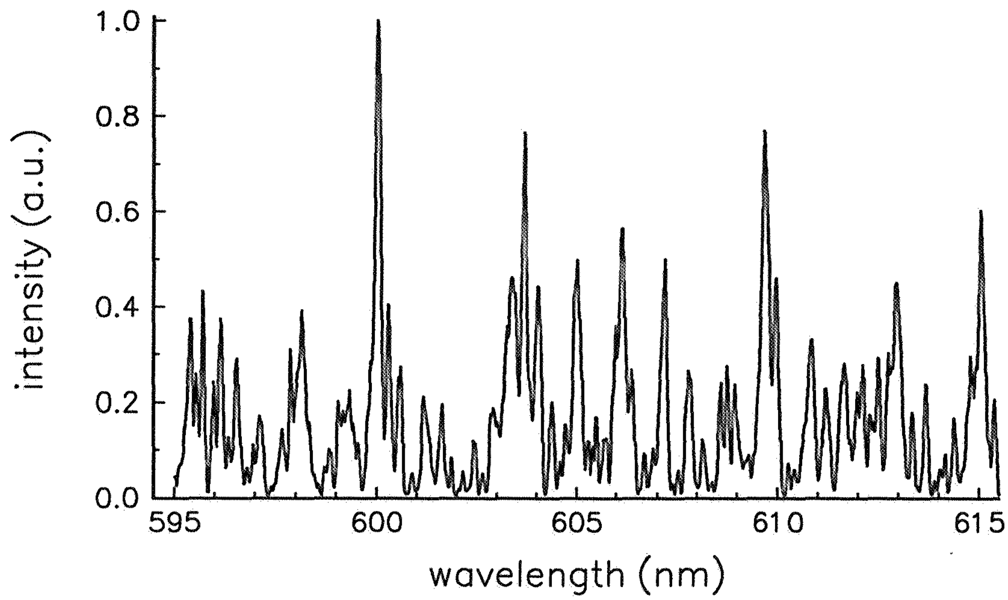

Figure 1: Transmitted intensity scattered in a small solid angle as a function of the wavelength of the light. Sample: TiO_2-particles, average size: 270 nm, thickness sample: 14 μm.

1.2 Interference

The light inside a strongly scattering medium is subject to a large number of scattering events. It therefore diffuses through the medium and a lot of experimental observations of multiply scattered light can be understood by the use of a diffusion model. Still, interference can play a significant role in the properties of the multiply scattered light. Moreover, in particular situations, interference causes a drastic change on the transport properties of light through these scattering media.

1.2.1 Speckle

If one shines monochromatic coherent light on a medium with scatterers fixed at random positions, one will observe a speckle pattern.[1]-[3] The intensity of the reflected or transmitted light fluctuates strongly from position to position and from observation direction to another. Similarly, a strongly fluctuating intensity is also observed when one changes the wavelength of the light. An example is given in Fig. 1.[4] Notice the typical structure of a speckle pattern, with many peaks of low intensity and only occasional peaks of high intensity. In fact, the intensity probability distribution is an exponential function known as Rayleigh statistics.[5]

Since the speckle pattern changes with wavelength, it must be an interference phenomenon. Hence, multiply scattered waves still interfere.

In practice, the structure of a speckle pattern cannot be calculated. This calculation would require not only knowledge of the scattering properties of all individual scatterers as surrounded by other scatterers, but also the evaluation of all possible trajectories of the light through the medium. A speckle pattern is unique in the sense that a change of the position of one scatterer will alter the speckle pattern.[6] A change of the speckle pattern can also be caused by very small displacements of many scatterers, as happens with suspended particles subject to Brownian motion. By correlating speckle patterns recorded at different times, one can study the motion of the particles on a sub-nanometer length scale. This measuring technique is known as diffusive wave spectroscopy.[7]

1.2.2 Coherent backscattering

Since a speckle pattern depends strongly on the positions of the scatterers, one should study *average* properties of multiply scattered light or of the random medium itself rather then attempt to build a theory to describe a speckle pattern. Average quantities are obtained from measurements of many different arrangements of the scatterers, where the macroscopic parameters like the density of the scatterers are kept constant. Every arrangement of the scatterers yields a different speckle pattern, the sum of these *independent* patterns will yield a smooth intensity profile. In other words: the interference contribution will be averaged out by this procedure.

There is, however, a particular interference contribution still present after the averaging procedure. Moreover, this interference contribution emerges only after an average has been performed. Consider a scattering path depicted as in Fig. 2.[1] A wave propagating along such a path will develop a certain phase shift. It is easy to see that a wave following this path in opposite direction, a so called 'time reversed wave', develops the same phase shift. Hence, the phase difference between the time forward and the time reversed wave is zero and *independent* on the position of the scatterers involved. The interference between time forward and reversed waves is thus constructive and survives the averaging. In an experiment, were the integration time on a detector is large compared to the rate of change of the scattering configurations, one will observe an increased intensity in the exact backscatter direction. At a small angle θ with the exact backscatter direction, the phase difference $\Delta\phi$ between time reversed waves will depend on the location of

[1]By a scattering path we mean an arrangement of scatterers along which the wave propagates.

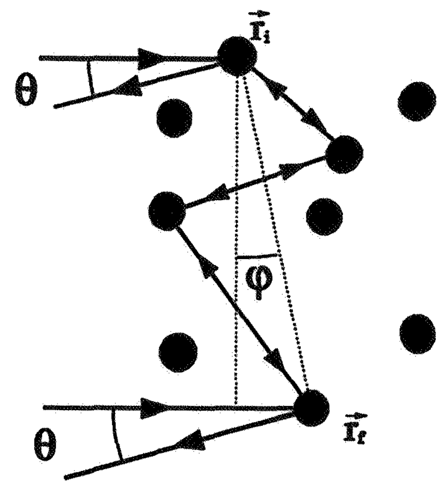

Figure 2: A scattering path contributing to the reflected intensity can be traversed in two directions as indicated by the arrows. The observation direction makes an angle θ with the exact backscatter direction.

the first ($\mathbf{r}_i$) and the last scatterer ($\mathbf{r}_f$)

$$\Delta\phi = \frac{2\pi}{\lambda}|\mathbf{r}_i - \mathbf{r}_f|(\sin(\varphi) - \sin(\varphi - \theta)), \tag{1.1}$$

λ being the wavelength of the light. Hence, the interference contribution to the backscattered light will decay as the angle with the exact backscatter direction increases.

An enhanced intensity in the backscatter direction as a consequence of interference, coherent backscattering, should not be confused with enhanced backscattering due to retro-reflection, which is not an interference phenomenon. Retro-reflection may emerge from several 'mirrors' placed at right angles to each other, or when light focused by a lens is (multiply) scattered at the focus point. The first mechanism of retro-reflection is used in for instance bike reflectors and road markers. The bright eyes of cats in the dark and the red pupils of people on flashed photographs are a manifestation of the latter mechanism of retro-reflection. The first reported, but misinterpreted, observation of retro-reflection is by Benvenuto Cellini in the 16^{th} century.[8] There will also be an interference contribution to the retro-reflected light, but the angular width will be extremely small and a negligible contribution to the total reflected intensity.

Coherent backscattering as a result of interference was already known in the early 80^s[9] but this was not recognized to be closely connected with a phenomenon that was experimentally observed for electron transport in metals with impurities.[10]-[12]

1.2.3 Anderson localization

Inside any multiply scattering medium, the intensity at a point Q due to a source located at P, is given by the square of the sum over the suitably normalized amplitudes of the waves following all possible scattering paths connecting P to Q,[13] as indicated in Fig. 3,

$$I = \left|\sum_i A_i(P \rightarrow Q)\right|^2 . \tag{1.2}$$

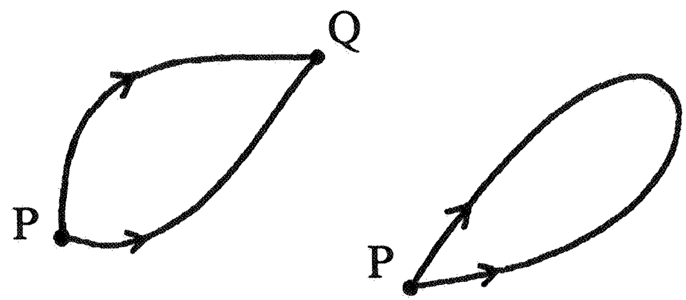

Figure 3: The intensity at point Q due to a source at P is given by the sum of intensities of all possible paths leading from P to Q. If Q is on top of P (right plot) an interference contribution enters.

Since each path gives a different phase shift to the wave, on average the cross terms in the square will cancel and the intensity at Q is given by the sum of the squared amplitudes (meaning the interference contribution is absent)

$$I = \sum_i |A_i(P \rightarrow Q)|^2 . \tag{1.3}$$

But if Q coincides with P, the scattering path can be traversed in opposite direction. A wave traversing the path in one direction will interfere constructively with a wave traversing the path in the other direction, which doubles the total intensity at P. Hence, the probability to return to the initial position is twice as large as one would expect without interference taken into account.

Normally, this returning probability is small. On increasing the disorder (reducing the mean-free path), the probability to return may become substantial and diffusive propagation is strongly frustrated. This phenomena is known as Anderson localisation, and occurs for systems fulfilling the Ioffe-Regel criterium[14]

$$kl \leq 1, \tag{1.4}$$

with l being the mean-free path, and $k = 2\pi/\lambda$ the wavevector.

In the Anderson regime, all waves are localized in an infinite medium; the extent in space decays exponentially for large distances. Localized modes do not contribute to the conductance (for the case of electrons) or the transport of waves, and the diffusion constant will be zero. For a finite medium, the intensity can 'leak out', which means in practice a scale dependent diffusion constant, or a total transmission inversely proportional with the thickness squared. The model of Anderson is used to explain the experimentally observed conductor-insulator-transition of disordered metals.

To stress the fact that Anderson localization is a consequence of the same physical mechanism as coherent backscattering (constructive interference of time reversed waves), one has introduced the term 'weak localization' to address the coherently backscattered light. Anderson localization of light is then referred to as strong localization.

A conductor is said to be in the mesoscopic regime when the following inequality holds

$$L \ll L_\phi, \tag{1.5}$$

with L being the typical dimensions of the conductor. The length L_ϕ refers to the phase incoherence length of the electrons. For light this means that scattering media are always in the mesoscopic regime. If in addition $l \ll L$, diffusion is the dominant transport mechanism, but interference contributions are emphatically present.

1.3 Applications

The start of the research of multiple scattering of light may be attributed to astronomers, who studied e.g. the scattering properties of planetary atmospheres and the transmission of light emitted by distant stars through interstellar clouds. They wrote the first books on multiple scattering of light, and most of the terminology and symbolic abbreviations used in the description of multiple light scattering originate from astronomers or refer to astronomical phenomena.[15]

Nowadays, the field of applications has embraced ocean optics, geology, medicine and remote sensing of vegetation. In remote sensing of vegetation one tries to deduce from reflection measurements the biomass of for instance a rain forest subdivided in e.g. trunks, branches and leaves.[16] Even near field corrections are performed to describe the scattering properties of a tree surrounded by others (wavelengths from centimeters to tens of meters are used). Applications in geology and medicine are more focused on the development of imaging tools: imaging of tumours in vivo (skin, breast etc.).[17] Screening a human population with x-rays induces probably more tumours than there will be detected.[18] Hence, a far less harmful method should be found, and the use of the visible light is a possibility. However, visible light will be multiply scattered by for instance the blood cells.

1.4 This thesis

In chapter 2 we will give an introduction to the multiple scattering theory. Important aspects of the experimental apparatus are discussed in chapter 3. In Chapter 4 we will study interference phenomena analogous to coherent backscattering but now for the transmitted light. We will make a small excursion to the combination of multiply scattering media and rough surface scattering. In Chapter 5 we will show how the effective index of refraction of a multiply scattering medium can be determined by a study of the coherently backscattered light as a function of the mismatch in index of refraction between scattering and non-scattering media. In Chapter 6 we will study the impact of anisotropic scattering on the lower order of scattering processes. Finally, in Chapter 7 imaging applications using the multiply scattered light are investigated.

References

[1] G. Parry, *Some effects of surface roughness on the appearance of speckle in polychromatic light*, Opt. Comm. **12**, 75 (1974).

[2] N. Garcia and A.Z. Genack, *Crossover to strong intensity correlation for microwave radiation in random media*, Phys. Rev. Lett. **63**, 1678 (1989).

[3] M. Tomita and M. Matsuoka, *Temporal fluctuations in disordered static media*, Phys. Rev. B **43**, 13579 (1991).

[4] *data were kindly supplied by J.F. de Boer.*

[5] J.C. Dainty, 'Progress in optics', Vol. 14, Ed. E. Wolf (North Holland, Amsterdam, 1976).

[6] R. Berkovitch, *Sensitivity of the multiple-scattering speckle pattern to the motion of a single scatterer*, Phys. Rev. B **43**, 8638 (1991).

[7] J.X. Zhu, D.A. Weitz, and R. Klein, *Dynamic correlations of multiple scattered light from strongly interacting suspensions*, p. 115, R. Berkovits, *Disordered fabry-perot interferometer: diffusive wave spectroscopy*, p. 201, in 'Photonic band gaps and localization', Ed. C.M. Soukoulis, (Plenum press, New York, 1993).

[8] B. Cellini, autobiography, *see* M. Minnaert, 'Natuurkunde van het vrije veld', Vol. **I**, (Thieme, Zutphen, 1974).

[9] Y. Kuga and A. Ishimaru, *Retroreflection from a dense distribution of spherical particles*, J. Opt. Soc. Am. A **1**, (1984) 831. L. Tsang and A. Ishimaru, *Backscattering enhancement of random discrete scatterers*, J. Opt. Soc. Am. A **1**, 836 (1984).

[10] M.P. van Albada and A. Lagendijk, *Observation of weak localization of light in a random medium*, Phys. Rev. Lett. **55**, 2692 (1985).

[11] P.E. Wolf and G. Maret, *Weak localization and coherent backscattering of photons in disordered media*, Phys. Rev. Lett. **55**, 2696 (1985).

[12] P.W. Anderson, *Absence of diffusion in certain random lattices*, Phys. Rev. **109**, 1492 (1958).

[13] D.E. Khmel'nitskii, *Localization and coherent scattering of electrons*, Physica **126** B, 235 (1984).

[14] N.F. Mott, *Electrons in disordered structures*, Adv. Phys. **16**, 49 (1967);

[15] S. Chandrasekhar, 'Radiative transfer', (Dover, New York, 1960). H.C. van de Hulst, 'Multiple light scattering', Vols. I and II, (Acad. New York, 1980), 'Light scattering by small particles', (Dover, New York, 1957; 1981).

[16] Proceedings on Progress In Electromagnetics Research Symposium (PIERS 1994), Eds. B. Arbesser-Rastburg, M. Borgeuad, S. Buinomon, J. Belshaw, J. Matagne, J. Noll, (Kluwer acad. pub. 1994) (on cd-rom).

[17] Proceedings of the Optical Society of America topical conference on *Advances in optical imaging and photon migration*, OSA Proceedings Vol. 21, Ed. R.R. Alfano, (1994).

[18] G. 't Hooft, private communication.

Chapter 2

Introduction to multiple scattering theory

In this chapter we will review theory on single and multiple scattering of light, and introduce important features and concepts used in this thesis. More details and extensive studies on single and multiple scattering of waves can be found in excellent books of which the references are given at the end of this chapter. We will study the weak localization regime, i.e. the regime where diffuse transport is dominant. We will treat finite size and point scatterers. We will discuss the mean amplitude Green's function for an infinite system of identical scatterers at low density, and the Bethe-Salpeter equation that describes the diffuse intensity in the scattering medium. Two classes of scattering events turn out to be important for our experiments. The first class leads to diffuse propagation inside the bulk of the scattering medium, which is the dominant transport mechanism. The second class describes the coherently backscattered light. The diffusion equation is derived by using the Ladder approximation of the Bethe-Salpeter equation. Coherent backscattering and anisotropic scattering is discussed in the last sections of this chapter.

The mismatch in the index of refraction between the scattering and the non-scattering medium will be neglected in this chapter, an extensive study of the influence of this mismatch being deferred until Chapter 5.

2.1 Single scattering of light

2.1.1 Cross sections

How much light is removed from an incident beam by an object? The answer is given by the magnitude of its effective cross section or shortly: cross section. The cross section is measured in length squared. The amount of light removed from the beam by an object is then given by the amount of light of the incident beam falling on an area equal to the effective cross section of that object. The effective cross section varies from zero to a large number of times the geometrical cross section of an object.

Since we are interested eventually in multiple scattering of light, we not only want to know the magnitude of the flux being removed from the incident beam, but also the (average) scattering direction, and how much light is absorbed. Hence, we will need four distinct cross sections: the extinction cross section, the scattering cross section, the absorption cross section and the pressure cross section. The extinction cross section σ_{ex} gives the amount of light removed from the incident beam. This removed light can be replaced by light in other directions and/or it can be partly absorbed. The total amount of light replaced by light with the same frequency in any other direction, the scattered light, is given by the scattering cross section σ_{sc}. The absorption cross section σ_{ab} gives the total amount of light removed from the incident beam and not replaced by scattered light with the same frequency. The last cross section, the pressure cross section σ_{pr} gives the amount of momentum removed from the incident beam and not replaced by momentum carried by the scattered light. From σ_{pr} one can infer the average direction of the scattered light with respect to the incident light, which is a useful concept when studying multiple scattering in disordered systems. The radiation pressure exerted on a scatterer is proportional to the pressure cross section. If the scattering is strictly forward, the pressure cross section is zero, and consequently the radiation pressure on this scatterer vanishes. Any cross section of a particle will in general depend on its dielectric constant, shape and size with respect to the wavelength, and its orientation with respect to the incident wave.

The scattered fraction of the removed light from the incident beam defines the albedo a of a scatterer

$$a \equiv \frac{\sigma_{sc}}{\sigma_{sc} + \sigma_{ab}} = \frac{\sigma_{sc}}{\sigma_{ex}}. \tag{2.1}$$

For non-absorbent particles the albedo a is 1.

Consider a monochromatic plane wave, with frequency ω and energy flux A^2 propagating along the z-axis, impinging from minus infinity on a particle with extinction cross section σ_{ex} and scattering cross section σ_{sc}, see Fig. 1. The scattered

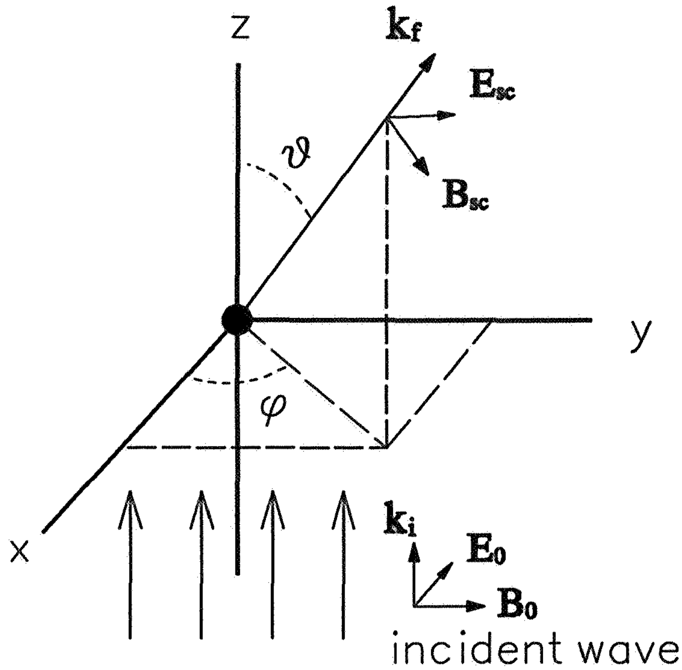

Figure 1: Incident light along the z-axis with wavevector $\mathbf{k}_i$ is scattered in direction $\mathbf{k}_f$ by a particle located at the origin, $\mathbf{E}$ and $\mathbf{B}$ denote the electric and magnetic field, respectively, of the incident and scattered light.

wave in the far field at position r is a spherical outgoing wave. It can be expressed, without taking account of the polarization yet, as

$$E_{sc} = AS(\vartheta,\phi)\frac{\exp(-ik_0r + i\omega t)}{ik_0r} = S(\vartheta,\phi)\frac{\exp(-ik_0r + ik_0z)}{ik_0r}E_0. \tag{2.2}$$

We have defined the complex amplitude scattering function $S(\vartheta,\phi)$ and $E_0 = A\exp(-ik_0z + i\omega t)$ as the incoming wave, with k_0 the magnitude of wavevector of the medium without scatterers. The angle ϑ is defined with respect to the direction of the incoming wave, and ϕ is the azimuth angle. The intensity $I(\vartheta,\phi)$ of the scattered light is given by

$$I(\vartheta,\phi) = A^2\frac{|S(\vartheta,\phi)|^2}{k_0^2r^2}, \tag{2.3}$$

and the scattering cross section by

$$\sigma_{sc} = \frac{1}{k_0^2}\int d\Omega|S(\vartheta,\phi)|^2. \tag{2.4}$$

A suitable normalization of the angular resolved scattering properties of a particle defines the phase function $F(\vartheta,\phi) = \frac{|S(\vartheta,\phi)|^2}{k_0^2\sigma_{sc}}$.[1] The phase function will not depend on ϕ if the particle is spherically symmetric. The amount of forward momentum carried by the scattered light is given by $\sigma_{sc}\cos\vartheta F(\vartheta,\phi)$. Thus the total momentum removed from the incident beam and not replaced by the scattered light can be calculated to be

$$\sigma_{pr} = \sigma_{ex} - \int d\Omega\sigma_{sc}\cos\vartheta F(\vartheta,\phi) = \sigma_{ex} - <\cos\vartheta> \sigma_{sc} = (1- <\cos\vartheta>)\sigma_{sc}. \quad (2.5)$$

The last equality holds for non-absorbent particles.

There is an important relation between the forward scattered light and the extinction cross section. The intensity of the incident plus forward scattered light *far away* from a particle located at the origin is

$$\begin{aligned} |E_0+E|^2 &= \left|E_0\left(1+\frac{1}{ik_0z}S(0)\exp(-ik_0(x^2+y^2)/2z)\right)\right|^2 \\ &= 1-\frac{2}{k_0z}Re\left(iS(0)\exp(-ik_0(x^2+y^2)/2z)\right), \quad \text{(for } A\text{=1)}. \quad (2.6) \end{aligned}$$

Hence, the total intensity integrated over an area O perpendicular to the z-axis is

$$O - Q.$$

The reduction of the intensity falling on O is thus equal to the intensity falling on an area Q. This is by definition the extinction cross section of the particle. Therefore

$$\sigma_{ex} = \lim_{O\to\infty}\int_O dxdy\frac{2}{k_0z}Re\left(iS(0)\exp(-ik_0(x^2+y^2)/2z)\right) = \frac{4\pi}{k_0^2}Re(S(0)). \quad (2.7)$$

This fundamental equation is called the extinction theorem.

If we take into account polarization, Eq. (2.2) turns into a matrix equation

$$\begin{pmatrix} E_{sc,\perp} \\ E_{sc,\|} \end{pmatrix} = \begin{pmatrix} S1(\vartheta,\phi) & S4(\vartheta,\phi) \\ S3(\vartheta,\phi) & S2(\vartheta,\phi) \end{pmatrix} \begin{pmatrix} E_{0,\perp} \\ E_{0,\|} \end{pmatrix} \frac{\exp(-ik_0r+ik_0z)}{ik_0r}, \quad (2.8)$$

where the suffix $\|$ ($\perp$) refers to the component of the electric field in (out of) the plane of scattering. For spherical particles $S3(\vartheta,\phi)$ and $S4(\vartheta,\phi)$ are zero and depolarization of the incident light does not occur in the plane of scattering. In the forward direction we must have $S1(0) = S2(0) = S(0)$ because of symmetry, and the extinction theorem is still given by Eq. (2.7).

[1]This phase function has nothing to do with the phase of the wave, nor with the phase shift obtained during scattering.

2.1.2 Rayleigh and Mie-solution

So far we have discussed general features of the scattering problem of a plane wave by a particle. We have not tried to calculate explicitly the cross section and phase functions of an arbitrary scatterer, we will come to this now. The scattering problem can be roughly divided into three regimes. The geometrical optics regime (the wavelength much *smaller* than the size of the particle), the reversed situation that is usually called the Rayleigh limit (the wavelength much *larger* than the particle) and the intermediate regime where the wavelength is comparable to the particle size. In the geometrical optics regime, the scattering behaviour can be understood using a ray tracing approach. However, features like the extinction paradox show that the wave character of light cannot be neglected even in the geometrical optics regime, see Ref. [1].

For large wavelengths, only the induced dipole (by the incident light) has a significant contribution to the scattered field, and it is given by

$$\begin{pmatrix} E_{sc,\perp} \\ E_{sc,\parallel} \end{pmatrix} = \begin{pmatrix} ik_0^3\alpha & 0 \\ 0 & ik_0^3\alpha\cos(\vartheta) \end{pmatrix} \begin{pmatrix} E_{0,\perp} \\ E_{0,\parallel} \end{pmatrix} \frac{\exp(-ik_0r + ik_0z)}{ik_0r}, \tag{2.9}$$

and the scattering cross section by

$$\sigma_{sc} = \frac{8}{3}\pi|\alpha|^2k_0^4, \tag{2.10}$$

with α being the polarizability of the particle and k_0 the wavevector of the incident light. Important to note is the k_0^4 dependency. This dependency is responsible for the colour of the sky and the setting sun. The cross section for blue light is much larger than that for red light. Hence, the blue light is scattered out of the direct sun light yielding a red setting sun. From other parts of the atmosphere the blue light is scattered into our eyes. The cosine in the matrix of Eq. (2.9) yields a high degree of polarization of the scattered light that is viewed at right angle with the direction of the incident sun light. If the size of the scatterer is comparable to the wavelength, the scattering behaviour does not follow a simple law as in Eq. (2.10). For the sky it means that it will be blue only if the scattering in the atmosphere is caused by single molecules. Scatterers of various larger sizes, aerosols (containing e.g. small water droplets!), spoil the whole effect, and the sky will be white.

Scattering resonances dominate the scattering behaviour of particles with a size comparable to the wavelength. For arbitrary shaped particles it is impossible to give exact solutions of the scattering problem, and numerical approximations should be used.[2]

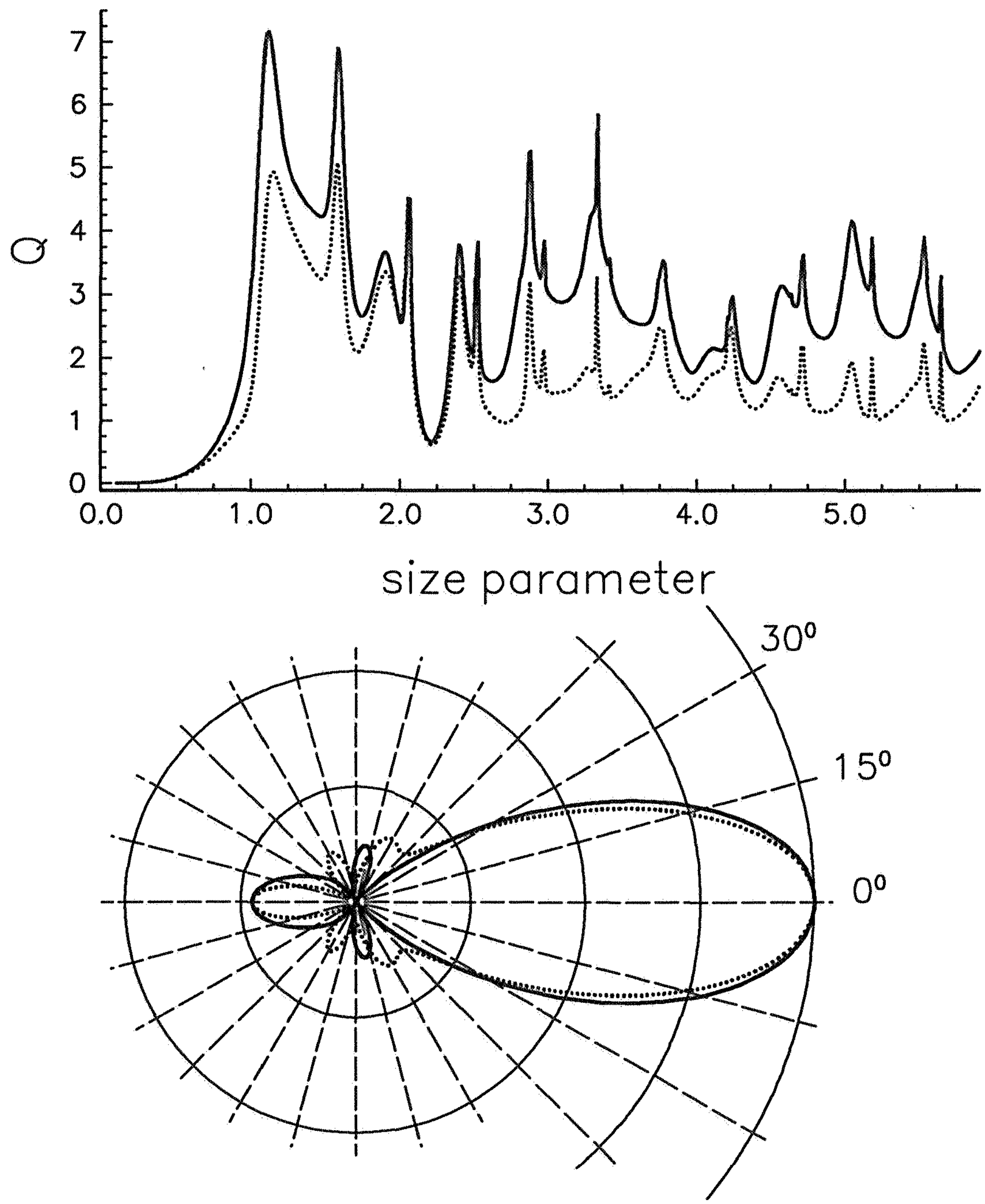

Figure 2: Upper plot: Scattering cross section (solid line) and pressure cross section (dotted line) of a spherical particle with $n = 2.7$ as a function of its size parameter X. Lower plot: Scattered intensity as a function of the angle for a spherical particle with index of refraction $n = 2$, and size parameter $X = 3.05$. Solid line: polarization out of the plane of scattering, dotted line: polarization in the plane of scattering.

Scattering of a monochromatic plane wave by a homogeneous spherical particle is exactly solvable.[1][3][4] It turns out that the scattering by a spherical particle is completely determined by the index of refraction of the sphere n and the size parameter. The size parameter X is defined as

$$X \equiv kr = \frac{2\pi n_m r}{\lambda_0}, \tag{2.11}$$

with λ_0 the vacuum wavelength, n_m the index of refraction of the medium *surrounding* the sphere with radius r.

The most important step in solving the scattering problem of a plane wave by a sphere is to expand a plane wave in spherical harmonics. Then boundary conditions at the surface of the sphere (enforced by Maxwell's equations) can be easily fulfilled. This solution is nowadays widely known and many computer programs have been written with which the scattering properties of spheres can be calculated. Usually, this solution is referred to as the Mie-solution. One has even started to talk about 'Mie scatterers'; denoting a spherical particle with a radius in the order of the wavelength. A 'Mie scatterer' is a rather sloppy term, it tends to indicate that the Mie-solution is only valid for scatterers with a radius comparable to the wavelength. The fact is that geometrical optics and Rayleigh scattering fail completely to describe scattering of light when the sphere is in the order of the wavelength. The Mie-solution is an exact solution for any radius and index of refraction of a spherical particle. However, numerical problems may arise when one tries to calculate scattering by very large spheres, say $X \gg 100$. Extensions of the Mie solution to layered spheres and ellipsoids is also possible.[4]

As an example we plot in Fig. 2 the scattering and pressure cross section as a function of the size parameter for a particle with n=2.7, and the angular resolved scattered intensity by a particle with n=2 and X=3.05 (polar diagram). The cross sections are expressed in efficiency factors according to

$$\sigma_{sc} = Q_{sc}\pi r^2, \tag{2.12}$$

with Q_{pr}, Q_{ex} and Q_{ab}, similarly. Clearly, one sees the complicated scattering behaviour in both plots. So for particles of the same size, rather striking scattering phenomena may occur: for instance an exceptional situation of uniform water droplets or (volcano) ash in the atmosphere can give rise to a blue setting sun or moon!

2.1.3 Free-space Green's function and t-matrices

In a strongly scattering environment it will be impracticable to use the full Mie-solution at each scattering event. The Mie-solution only applies to plane wave incidence, and a wave impinging after one scattering event on an other particle will in general not be a plane wave. A rigorous approach in which Maxwell's equations are numerically solved for a particular configuration of the scatterers cannot be used in our case, as an average over the positions of all the particles should be performed. We will use the simplifications of *scalar* waves and *isotropic* point scatterers in our description of the multiply scattered light. If one wishes, one could improve on this theory by using point scatterers with a Mie phase function.

Starting from Maxwell's equations, and neglecting the logarithmic derivative of the dielectric constant, each component of both the $\mathbf{E}$ and $\mathbf{B}$-fields can be shown to fulfil the same wave equation (see for a review ref. [5]). Inserting harmonic waves in the wave equation we arrive at the Helmholtz wave equation.

$$\Delta\Psi(\mathbf{r}) + \epsilon(\mathbf{r})k_0^2\Psi(\mathbf{r}) = 0, \tag{2.13}$$

where Ψ denotes one of the field components. The scattering is caused by the position-dependent dielectric constant $\epsilon(\mathbf{r})$: i.e. the scatterer. By separating the spatially dependent dielectric constant from the empty medium, $\epsilon(\mathbf{r}) \equiv 1 + \delta\epsilon(\mathbf{r})$, the scattering part is revealed

$$\Delta\Psi(\mathbf{r}) + k_0^2\Psi(\mathbf{r}) = V(\mathbf{r})\Psi(\mathbf{r}). \tag{2.14}$$

The scattering potential reads $V(\mathbf{r}) = -k_0^2\delta\epsilon(\mathbf{r})$, and $V(\mathbf{r}) = 0$ outside the scatterer. We shall solve the Helmholtz wave equation with the use of the free-space Green's function, it is the solution of Eq. (2.14) with a delta source at the right hand side

$$\Delta G(\mathbf{r},\mathbf{r}') + k_0^2 G(\mathbf{r},\mathbf{r}') = -\delta(\mathbf{r}-\mathbf{r}'). \tag{2.15}$$

The Green's function $G(\mathbf{r},\mathbf{r}')$ gives the response of the system at $\mathbf{r}'$ due to a source at $\mathbf{r}$. Fourier transforming this equation leads to a direct invertible form. We find the free-space Green's function in k-space:

$$G_0(\mathbf{k},\mathbf{k}') = \frac{\delta(\mathbf{k}-\mathbf{k}')}{k^2 - k_0^2}. \tag{2.16}$$

Fourier transforming back to real-space gives for 3-dimensions

$$G_0(\mathbf{r},\mathbf{r}') = \frac{1}{4\pi|\mathbf{r}-\mathbf{r}'|}\exp(-ik_0|\mathbf{r}-\mathbf{r}'|). \tag{2.17}$$

In one and two dimensions the k-space Green's function has the same form as for three dimensions. The real-space Green's function depends on the dimensionality. For two dimensions the Green's function is given by

$$G_0(\mathbf{r},\mathbf{r}') = \frac{1}{2\pi}K_0(ik_0|\mathbf{r}-\mathbf{r}'|), \tag{2.18}$$

and for one dimension it is

$$G_0(\mathbf{r},\mathbf{r}') = \frac{i}{2k_0}\exp(-ik_0|\mathbf{r}-\mathbf{r}'|). \tag{2.19}$$

We have solved Eq. (2.14) formally by writing

$$\Psi(\mathbf{r}) = \Psi_{in}(\mathbf{r}) - \int d\mathbf{r}' G_0(\mathbf{r},\mathbf{r}')V(\mathbf{r}')\Psi(\mathbf{r}'). \tag{2.20}$$

Where $\Psi_{in}(\mathbf{r})$ is a solution of the homogeneous equation (without a scatterer) and represents the incoming wave. Iterating Eq. (2.20) yields

$$\Psi(\mathbf{r}) = \Psi_{in}(\mathbf{r}) + \iint d\mathbf{r}''d\mathbf{r}' G_0(\mathbf{r},\mathbf{r}'')t(\mathbf{r}'',\mathbf{r}')\Psi_{in}(\mathbf{r}'), \tag{2.21}$$

which defines the t-matrix $t(\mathbf{r},\mathbf{r}')$ given by

$$\begin{aligned} t(\mathbf{r},\mathbf{r}') &= -V(\mathbf{r})\delta(\mathbf{r}-\mathbf{r}') + V(\mathbf{r})G_0(\mathbf{r},\mathbf{r}')V(\mathbf{r}') - \\ &\quad \int d\mathbf{r}'' V(\mathbf{r})G_0(\mathbf{r},\mathbf{r}'')V(\mathbf{r}'')G_0(\mathbf{r}'',\mathbf{r}')V(\mathbf{r}') + \cdots . \end{aligned} \tag{2.22}$$

One uses the term transition matrix since a t-matrix projects ingoing states of the incident light onto outgoing states; it describes the total effect of the scatterer on the wave.

For a point scatterer located at $\mathbf{r}_0$ with polarizability α, $V(\mathbf{r}) = -\alpha k_0^2\delta(\mathbf{r}-\mathbf{r}_0)$, the t-matrix can be rewritten as

$$\begin{aligned} t(\mathbf{r},\mathbf{r}') &= \delta(\mathbf{r}-\mathbf{r}_0)\delta(\mathbf{r}'-\mathbf{r}_0)\Big(\alpha k_0^2 + \alpha k_0^2 G_0(\mathbf{r}_0,\mathbf{r}_0)\alpha k_0^2 + \\ &\qquad \alpha k_0^2 G_0(\mathbf{r}_0,\mathbf{r}_0)\alpha k_0^2 G_0(\mathbf{r}_0,\mathbf{r}_0)\alpha k_0^2 + \cdots\Big) \qquad (2.23) \\ &= \frac{\alpha k_0^2}{1-\alpha k_0^2 G_0(\mathbf{r}_0,\mathbf{r}_0)}\delta(\mathbf{r}-\mathbf{r}_0)\delta(\mathbf{r}'-\mathbf{r}_0). \qquad (2.24) \end{aligned}$$

The first-order Born approximation retains only the first term or equivalently, replaces the scattered field by the incoming wave in Eq. (2.20).

It is fruitful to introduce a diagrammatic representation of Eq. (2.23)[6]

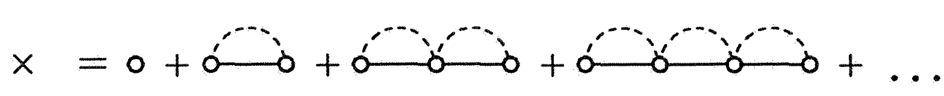

(2.25)

Where $\times$ denotes the t-matrix, $\circ$ the scattering potential $\alpha k_0^2\delta(\mathbf{r}-\mathbf{r}_0)$, solid lines the free-space Green's function and dashed lines indicate the same scatterer.

By writing the expansion of the t-matrix as in Eq. (2.24), the scattering problem is still only solved formally. In one dimension Eq. (2.24) can be summed to give the exact solution, but in two and three dimensions the return Green's function $G_0(\mathbf{r},\mathbf{r})$ diverges, so Eq. (2.24) does not make sense in two and three dimensions.

One way to 'solve' this problem is to omit the third and higher order terms and the diverging real part of the second term. In this way one arrives at the second order Born-approximation, which is often used for electronic systems. A disadvantage of this approximation is that it violates the optical theorem and that scattering resonances are not contained by this t-matrix. In real life, however, scattering resonances are more common than exceptional. Incorporation of resonant scattering behaviour can be done by introducing a cut-off length in the return Green's function. On physical grounds it is logical to choose the cut-off length proportional to the size of the physical scatter. One finds the t-matrix[7]

$$t(\mathbf{r},\mathbf{r}') = \frac{U_{eff}}{1+U_{eff}\frac{ik_0}{4\pi}}\delta(\mathbf{r}-\mathbf{r}_0)\delta(\mathbf{r}'-\mathbf{r}_0) \equiv t\delta(\mathbf{r}-\mathbf{r}_0)\delta(\mathbf{r}'-\mathbf{r}_0). \tag{2.26}$$

with $U_{eff} = \alpha k_0^2/(1-\alpha k_0^2\Lambda)$. It has a scattering resonance at $k_0^2 = 1/\Lambda\alpha$. Comparison with the Mie solution for scalar waves yields $1/\Lambda = (\pi^2 r/12)^2$, with r the radius of the sphere.[7]

Relations between the t-matrix and the cross sections can be found by considering a plane wave with initial wavevector $\mathbf{k}_0$ from $z=-\infty$ falling on a scatterer located at the origin. Equation (2.21) then contains the Fourier transform of $t(\mathbf{r},\mathbf{r}')$ for $z \gg x, y$. Hence, we can write

$$\Psi(\mathbf{r}) = \exp(-ik_0\mathbf{n}\cdot\mathbf{r}) + t(\mathbf{n}'k_0,\mathbf{n}k_0)\frac{\exp(-ik_0 r)}{4\pi r}, \qquad \mathbf{n} \equiv \frac{\mathbf{k}_0}{k_0} \tag{2.27}$$

Calculating the intensity removed by the point scatterer as in section 2.1.1, leads to the result

$$\sigma_{ex}(\mathbf{n}) = -\frac{1}{k_0}Im(t(\mathbf{n}k_0,\mathbf{n}k_0)). \tag{2.28}$$

The scattering cross section can be found by integrating the scattered intensity over a large sphere centred around the origin

$$\sigma_{sc}(\mathbf{n}) = \int r^2 d\Omega' \left| t(\mathbf{n}k_0,\mathbf{n}'k_0)\frac{\exp(-ik_0 r)}{4\pi r}\right|^2 \tag{2.29}$$

For isotropic scattering we find

$$\sigma_{ex} = -\frac{1}{k_0}Im(t), \text{ and } \sigma_{sc} = \frac{1}{4\pi}|t|^2. \tag{2.30}$$

Using the definition of the albedo,

$$a = \frac{\sigma_{sc}}{\sigma_{ex}} = -\frac{1}{4\pi}|t|^2\frac{k_0}{Im(t)} \tag{2.31}$$

we find for non-absorbent particles the optical theorem

$$Im(t) = \frac{-k_0}{4\pi}|t|^2. \tag{2.32}$$

2.2 Multiple scattering

Scattering light from a disordered medium will yield different results for different configurations of the scatterers. Hence, if we want to obtain useful information on a scattering medium, we should be concerned with properties averaged over the many possible configurations of the scatterers. Average quantities like the diffusion constant, transmission and reflection coefficients, can be measured and reproduced in an experiment. Thus in our theoretical description, we should at some stage square the amplitude to obtain the intensity and average the intensity over the scattering configurations. The average of the square of the amplitude contains the diffuse intensity and 'coherent beam' (the reduced incident intensity), whereas the square of the average describes only the properties of the coherent beam. The reduced intensity is called the 'coherent beam' because it contains unscrambled phase information of the incident light. This does not mean that the multiply scattered light is incoherent. The occurrence of speckle is a strong counter example.

We will first show how one calculates in a phenomenological manner the attenuation of the incident wave in a scattering medium. Consider a semi-infinite medium ($z>0$ medium, $z<0$ vacuum) with a density n of randomly placed identical scatterers with an extinction cross section $\sigma_{ex} = \sigma_{sc} + \sigma_{ab}$. A light beam propagating in this medium will be attenuated, because light is absorbed or scattered out of the beam. Suppose an incoming plane wave from $z=-\infty$ with an intensity I_0 impinges on the medium. If we know the intensity of this wave at depth z, the intensity at $z+dz$ is given by

$$I(z + dz) = I(z) - I(z)n\sigma_{ex}dz. \tag{2.33}$$

Solving this equation, and using the boundary condition that at $z = 0$ the intensity should be I_0, we find Lambert-Beer's Law

$$I(z) = I_0 \exp(-n\sigma_{ex}z) \equiv I_0 \exp(-z/l_{ex}). \tag{2.34}$$

By the last equality we have defined the extinction mean-free path l_{ex}. The coherent beam is actually the interference between the forward scattered and the residual unscattered light. The coherent beam is therefore subject to the average index of refraction of the medium. Equation (2.34) gives the answer to the question how far one can see through the fog, i.e one extinction mean-free path. An experimental example is given in Fig. 3. We have measured the directly transmitted light of a collimated beam as a function of the thickness of a multiply scattering medium, and thus determined the extinction mean-free path of, in this case, milk. As the coherent beam attenuates, a diffuse intensity is built up. Before we can

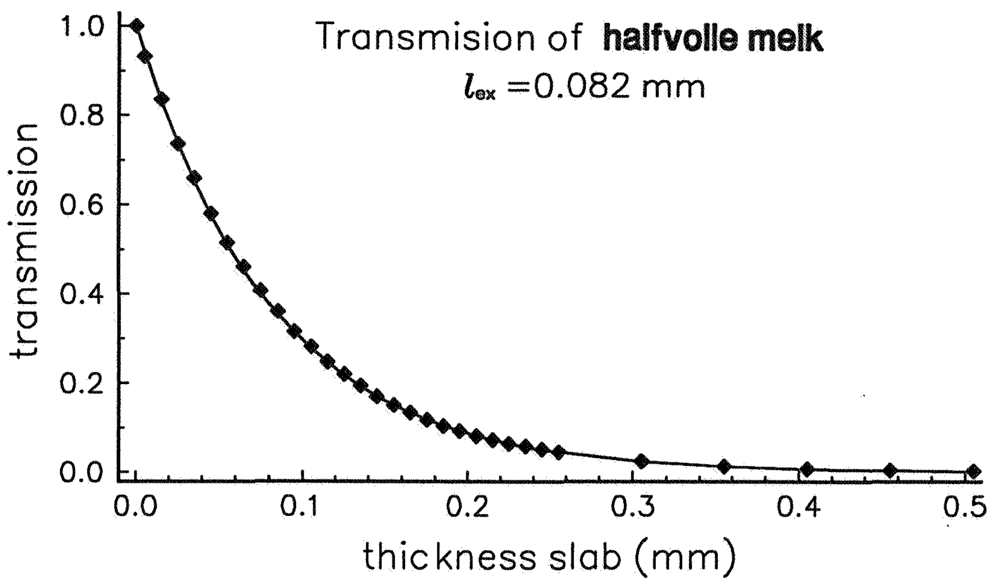

Figure 3: Measured transmission of the unscattered light through 'halfvolle melk' (half fat milk) as a function of the slab thickness. The solid line is an exponential function yielding the extinction mean-free path of milk $l_{ex} = 82\mu m$, used wavelength: 633 nm.

calculate this crossover, we need to have a better understanding of the amplitude in a disordered medium.

2.2.1 Amplitude properties

Consider an infinite system of randomly placed isotropic point scatterers. We will calculate the average amplitude propagator or Green's functions for the disordered system. An amplitude propagator is equal to the sum of amplitudes of all possible scattering paths arriving from $\mathbf{r}$ at $\mathbf{r}'$. The amplitudes should be summed coherently, i.e. taking into account the phase of each amplitude

$$\begin{aligned} g(\mathbf{r},\mathbf{r}') &= G_0(\mathbf{r},\mathbf{r}') - \int d\mathbf{r}'' G_0(\mathbf{r},\mathbf{r}'')V(\mathbf{r}'')G_0(\mathbf{r}'',\mathbf{r}') + \\ & \int d\mathbf{r}''' \int d\mathbf{r}'' G_0(\mathbf{r},\mathbf{r}''')V(\mathbf{r}''')G_0(\mathbf{r}''',\mathbf{r}'')V(\mathbf{r}'')G_0(\mathbf{r}'',\mathbf{r}') - \cdots \quad (2.35) \\ &= G_0(\mathbf{r},\mathbf{r}') - \int d\mathbf{r}'' G_0(\mathbf{r},\mathbf{r}'')V(\mathbf{r}'')g(\mathbf{r}'',\mathbf{r}'), \quad (2.36) \end{aligned}$$

$V(\mathbf{r})$ is the aforementioned scattering potential but now for the whole collection of scatterers. For point scatterers the scattering potential is given by

$$V(\mathbf{r}) = \sum_i^N -\alpha k_0^2 \delta(\mathbf{r} - \mathbf{R}_i), \quad (2.37)$$

with $\mathbf{R}_i$ the position of the i^{th} scatterer, and N the total number of scatterers. Equation (2.35) can be depicted by

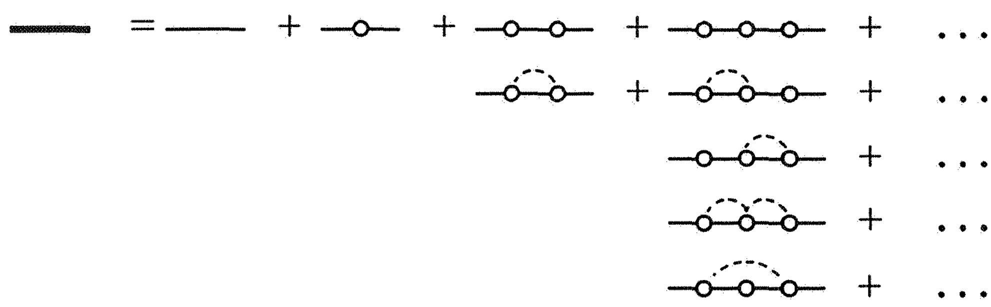

(2.38)

A thick line indicates the dressed Green's function (not yet averaged over the position of the scatterers), and a thin line the free-space Green's function, o is the scattering potential, $\alpha k_0^2 \delta(\mathbf{r}-\mathbf{R}_i)$, of one scatterer. The average Green's functions are defined by

$$G(\mathbf{r}-\mathbf{r}') \equiv < g(\mathbf{r},\mathbf{r}') > \tag{2.39}$$

and

$$G(k)\delta(\mathbf{k}-\mathbf{k}') \equiv < g(\mathbf{k},\mathbf{k}') > . \tag{2.40}$$

If we define Σ as the sum of all irreducible diagrams (diagrams that cannot be broken into smaller parts without cutting a dashed line) we can rewrite Eq. (2.38)

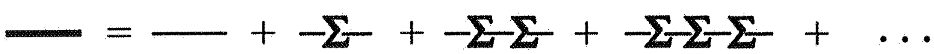

(2.41)

Contributions to Σ containing only one scatterer can be summed to give the t-matrix of the scatterer (the density of the scatterers shows up as prefactor as a consequence of the averaging),

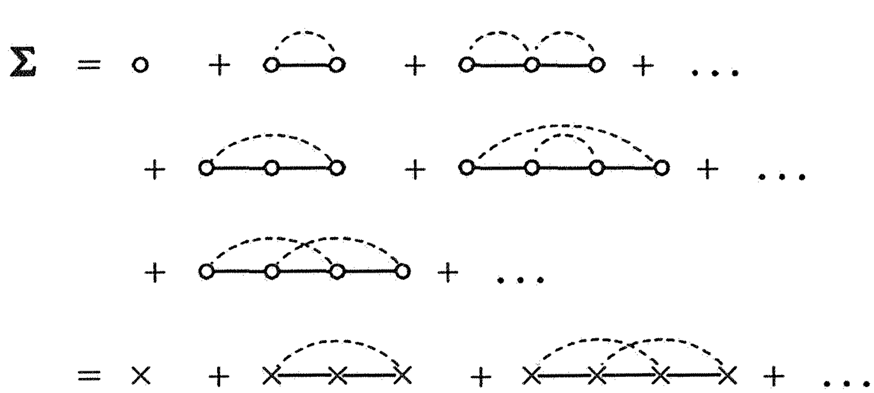

(2.42)

It can easily be checked that all diagrams of Eq. (2.38) are generated by inserting Eq. (2.42) in Eq. (2.41). The sum of all irreducible diagrams is called the self energy or mass operator of the system. The terms 'self energy' and 'mass operator' originate from field theory. Equation (2.41) can be rewritten in a generating equation, which is called the Dyson equation. The Dyson equation reads in k-space

$$G(k) = G_0(k) + G_0(k)\Sigma(k)G(k). \tag{2.43}$$

The Dyson equation can be solved to give the amplitude propagator for the disordered medium

$$G(k) = \frac{1}{G_0^{-1} - \Sigma(k)} = \frac{1}{k^2 - k_0^2 - \Sigma(k)}. \tag{2.44}$$

Usually, only the first term of the self energy is taken into account, which is called the independent scattering approximation

$$\Sigma(k) = nt. \tag{2.45}$$

Now we can transform Eq. (2.44) to real-space coordinates and find

$$G(\mathbf{r}) = \frac{\exp(-iKr)}{4\pi r}, \tag{2.46}$$

with the effective k-vector K given by

$$K = \sqrt{k_0^2 + nt}. \tag{2.47}$$

In this approximation we can write down the real and imaginary part of the effective k-vector explicitly

$$K = \sqrt{k_0^2 + nt} \approx k_0\sqrt{1 + n\frac{Re(t)}{k_0^2}} + i\frac{1}{2}n\frac{1}{k_0}Im(t) = mk_0 - \frac{i}{2l_{ex}}, \tag{2.48}$$

where we have used Eq. (2.28). The real part of the effective k-vector is shifted from the vacuum value as a result of the presence of scatterers with an index of refraction different from that of the embedding medium. The shift expresses a mean-index of refraction m of the scattering medium. The imaginary part of the effective k-vector expresses extinction of the coherent beam due to scattering. The intensity of the coherent beam is given by

$$I_{coh}(\mathbf{r}) = |A\Psi_{coh}(\mathbf{r})|^2 = I_0|\exp(-iKz)|^2 = I_0\exp(-z/l_{ex}), \tag{2.49}$$

in accordance with Eq. (2.34).

2.2.2 Intensity properties

We can write down the intensity Green's function (not yet averaged over the scattering configurations) inside the disordered medium as

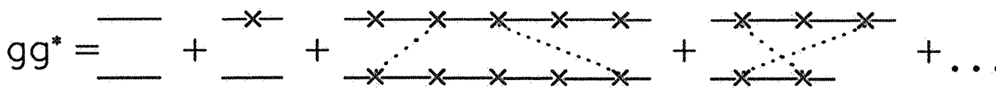

(2.50)

By convention the upper line denotes the amplitude and the lower line the complex conjugate amplitude. Dashed lines indicate again the same scatterers. Since we average over the disorder, the number of scatterers runs from zero to infinity in between two scatterers that are connected with dashed lines from upper to lower line, for instance in the third diagram of Eq. (2.50). We can account for this at once by the use of the dressed Green's function in between those two scatterers. We arrive at the Bethe-Salpeter equation

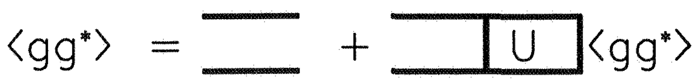

(2.51)

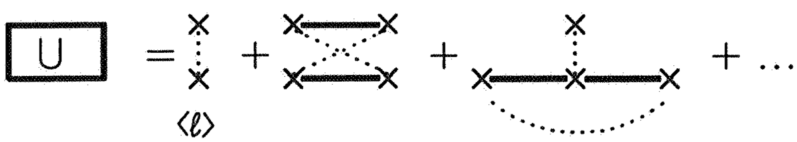

(2.52)

where U is the irreducible vertex. It is the intensity equivalent of the self energy. Iterating the Bethe-Salpeter equation yields,

$$<gg^*>= GG^* + GG^*RGG^*, \tag{2.53}$$

which defines the reducible vertex R as

$$R = U + UGG^*R. \tag{2.54}$$

In the weak-scattering regime all recurrent scattering events can be neglected, and we only take into account the first contributions to the irreducible vertex U,

$$U =<l>, \tag{2.55}$$

where $<l>$ is defined as the first diagram of Eq. (2.52). This leads to diffuse transport of light through the medium. However, in order to describe coherent backscattering of light, which is a major subject of this thesis, we also need the so called most crossed diagrams (the diagrams describing the interference between time reversed waves). Thus we use for the reducible vertex

$$R =<L> + <C>, \tag{2.56}$$

with $<L>$ the sum of all ladder diagrams and $<C>$ the sum of the most crossed diagrams

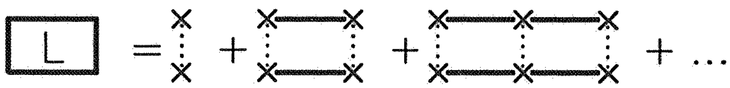
(2.57)

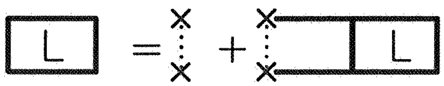
(2.58)

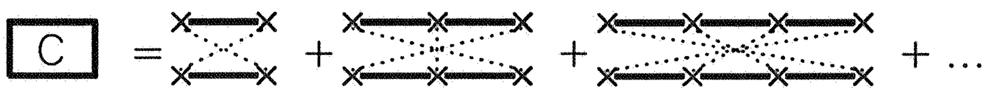
(2.59)

Equation (2.58) reads in real coordinates

$$\begin{aligned} <L(\mathbf{r}_1,\mathbf{r}_2,\mathbf{r}_3,\mathbf{r}_4)> &= n|t|^2\delta(\mathbf{r}_1-\mathbf{r}_2)\delta(\mathbf{r}_1-\mathbf{r}_3)\delta(\mathbf{r}_1-\mathbf{r}_4)+ \\ & n|t|^2\int d\mathbf{r}_5 d\mathbf{r}_6 G(\mathbf{r}_1,\mathbf{r}_5)G^*(\mathbf{r}_2,\mathbf{r}_6) <L(\mathbf{r}_5,\mathbf{r}_6,\mathbf{r}_3,\mathbf{r}_4)> . \end{aligned} \tag{2.60}$$

Noting that the most crossed diagrams are quite similar to the ladder diagrams, except that the complex conjugate amplitude traverses the scattering sequence in reversed order, we expect $<L>$ and $<C>$ to fulfil a similar equation if we separate out the single scattering contribution to $<L>$. Hence, we write for $<L>$[8]

$$\begin{aligned} &<L(\mathbf{r}_1,\mathbf{r}_2,\mathbf{r}_3,\mathbf{r}_4)>= \\ &\quad n|t|^2\delta(\mathbf{r}_1-\mathbf{r}_2)\delta(\mathbf{r}_1-\mathbf{r}_3)\delta(\mathbf{r}_1-\mathbf{r}_4)+F(\mathbf{r}_1,\mathbf{r}_3)\delta(\mathbf{r}_1-\mathbf{r}_2)\delta(\mathbf{r}_3-\mathbf{r}_4). \end{aligned} \tag{2.61}$$

Inserting this equation in Eq.(2.60) we obtain an integral equation for $F(\mathbf{r}_1,\mathbf{r}_3)$

$$F(\mathbf{r}_1,\mathbf{r}_3)=n^2|t|^4|G(\mathbf{r}_1,\mathbf{r}_3)|^2+n|t|^2\int d\mathbf{r}'|G(\mathbf{r}_1,\mathbf{r}')|^2F(\mathbf{r}',\mathbf{r}_3). \tag{2.62}$$

The most crossed diagrams can be summed to give

$$<C(\mathbf{r}_1,\mathbf{r}_2,\mathbf{r}_3,\mathbf{r}_4)>=F(\mathbf{r}_1,\mathbf{r}_3)\delta(\mathbf{r}_1-\mathbf{r}_4)\delta(\mathbf{r}_2-\mathbf{r}_3). \tag{2.63}$$

We only have to solve one integral equation to obtain both the contributions of the ladder diagrams and the most crossed diagrams. This a tremendous reduction of the scattering problem.

2.2.3 Diffusion equation

Let us first discuss the ladder approximation of the Bethe-Salpeter equation, which is obtained by retaining only the first diagram of the irreducible Vertex U, see Eq. (2.55). The ladder approximation (or equation) describes the dominant transport behaviour inside a disordered system and leads to diffuse propagation in the bulk of the scattering medium. The diffuse intensity in the disordered medium can be found by integrating over the reduced incident intensity. The integration should be restricted to the dimensions of the scattering medium

$$\begin{aligned} I(\mathbf{r}_1) &= \frac{1}{n|t|^2}\int_V d\mathbf{r}_2 L(\mathbf{r}_1,\mathbf{r}_2)|\Psi_{coh}(\mathbf{r}_2)|^2 \\ &= |\Psi_{coh}(\mathbf{r}_1)|^2 + n|t|^2\int_V d\mathbf{r}'|G(\mathbf{r}_1,\mathbf{r}')|^2 I(\mathbf{r}'). \end{aligned} \tag{2.64}$$

Here we see a new contribution that we have not yet encountered in the expansion of the amplitude propagator, i.e. scattering of the intensity.

The diffuse intensity will depend only on the z-coordinate if the scattering medium is slab-like or semi-infinite and the incident light a plane wave. The direction of the incident wave can make an angle θ_i with the surface normal of the scattering medium. We can integrate Eq. (2.64) over the coordinates parallel to the slab and arrive at the Milne equation. Setting the incident flux $I_0 = 1$ and introducing the optical depth τ by $z = \tau l_{ex}$, and the optical thickness b by $L = bl_{ex}$, the Milne equation reads

$$I(\tau) = \exp(-\tau/\mu_i) + \frac{a}{2}\int_0^b d\tau' E_1(|\tau-\tau'|)I(\tau'), \tag{2.65}$$

with $\mu_i = \cos\theta_i$ and $E_1(y)$ the exponential integral $E_1(y) = \int_1^\infty 1/x\exp(-xy)dx$. The equation was first derived by E.A. Milne.[9] Solving the Milne equation is essentially the same as solving the Radiative Transfer equation for isotropic scatterers.[10]

In the bulk of the system, the source term from the incoming beam will be negligible. Hence, the diffuse intensity in the bulk is subject to the equation

$$I(\mathbf{r}) = n|t|^2\int d\mathbf{r}' \mid G(\mathbf{r},\mathbf{r}') \mid^2 I(\mathbf{r}'). \tag{2.66}$$

The diffusion approximation is the assumption that $I(\mathbf{r})$ is a slowly varying function of $\mathbf{r}$, and $I(\mathbf{r}')$ can be approximated by a second order Taylor expansion

$$I(\mathbf{r}') = I(\mathbf{r}+(\mathbf{r}'-\mathbf{r})) = I(\mathbf{r})+(\mathbf{r}-\mathbf{r}')\cdot\nabla I(\mathbf{r})+\frac{1}{2}(\mathbf{r}-\mathbf{r}')(\mathbf{r}-\mathbf{r}'):\nabla\nabla I(\mathbf{r}). \tag{2.67}$$

Using this Taylor expansion for the integrand of Eq. (2.66) yields two terms, the linear term in $(\mathbf{r}-\mathbf{r}')$ is zero because of symmetry. We find the stationary diffusion equation

$$\begin{aligned} I(\mathbf{r}) &= aI(\mathbf{r}) + \frac{1}{3} l_{ex}^2 \nabla^2 I(\mathbf{r}), \\ \Rightarrow \Delta I(\mathbf{r}) &= \frac{3(1-a)}{l_{ex}^2} I(\mathbf{r}) \equiv \frac{1}{L_a^2} I(\mathbf{r}), \end{aligned} \tag{2.68}$$

where we have defined the absorption length $L_a \equiv \sqrt{l_{ex}^2/3(1-a)}$. For non-absorbent systems there will be a linear solution to the diffusion equation.

The boundary conditions accompanying the diffusion approximation are ambiguous because the diffusion approximation does not hold at the boundaries. The source term I_0, for the diffusion equation, should be a diffuse intensity, which is the light scattered out of the incident wave. At the transmission side of the slab, there will be a region where the chance for the light to escape the medium without being scattered is high. A good description of the diffuse intensity at the boundaries is crucial to calculate how much light is coupled into and out of the system. On the other hand, one seeks analytical formulae that do not require solving of integral equations. Occasionally, both conditions can be met. A pragmatic approach is to replace the exponentially decaying source function by a diffuse source located at an injection depth,[11] and at the transmission side, to locate the point where the diffuse intensity is zero outside the slab. The boundary conditions for the diffuse intensity then become for a slab-like scattering medium with thickness L

$$I(z=-z_0) = I_0 \quad \text{and} \quad I(z=L+z_0) = 0. \tag{2.69}$$

We expect the extrapolation length z_0 to be proportional to the mean-free path because randomization of the direction of the incident light will be achieved after a few scattering events. Comparison with numerical solutions of the Milne Equations yields the locations of the mathematical boundaries (trapping planes): $z_0 = 0.7104 l_{ex}$.[12] Hence, the diffuse intensity in the diffusion approximation is given by

$$I(z) = I_0 \frac{L + z_0 - z}{L + 2z_0}. \tag{2.70}$$

The total transmission is given by the intensity at $z=L$. Since the extrapolation length is proportional to the mean-free path we find for the transmission coefficient

$$T = \frac{1}{I_0} I(z=L) = \frac{z_0}{L+2z_0} = -z_0 \frac{1}{I_0} \left.\frac{dI(z)}{dz}\right|_{z=L+z_0} \propto \frac{l_{ex}}{L}. \tag{2.71}$$

The intensity Green's functions or diffusion propagator $P_0(\mathbf{r},\mathbf{r}')$ for the infinite medium can be derived by applying the same approximations to Eq. (2.60) which yields

$$(\Delta - L_a^{-2}) P_0(\mathbf{r},\mathbf{r}') = -\delta(\mathbf{r}-\mathbf{r}'), \tag{2.72}$$

with the solution (for three dimensions),

$$P_0(\mathbf{r},\mathbf{r}') = \frac{a^2}{4\pi|\mathbf{r}-\mathbf{r}'|}\exp(-|\mathbf{r}-\mathbf{r}'|/L_a). \tag{2.73}$$

The finiteness of the scattering medium can be taken into account again by setting boundary conditions for the diffusion propagator. Since the diffuse intensity is zero at the trapping planes, the diffusion propagator must be zero too at these locations. The boundary conditions can be fulfilled by mirroring in the trapping planes, which is a similar approach as in electromagnetic boundary problems.[5] We obtain the diffusion propagator for a slab of thickness L

$$\begin{aligned} P(\mathbf{r},\mathbf{r}') &= \sum_{n=-\infty}^{n=\infty} P_0(x-x', y-y', z-z'-2n(L+2z_0)) - \\ &\qquad P_0(x-x', y-y', z+z'+2z_0-2n(L+2z_0)). \end{aligned} \tag{2.74}$$

For a semi-infinite medium only one mirror image is needed, i.e. the $n = 0$ terms remain.

2.2.4 Bistatic coefficients

The reflected and transmitted intensities are conveniently described by bistatic coefficients. A bistatic coefficient is the observed intensity in a certain direction for normalized incident intensity, and corrected for the distance to the scattering medium and the observed area A,

$$\gamma(\mu_i,\mu_s) \equiv \frac{2\pi r^2}{A} I(\mathbf{r}), \tag{2.75}$$

with $\mu_i = \cos\theta_i$, $\mu_s = \cos\theta_s$, and θ_i the direction of the incident light and θ_s the direction of observation (both with respect to the surface normal pointing outwards).

The intensity outside the scattering medium I_{out} is given by

$$\begin{aligned} I_{out}(\mathbf{r}) &= |\Psi_{coh}(\mathbf{r})|^2 + \int d\mathbf{r}' G(\mathbf{r}',\mathbf{r})G^*(\mathbf{r}',\mathbf{r})I(\mathbf{r}') \\ &= |\Psi_{coh}(\mathbf{r})|^2 + \\ &\int d\mathbf{r}_1 d\mathbf{r}_2 d\mathbf{r}_3 d\mathbf{r}_4 G(\mathbf{r},\mathbf{r}_1)G^*(\mathbf{r},\mathbf{r}_2)R(\mathbf{r}_1,\mathbf{r}_2,\mathbf{r}_3,\mathbf{r}_4)\Psi_{coh}(\mathbf{r}_3)\Psi^*_{coh}(\mathbf{r}_4). \end{aligned} \tag{2.76}$$

The two Green's functions transport the intensity inside the scattering medium towards the observation point $\mathbf{r}$.

The boundaries of the scattering medium are considered to be ideal, i.e. reflection of the light leaving the sample is not taken into account. In Chapter 5 we will improve on this assumption. For reflection, the Green's function $G(\mathbf{r}, \mathbf{r}')$ for $\mathbf{r}'$ inside and $\mathbf{r}$ far outside the slab can be approximated by

$$G(\mathbf{r}, \mathbf{r}') \approx \frac{1}{4\pi r} \exp(-ik_0 r + i\mathbf{K} \cdot \mathbf{r}'), \tag{2.77}$$

where we have used that

$$iK|\mathbf{r} - \mathbf{r}'| \approx iK(r - \frac{\mathbf{r} \cdot \mathbf{r}'}{r}) \approx ik_0 r - i\mathbf{K} \cdot \mathbf{r}'. \tag{2.78}$$

The transverse component of the outgoing wavevector $\mathbf{K}$ must be continuous at the boundary, hence we write

$$K_z = \sqrt{K^2 - k_0^2 \sin^2 \vartheta_s} \approx k_0 \cos \vartheta_s - \frac{i}{2l_{ex} \cos \vartheta_s} = k_0 \cos \vartheta_s + \frac{i}{2l_{ex}\mu_s} \tag{2.79}$$

and find for the Green's function for the backscatter direction

$$G(\mathbf{r}, \mathbf{r}') = \frac{1}{4\pi r} \exp(-ik_0 r) \exp(i\mathbf{K}_\mathbf{b} \cdot \mathbf{r}'), \tag{2.80}$$

with the outgoing wavevector defined as

$$\mathbf{K}_b = (k_0 \cos \phi_s \sin \vartheta_s, k_0 \sin \phi_s \sin \vartheta_s, k_0 \cos \vartheta_s + \frac{i}{2l_{ex}\mu_s}) \equiv \mathbf{k}_s + \frac{i}{2l_{ex}\mu_s}\hat{\mathbf{z}}. \tag{2.81}$$

Similarly, the Green's function for transmission is given by

$$G(\mathbf{r}, \mathbf{r}') = \frac{1}{4\pi r} \exp(-ik_0 r) \exp(i\mathbf{K}_t \cdot (\mathbf{r}' - L\hat{\mathbf{z}})), \text{ with } \mathbf{K}_t = \mathbf{k}_s - \frac{i}{2l_{ex}\mu_s}\hat{\mathbf{z}}. \tag{2.82}$$

We find for the reflection bistatic coefficient

$$\begin{aligned} \gamma(\mu_i, \mu_s) &= \frac{1}{8\pi A} \iiiint_{slab} d\mathbf{r}_1 d\mathbf{r}_2 d\mathbf{r}_3 d\mathbf{r}_4 \times \\ & e^{-(\tau_1+\tau_2)/2\mu_s} e^{i\mathbf{k}_s\cdot(\mathbf{r}_1-\mathbf{r}_2)} R(\mathbf{r}_1, \mathbf{r}_2, \mathbf{r}_3, \mathbf{r}_4) e^{-(\tau_3+\tau_4)/2\mu_i} e^{-i\mathbf{k}_i\cdot(\mathbf{r}_3-\mathbf{r}_4)}, \end{aligned} \tag{2.83}$$

and for the transmission bistatic coefficient

$$\begin{aligned} \gamma(\mu_i, \mu_s) &= \frac{e^{-b/\mu_s}}{8\pi A} \iiiint_{slab} d\mathbf{r}_1 d\mathbf{r}_2 d\mathbf{r}_3 d\mathbf{r}_4 \times \\ & e^{(\tau_1+\tau_2)/2\mu_s} e^{i\mathbf{k}_s\cdot(\mathbf{r}_1-\mathbf{r}_2)} R(\mathbf{r}_1, \mathbf{r}_2, \mathbf{r}_3, \mathbf{r}_4) e^{-(\tau_3+\tau_4)/2\mu_i} e^{-i\mathbf{k}_i\cdot(\mathbf{r}_3-\mathbf{r}_4)}. \end{aligned} \tag{2.84}$$

It is instructive to calculate separately the contributions to the reflected intensity of single scattering, the ladder and the most crossed diagrams. For the single scattering bistatic coefficient $\gamma_s(\mu_i, \mu_s)$ we find

$$\begin{aligned} \gamma_s(\mu_i, \mu_s) &= \frac{1}{8\pi A} \iiiint_{slab} d\mathbf{r}_1 d\mathbf{r}_2 d\mathbf{r}_3 d\mathbf{r}_4 n|t|^2 \delta(\mathbf{r}_{12})\delta(\mathbf{r}_{13})\delta(\mathbf{r}_{14}) \times \\ & \exp\left[-\frac{\tau_1+\tau_2}{2\mu_i} - \frac{\tau_3+\tau_4}{2\mu_s}\right] \exp[i\mathbf{k}_s \cdot (\mathbf{r}_1 - \mathbf{r}_2) - i\mathbf{k}_i \cdot (\mathbf{r}_3 - \mathbf{r}_4)] \\ &= \frac{An|t|^2 l_{ex}}{8\pi A} \int_0^b d\tau_1 \exp[-\tau_1(\frac{1}{\mu_i} + \frac{1}{\mu_s})] \\ &= \frac{a\mu_i\mu_s}{2(\mu_i+\mu_s)} \left(1 - \exp[-b(\frac{1}{\mu_i} + \frac{1}{\mu_s})]\right). \end{aligned} \tag{2.85}$$

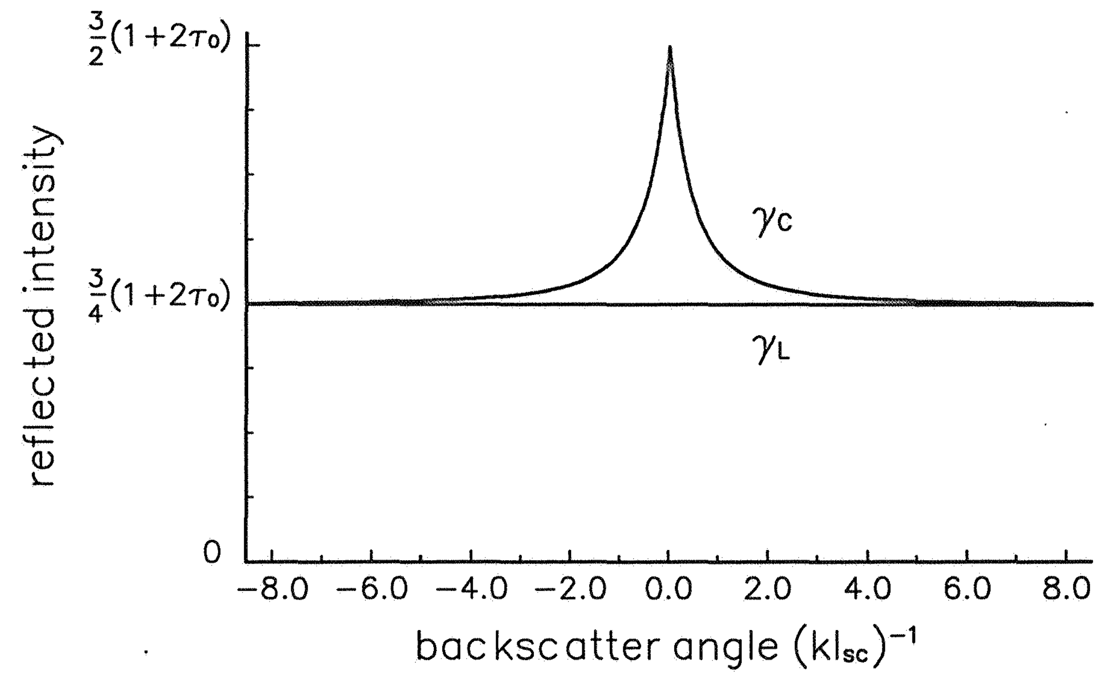

Figure 4: Reflected intensity of a semi-infinite random medium is plotted as a function of the backscatter angle. The increased intensity near the backscatter direction is a consequence of constructive interference of time reversed waves.

Similarly, we find for the bistatic coefficient for the diffuse reflection $\gamma_L(\mu_i, \mu_s)$

$$\gamma_L(\mu_i, \mu_s) = \frac{1}{8\pi A\mu_i}\iint_{slab} d\mathbf{r}_1 d\mathbf{r}_3 F(\mathbf{r}_1, \mathbf{r}_3)\exp[-\frac{\tau_1}{\mu_s} - \frac{\tau_3}{\mu_i}], \tag{2.86}$$

and for the most crossed diagrams

$$\begin{aligned}\gamma_C(\mu_i, \mu_s) &= \frac{1}{8\pi A}\iint_{slab} d\mathbf{r}_1 d\mathbf{r}_3 F(\mathbf{r}_1, \mathbf{r}_3)\times \\ &\exp[-(\frac{1}{2\mu_s} + \frac{1}{2\mu_i})(\tau_1 + \tau_3)]\exp[i(\mathbf{k}_s + \mathbf{k}_i)\cdot(\mathbf{r}_1 - \mathbf{r}_3)].\end{aligned} \tag{2.87}$$

The function $F(\mathbf{r}_1, \mathbf{r}_2)$ should be solved (numerically) from Eq. (2.62). Analytical expressions for Eqs. (2.86) and (2.87) can be obtained by considering the diffusion approximation for $F(\mathbf{r}_1, \mathbf{r}_2)$. The function $F(\mathbf{r}_1, \mathbf{r}_2)$ is approximated by the diffusion propagator as given by Eq. (2.74).

The reflected intensity for a semi-infinite medium with non-absorbent particles (a=1) is found to be

$$\gamma_L(\mu_i, \mu_s) = \frac{3\mu_i\mu_s}{2}\left(\tau_0 - \frac{\mu_i\mu_s}{\mu_i + \mu_s}\right), \tag{2.88}$$

and

$$\gamma_C(\mu_i, \mu_s) = \frac{3}{4} \frac{1}{(\alpha+\nu)^2 + u^2} \left(\frac{1}{\nu} + \frac{1}{\alpha}(1 - \exp(-2\alpha\tau_0)) \right), \tag{2.89}$$

with

$$\alpha = k_0 l_{sc} \sqrt{\sin^2\theta_s + \sin^2\theta_i} \quad \nu \equiv \frac{1}{2\mu_i} + \frac{1}{2\mu_s}, \quad u \equiv k_0 l_{sc}(\mu_i - \mu_s), \quad l_{sc}\tau_0 = z_0.$$

The scattering mean-free path is given by $l_{sc} = 4\pi/n|t|^2$ and equal to the extinction mean-free path for non-absorbent particles.

In Fig. 4, we plot the diffusion result for the reflected intensity as a function of the backscatter angle, normally incident light is assumed. We observe an increased intensity in the backscatter direction that is entirely due to the most crossed diagrams. It is an interference contribution of counter propagating or time reversed amplitudes. The angular width of the interference contribution is inversely proportional to $k_0 l_{sc}$. The functional form for the interference contribution is not differentiable at $\theta = 0$.

In the exact backscatter direction ($\theta = 0$), the intensity is twice that of the diffuse background: $\gamma_L(1,1) = \gamma_C(1,1) = \frac{3}{4}(1 + 2\tau_0)$. This is an exact relation when recurrent scattering events are neglected. This can be seen as follows: if $A_i(\mathbf{k}_i, \mathbf{k}_f)$ denotes the amplitude of a reflected wave with initial direction $\mathbf{k}_i$, first scattered at $\mathbf{r}_i$ and last scattered at $\mathbf{r}_f$ in the final direction $\mathbf{k}_f$, we can write down the reflected intensity as a coherent sum over amplitudes of all possible reflection paths

$$\begin{aligned} I(\mathbf{k}_i, \mathbf{k}_f) &= \left|\sum_i A_i\right|^2 = \sum_{i,j} A_i A_j^* \\ &= \sum_{i=j} A_i A_j^* + \sum_{i=-j} A_i A_j^* + \sum_{i \neq j, i \neq -j} A_i A_j^*. \end{aligned} \tag{2.90}$$

The summation indices i, j run over all possible paths (we have omitted the wavevector dependency of each amplitude in Eq. (2.90)). The first term on the right hand side of Eq. (2.90) is the diffuse scattered intensity: amplitude and complex conjugate travel side by side through the sample (ladder diagrams). The second term is the interference contribution where the complex conjugate follows the same path as the amplitude but in reversed order (most crossed diagrams). This is denoted by $i = -j$ in the summation. The third term yields the speckle pattern that is a wildly fluctuating (in space or direction) random intensity pattern. If we average over the configuration of the scatterers, the speckle term drops out and we retain

$$<I(\theta)> = <\sum_i |A_i|^2> + <\sum_i |A_i|^2 \exp(i\Delta\phi_i)>, \tag{2.91}$$

where $\Delta\phi_i$, given by

$$\Delta\phi_i(\mathbf{k}_i, \mathbf{k}_f) = (\mathbf{k}_i + \mathbf{k}_f) \cdot (\mathbf{r}_i - \mathbf{r}_f), \tag{2.92}$$

is the phase difference between the direct wave i and its counter-propagating partner. In the exact backscatter direction ($\mathbf{k}_i = -\mathbf{k}_f$) the phase difference $\Delta\phi$ is zero for all paths, hence

$$<I(0)>= 2\times <\sum_i |A_i|^2> . \tag{2.93}$$

For large backscatter angles, the second term of Eq. (2.91) depends on the position of the scatterers and thus averages out to zero. It follows that

$$<I(\theta \gg 0)>=<\sum_i |A_i|^2> . \tag{2.94}$$

Therefore, the enhancement factor, $<I(0)>/<I(\theta \gg 0)>$, of coherently backscattered light is exactly 2. Absorption of light inside the disordered system does not affect the enhancement factor, because the intensity of the diffuse background and the coherently backscattered light are reduced equally. The shape of the backscatter cone will change for absorbent disordered media, the triangular shape at $\theta = 0$ will be rounded off.

The diffuse transmission for thick slabs can be calculated as

$$\gamma_L(\mu_i, \mu_s) = \frac{3\mu_s\mu_i}{2}\frac{(\tau_0 + \mu_s)(\tau_0 + \mu_i)}{b + 2\tau_0}. \tag{2.95}$$

The transmission is inversely proportional to the thickness of the slab, which was also obtained directly from the diffusion equation in the previous section.

2.3 Anisotropic scattering

Let us briefly discuss the impact of anisotropic scattering. We will consider the time dependent transport equation in order to arrive at the time dependent diffusion equation which we will need in this thesis. The time dependent transport equation is given by[10],[12]-[14]

$$\delta_t \frac{\partial}{\partial t} I(\mathbf{r}, \hat{\mathbf{s}}, t) + l_{ex}\hat{\mathbf{s}} \cdot \nabla I(\mathbf{r}, \hat{\mathbf{s}}, t) = \frac{a}{4\pi}\int p(\hat{\mathbf{s}}, \hat{\mathbf{s}}') I(\mathbf{r}, \hat{\mathbf{s}}', t) d\hat{\mathbf{s}}' - I(\mathbf{r}, \hat{\mathbf{s}}, t), \tag{2.96}$$

with δ_t being the average time between scattering events, $I(\mathbf{r}, \hat{\mathbf{s}}, t)$ the specific intensity, and $p(\hat{\mathbf{s}}, \hat{\mathbf{s}}')$ the phase function for scattering from direction $\hat{\mathbf{s}}$ to $\hat{\mathbf{s}}'$, and l_{ex} the extinction mean-free path as previously given by

$$l_{ex} = \frac{1}{n(\sigma_{sc} + \sigma_{ab})} = \frac{1}{n\sigma_{ex}} = a l_{sc}. \tag{2.97}$$

Integration of Eq. (2.96) over all angles yields a conservation equation or continuity equation

$$\frac{\partial}{\partial t}I(\mathbf{r},t)+\nabla\cdot\mathbf{J}(\mathbf{r},t)=-\frac{1-a}{\delta_t}I(\mathbf{r},t). \tag{2.98}$$

The angular averaged diffuse intensity or shortly diffuse intensity $I(\mathbf{r},t)$ is related to the specific intensity by

$$I(\mathbf{r},t)=\int\frac{d\hat{\mathbf{s}}}{4\pi}I(\mathbf{r},\hat{\mathbf{s}},t), \tag{2.99}$$

and the diffuse flux vector $\mathbf{J}(\mathbf{r},t)$ by

$$\mathbf{J}(\mathbf{r},t)=\frac{l_{ex}}{\delta_t}\int\frac{d\hat{\mathbf{s}}}{4\pi}I(\mathbf{r},\hat{\mathbf{s}},t)\hat{\mathbf{s}}. \tag{2.100}$$

Multiplying Eq. (2.96) by $\hat{\mathbf{s}}$ and then integrating we find

$$\frac{\delta_t^2}{l_{ex}}\frac{\partial}{\partial t}\mathbf{J}(\mathbf{r},t)+l_{ex}\int\frac{d\hat{\mathbf{s}}}{4\pi}(\hat{\mathbf{s}}\cdot\nabla I(\mathbf{r},\hat{\mathbf{s}},t))\hat{\mathbf{s}}=a\frac{\delta_t}{l_{ex}}<\cos\vartheta>\mathbf{J}(\mathbf{r},t)-\frac{\delta_t}{l_{ex}}\mathbf{J}(\mathbf{r},t), \tag{2.101}$$

where we have noted that

$$\int\frac{d\hat{\mathbf{s}}}{4\pi}d\hat{\mathbf{s}}'p(\hat{\mathbf{s}},\hat{\mathbf{s}}')I(\mathbf{r},\hat{\mathbf{s}}',t)\hat{\mathbf{s}}=\frac{\delta_t}{l_{ex}}<\cos\vartheta>\mathbf{J}(\mathbf{r},t), \tag{2.102}$$

with $<\cos\vartheta>=<\hat{\mathbf{s}}\cdot\hat{\mathbf{s}}'>$ the average scattering angle. The angular distribution of the diffuse intensity is almost uniform since it is subject to a large number of scattering events. Hence, we make the approximation[12]

$$I(\mathbf{r},\hat{\mathbf{s}},t)\approx I(\mathbf{r},t)+\frac{3\delta_t}{l_{ex}}\hat{\mathbf{s}}\cdot\mathbf{J}(\mathbf{r},t), \tag{2.103}$$

and we find

$$\frac{\delta_t^2}{l_{ex}}\frac{\partial}{\partial t}\mathbf{J}(\mathbf{r},t)+\frac{\delta_t}{l_{ex}}(1-a<\cos\vartheta>)\mathbf{J}(\mathbf{r},t)=-\frac{l_{ex}}{3}\nabla I(\mathbf{r},t). \tag{2.104}$$

Finally, we neglect the time derivative of the current in Eq. (2.104) and substitute the remaining equation into Eq. (2.98) to obtain the time dependent diffusion equation

$$\frac{\partial}{\partial t}I(\mathbf{r},t)=D\nabla^2 I(\mathbf{r},t)-DL_a^{-2}I(\mathbf{r},t). \tag{2.105}$$

The diffusion constant D is defined by

$$D=\frac{1}{3}\frac{l_{ex}}{\delta_t}\frac{l_{ex}}{1-a<\cos\vartheta>}=\frac{1}{3}vl_{tr}, \tag{2.106}$$

and the absorption length

$$L_a=\sqrt{l_{ex}l_{tr}/3(1-a)}. \tag{2.107}$$

The transport mean-free path l_{tr} is given by

$$l_{tr} \equiv \frac{1}{n\sigma_{pr}} = \frac{1}{n(\sigma_{ex} - <\cos\vartheta> \sigma_{sc})} = \frac{l_{ex}}{1 - a <\cos\vartheta>}. \tag{2.108}$$

Hence, diffuse processes are determined by the transport mean-free path which is usually larger than the extinction mean-free path. To account for anisotropic scattering, we should replace the extinction mean-free path by the transport mean-free path, in the results of the previous sections. As we will learn in Chapter 6, corrections for low order of scattering processes are necessary. The attenuation of the coherent beam is still given by the extinction mean-free path.

References

[1] H.C. van de Hulst, 'Light scattering by small particles', (Dover, New York, 1957; 1981).

[2] *see for instance:* 'Light scattering by irregularly shaped particles', Ed. D.W. Schuerman, (Plenum, New York, 1979), P.W. Barber and S.C. Hill, 'Light scattering by particles: computational methods', (World Scientific, London, 1990).

[3] G. Mie, *Beitrage zur Optik trüber Medien speziell kolloidaler Metallösungen*, Ann. Phys. **25**, (1908).

[4] C.F. Bohren and D.R. Huffman, 'Absorption and scattering of light by small particles', (Wiley, New York, 1983).

[5] J.D. Jackson, 'Classical electrodynamics', (Wiley, New York, 1975).

[6] U. Frish, *Wave propagation in random media*, 'Probabilistic methods in applied mathematics', edited by A.T. Barucha-Reid, Vol. **I**, 76 (Acad. Press. New York, 1968).

[7] Th.M. Nieuwenhuizen, A. Lagendijk, and B.A. van Tiggelen, *Resonant point scatterers in multiple scattering of classical waves*, Phys. Lett. A **169**, 191 (1992).

[8] L. Tsang and I. Ishimaru, *Backscatter enhancement of random discrete scatterers*, J. Opt. Soc. Am. A **1**, 836 (1984).

[9] E.A. Milne, *Monthly Notices Roy. Astron. Soc. London*, **81**, 361 (1921).

[10] S. Chandrasekhar, 'Radiative transfer', (Dover, New York, 1960).

[11] E. Akkermans, P.E. Wolf, and R. Maynard, *Coherent backscattering of light by disordered media: analysis of the peak line shape*, Phys. Rev. Lett. **56**, 1471 (1986).

[12] A. Ishimaru, 'Wave propagation and scattering in random media', Vol. **I, II**, (Academic press, New York, 1978).

[13] J.J. Duderstadt and W.R. Martin, 'Transport theory', (Wiley, New York, 1979).

[14] Th. M. Nieuwenhuizen, private communication.

Chapter 3

Experimental Setup

This thesis describes an experimental study of multiple scattering of light. We are mainly concerned with angular resolved reflection measurements around the exact backscatter direction. We will describe the experimental setup for the backscatter measurements in detail. Setups required for other experiments, will be described in the chapters where that particular experiment is discussed.

3.1 Light source

The most important requirements for the light source for our experiments are stability of the output power and low divergency of the light beam. The first requirement is important since we scan the detection system around the samples and thus compare intensities measured at different times. The second requirement is important for a high angular resolving power of the detection system.

We use an argon-ion pumped continuous dye-laser, the argon laser operates in all-lines mode. The dye-laser is power stabilized by a feedback loop to the output power supply of the argon-ion laser. At best performance, the intensity fluctuations on the output power of the dye-laser are smaller than a few promille of the total power. A specific wavelength of the dye-laser is usually not required, and we can use the most powerful output wavelength of the dye-laser: 603 nm. Only when circularly polarized light is needed should the wavelength be matched to the requirements of a quarter wave-plate, i.e. 633 nm.

The laser dye *rhodamine 6G* is dissolved in a mixture of methanol and ethylene glycol, (1g *rhodamine* on 50:250 ml methanol to ethylene glycol). The wavelength range of the dye-layer is 580 to 620 nm. Adding *rhodamine B*, this range can be shifted towards the red to include 633 nm. The beam of the dye-laser is astigmatic and highly diverging (100 $mrad$). To reduce both, the beam is spatially filtered and expanded. It is focused with an ocular onto a pinhole (50 μm) and

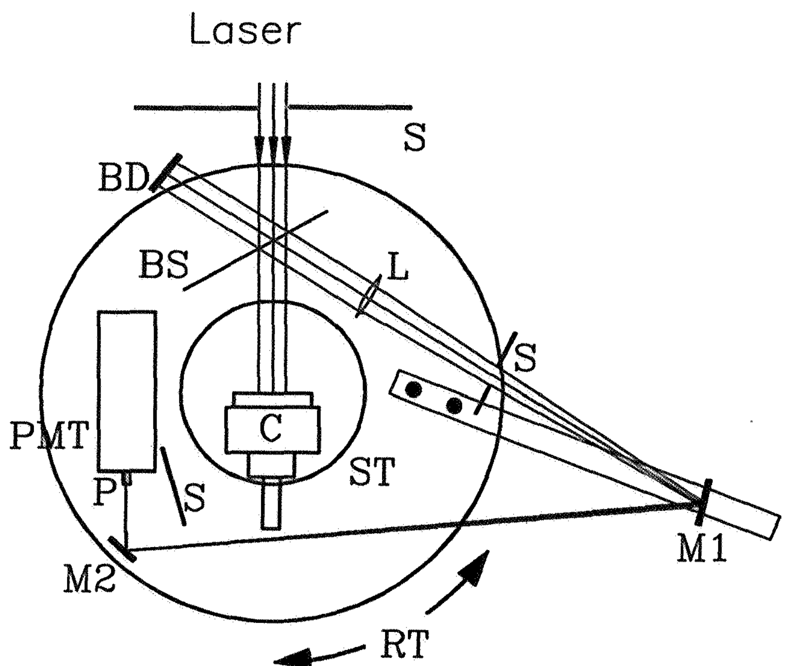

Figure 1: A sketch of the rotating detection system. BS: beamsplitter, BD: beam dump, C: sample cell (see also Fig. 2), L: lens, M1,M2: mirrors, P: polarizer and pinhole, PMT: Photo Multiplier Tube, S: screens, RT: rotation table, ST: stable table.

made parallel with a second lens, F=250 *mm*. Optimal positioning of the second lens is accomplished by comparing the cross section of the beam immediately after the lens with that after it has traversed a distance of approximately 14 meter. The circular cross section of the spatially filtered beam has a diameter of approximately 15 *mm* and is slightly elongated along the vertical direction. It has, to a good extent, a Gaussian intensity profile (width 5 *mm*). The remaining divergence is less then 0.1 *mrad*.

The beam is chopped, before the spatial filter, for phase sensitive detection. The dye-laser power is monitored with a diode to perform ratio measurements; the measured reflected intensity is divided on-line by the signal of this diode.

3.2 Detection system

The samples are illuminated through a beamsplitter that reflects the backscattered light by the samples towards a detector; a Photo Multiplier Tube (PMT), see Fig. 1. A polarizing cube (Glan-Thompson prism) in front of the PMT selects the polarization to be detected.

The sample region is shielded completely from the lasers, leaving an aperture for the incoming beam. The reflected light off the beamsplitter is dumped on a dark glass plate. The dark glass plate is placed at the Brewster angle to suppress illumination of any other components than the sample. In the experiments the background intensity was less than 0.5 percent of the backscattered intensity of a random sample. The background intensity arises from scattering off dirt on the beamsplitter and from noise in the detection system. The measurements are corrected for this background signal.

The samples are slowly rotated to average out the speckle pattern. The axis of rotation is normal to the sample surface. Rotation also prevents sedimentation of the scattering suspensions.

To measure the backscattered intensity as a function of the angle, either the detector should move in the focal plan of an imaging lens, or the detector should circle the sample. In the latter case, a lens is still necessary to have a high angular resolution, and a reasonable intensity on the detector. In practice, the angular resolving power is given by the ratio of the focal waist to the focal length of the lens, for both ways of measurements. The diameter w of the focal waist of a Gaussian beam is given by

$$w = \frac{\lambda F}{\pi W_0} \tag{3.1}$$

with F being the focal length of the lens, and W_0 the width of the Gaussian beam. In our experiments, this Gaussian beam is the scattered light in the direction of observation, with a width that corresponds to the illuminated area on the sample. Since the focal waist is proportional to the focal length, the angular resolving power is determined by the diameter of the illuminated area on the sample only. Hence, the larger the cross section of the incident beam, the higher the angular resolution (a short lens only decreases the length scale). To make use of the angular resolution of the lens-beam system, only the light that passes through the focus should be detected. This can be achieved by a pinhole at the focus position with a diameter at the most equal to the focal waist. In the experiments we use a pinhole of 40 μm in diameter. The pinhole is mounted between the polarizing cube and PMT. The theoretical estimate for the angular resolution of our experimental situation is 40 μrad, in practice we could achieve an angular resolution of 52 μrad.

Optimal positioning of the optical components is accomplished by the following procedure. The backscatter direction is first determined experimentally by the reflection of a mirror, which is positioned so that its reflection passes again through the beamsplitter *and* through the spatial filter. Part of this reflected light is mirrored by the beamsplitter through the imaging lens onto the pinhole mounted on the PMT. By scanning the pinhole and PMT through the focus, the distances between the imaging lens and the pinhole can be optimized by seeking a minimum focal waist. The 'exact' backscatter direction is found by making use of the coherently backscattered light from a disordered sample. By translating the PMT with two micro-screws in the focal plane of the lens, the maximum backscattered intensity from the disordered sample should be found. This defines the backscatter direction. We always used a teflon sample to determine the location of the exact backscatter direction, because teflon yields a backscatter cone with a convenient angular width.

When the detection system is mounted on an x-y-translational stage (translation possible in the plane normal to the optical axis), one can easily switch between two scanning modes: parallel or perpendicular to the initial polarization of the incoming light. In addition, one can also choose to measure the copolarized or crossed polarized light, which allows for four distinct detecting modes. Using a 1000 mm (achromat) lens, the minimum angular increment is 8.3 μrad and samples with a large mean-free path can be measured accurately. The maximum scanning angle, however, is limited by the dimensions of the translation stage and is 1.4 degrees. The maximum scanning angle, and automatically the minimum increment, can be enlarged by using a lens with a shorter focal distance. However, lens faults will show up for large angles, so one cannot arbitrarily increase the total scanning angle in this way.

When a large scanning angle is required (for samples with a short mean-free path) the whole detection system should circle the sample. For this purpose all optical components are placed on a rotation table. The 1 meter light path after the lens is folded on the rotation table. All components are balanced to minimize the stress in the rotation device, the maximal allowed horizontal couple is 4 Nm. A sketch is given in Fig. 1. The minimum rotational increment is 0.002 degrees. The maximum scanning angle is limited by the size of the beamsplitter, which in our case resulted in a maximum scanning angle of 23 degrees. The rotation table and translation stage are scanned by computer controlled steppermotors.

3.3 Experimental difficulties

The enhancement factor, defined as the intensity scattered exactly backwards divided by the diffuse background, is an interesting parameter. There are however several experimental artefacts that can reduce this factor. We will discuss these artefacts and show how they are eliminated in the experimental setup.

The intensity variation within the cross section of the beam should be small on the scale of the mean-free path of the sample. Otherwise a pair of counter-propagating waves will have different amplitudes. The interference contribution of such a pair is smaller than their diffuse contributions, and consequently, the enhancement factor is reduced.

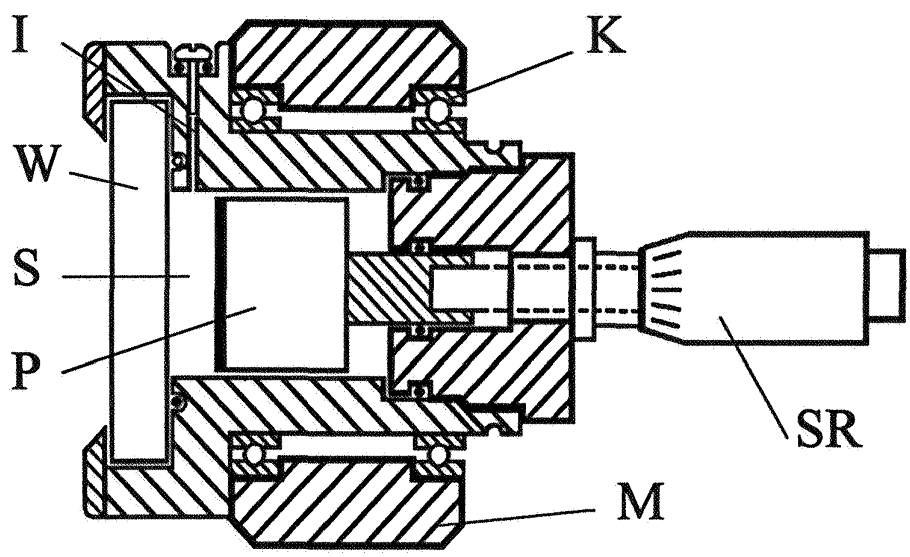

Figure 2: Cross-sectional drawings of the sample container. S: sample area, W: window, I: sample inlet, K: ball-bearing, SR: micro-screw, M: mounting device, P: moveable piston.

The illuminated area on the sample should exactly equal the area seen by the detector. If the illuminated area is smaller, light diffused out of the illuminated area is still detected, but a counter-propagating partner lacks. This light will contribute to the diffuse background only. For the reversed situation, the illuminated area larger than the detected area, a similar process will happen. Now light can diffuse into the detected area, whereas the counter-propagating partner will not be detected. Again, only a contribution is made to the diffuse background.

The first requirement favours a beam with a flat intensity profile, whereas the necessity to fulfil the second requirement can be reduced by the use of a Gaussian intensity profile. For a Gaussian intensity profile, the outer parts of the illuminated area contribute little to the reflected light. When the width of a Gaussian beam is an order of magnitude larger than the mean-free path of the sample, the first requirement is of minor importance. But still for this situation, we have measured a reduction of 10 percent for the enhancement factor when the detectable area is too large.

Measurements on a scattering suspension are necessarily performed through a glass window of a sample cell. Light leaving the sample can now be reflected into the sample a second time by the glass-air interface. Light paths that include such a reflection have consequently traversed a very large distance parallel to the interface, and give rise to an extremely narrow angular interference contribution. This narrow interference pattern cannot be resolved, and consequently the enhancement factor is reduced. Therefore, we use a window that is anti-reflection coated on the air side and thick enough to have the total internal reflected light (from the glass-air interface) falling adjacent to the sample. The extended parts of the window, see Fig. 2, are used to guide this light towards the black cell where it is absorbed. A fluid matching the index of refraction of the window suppresses reflections at that point. The rear side of the sample compartment is a polished RG 830 filter and mounted on a micro-screw. The thickness of the sample is thus variable, ranging from 0 to 1.5 mm. The reflection coefficient of the RG 830 filter is 1.7% at visible wavelength in water (measured at 633 nm).

Chapter 4

Transmission and reflection properties of diffuse scattering media

4.1 Introduction

In this chapter we present several experiments dedicated to particular aspects of light scattering by disordered media. We study interference phenomena for the reflected *and* the transmitted intensity. The main properties of coherent backscattering will be discussed, taking into account the polarization states of the incident and reflected light. Predicted interference phenomena for the transmitted intensity are the forward cone and the anti-specular reflection.[1]-[4] The feasibility to observe these phenomena is investigated. We have performed experiments to determine what kind of corrections follow from the fact that in reality an interface between a scattering and non-scattering medium is rough, and not as in the theoretical considerations perfectly smooth.

4.2 Coherent backscattering

Weak localization or coherent backscattering is understood as constructive interference between time reversed waves. The angular distribution of the coherently backscattered light has a cone shape, therefore the use of the term 'backscatter cone' is quite common. The width of the backscatter cone is inversely proportional to the mean-free path of the disordered medium. Another important quantity is the enhancement factor of the coherently backscattered light. It is defined as the ratio of the intensity in the exact backscatter direction to the intensity of the diffuse background, i.e. at large angle with the backscatter direction. If only the diffusion paths are taken into account, the enhancement factor is exactly two. Several non-diffusive contributions to the reflected intensity alter the magnitude of the enhancement factor.[5] They will be discussed later.

In our theoretical discussion in Chapter 2 of coherently backscattered light we have not taken into account the fact that light is a vector wave. We will come to this now. The enhancement factor is still 2 when the copolarized component of the backscatter light is measured, or the helicity preserving component for the case of circularly polarized incident light. The enhancement factor of the crossed-polarized backscatter cone depends strongly on the single scattering properties of the particles, and is usually smaller than 2.[6]

Recently, it has been shown that the absence of a full crossed-polarized backscatter cone can be understood in terms of geometrical or Berry's phase shifts in addition to the acquired dynamic phase shift ωt.[7] The geometrical phase shift acquired by a vector wave depends strongly on the shape of the path and on the polarization state of the initial and final wave. This can be revealed most easily by drawing a scattering sequence of more than two Rayleigh-scatterers as done in Fig. 1 (the interference term of scattering by two particles is always constructive for both polarization channels). An arrow P_{in} attached to the first scatterer represents the E-field of the light incident from any direction perpendicular to this vector. Projecting this vector onto the direction perpendicularly to the line connecting the first to the second scatterer, yields the amplitude at the next scatterer. Repeating this procedure eventually gives the orientation of the outgoing wavevector P_{out}. In Fig. 1 the amplitude of the time forward path (clock wise propagating) is denoted by P^+_{out}, and P^-_{out} for the time reversed path (counter clock wise). The parallel components of the time forward and time reversed amplitudes P^+_{out} and P^-_{out}, are equal in length and direction ($P^+_{\|} = P^-_{\|}$), whereas the crossed-polarized components differ in length and point in opposite direction ($P^+_{\perp} \neq P^-_{\perp}$). Hence, the crossed-polarized components will not interfere constructively. Depending on the shape of the path (the arrangement of the scatterers) the interference in the crossed-polarized channel thus ranges from completely constructive to destructive. The shape of the scattering paths is strongly influenced by the single scattering properties of the particles.[6]

Another polarization effect is the anisotropic angular distribution of the backscattered light. Measuring the copolarized light by scanning perpendicularly to the incident polarization or parallel, yields a slightly different result. The single scattering properties of the particles are determined if anisotropy is present. In fact, only for small particles, with a phase function close to a Rayleigh phase function, an anisotropic backscatter cone is reported.[6][8]

We will now discuss the impact of non-diffusive scattering contributions on

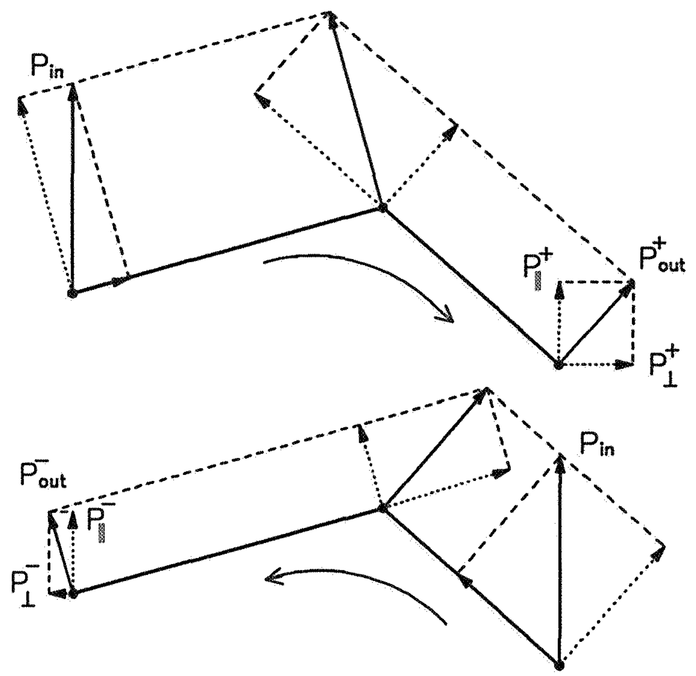

Figure 1: A triple scattering event for both propagation directions (time forward and time reversed), revealing additional phase shifts of the multiply scattered light. All scatterers and vectors lie in the plane of drawing. Each solid arrow denotes the amplitude of the electric field at that point, the dotted arrows are decompositions. It follows that $P_{\|}^{+} = P_{\|}^{-}$, and $P_{\perp}^{+} \neq P_{\perp}^{-}$.

the enhancement factor of the backscatter cone: single scattering and loop diagrams. The time reversed path of a single scattering event is *identical* to the time forward path, hence there cannot be an interference contribution to the singly scattered intensity. The singly backscattered light has an intensity that is constant as a function of angle on the angular scale of the backscatter cone (if the mean-free path is much larger than the wavelength). Therefore, single scattering contributes only to the diffuse background and not to the backscatter cone, thus reducing the enhancement factor.

Loop diagrams are recurrent scattering sequences, the intensity starts and ends at the same scatterer. They can be depicted by the following diagrams

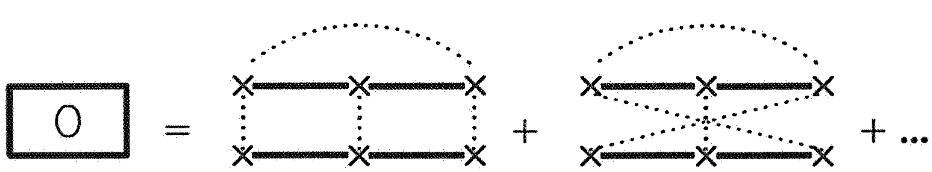

(4.1)

The conventions of the scattering diagrams have been described in Chapter 2. Waves creating a loop do have a counter-propagating partner (the most crossed diagrams) but the interference contribution will be angle independent since start and end points of a loop coincide. In an experiment, the contribution of the loop diagrams cannot be distinguished from the diffuse reflected light, consequently, loop diagrams lower the enhancement factor. Of course, one could reverse this and state that a lowering of the enhancement factor is an indication that loop type scattering events occur.[9] Loops contribute only significantly in very dense random media, because the cross section of the first scatterer and the distance between the first and the last scatterer must still define a significant solid angle in order to have a chance to scatter from the last to the first particle (creating a loop). Thus loop diagrams can be neglected for samples with a large mean-free path.

4.2.1 Measurements of coherently backscattered light

We would like to confirm by experiment that the enhancement factor of coherently backscattered light is indeed 2 as predicted by theory, when only the diffusion paths contribute to the reflected intensity. Elimination of the single scattering contribution requires some experimental effort, whereas loop type scattering events can easily be eliminated by choosing samples with a large mean-free path.

A direct way to filter out the single scattering contribution is to make use of circularly polarized light. Single scattering flips the helicity of the light, whereas the second and higher scattering orders yield both helicity channels. Only the helicity preserving channel shows a backscatter cone for all orders of scattering sequences. Hence, the helicity preserved backscatter cone has an enhancement factor of 2. The helicity preserving component can be filtered by a quarter-wave plate in combination with a polarizer.[10] Light from any source passing subsequently through a polarizer and a quarter-wave plate gets circularly polarized. This light cannot be reflected back along the same path to the light source, provided that only one mirror is used for the reflection (which flips the helicity). The backward reflected light ends, after passing again the quarter-wave plate with a crossed linear polarization state and is blocked by the polarizer. This combination of optical components is often called an optical isolator or optical diode. It is used to decouple the laser cavity from the rest of the experiment.

Another way to eliminate single scattering contributions is by recording 'difference backscatter cones'.[6] The backscattered intensity is measured for various thicknesses of a scattering medium. Subtracting the measured backscattered intensity of a 'thin' slab from the intensity measured for a 'thick' slab retains only light paths that have probed the deep region of the slab. Consequently, the single

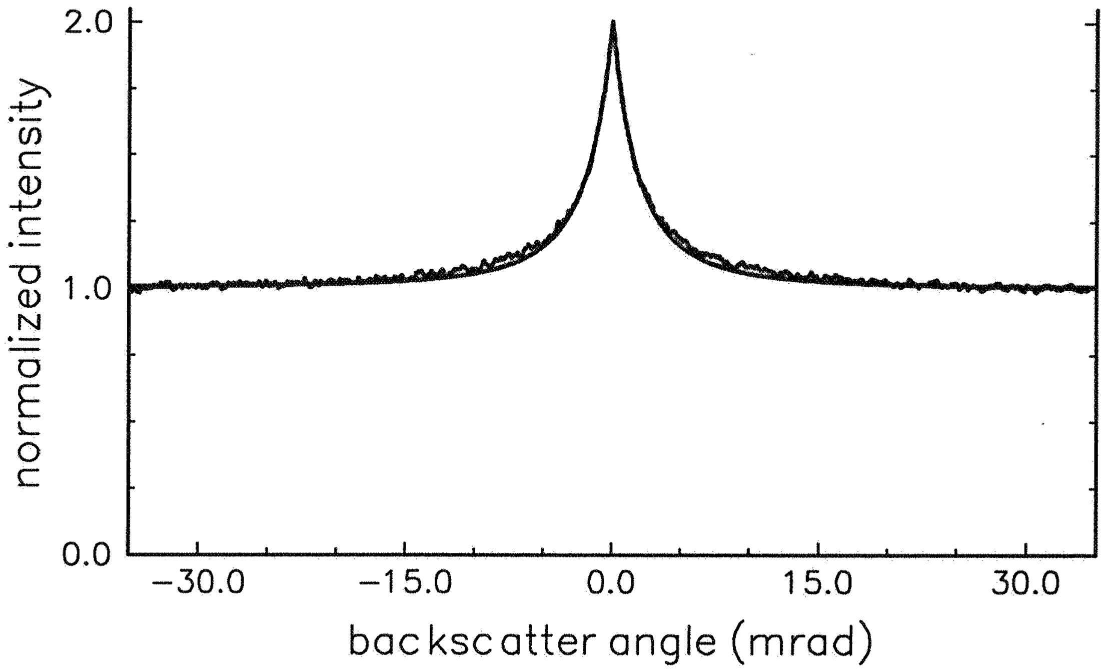

Figure 2: The backscattered intensity of an aqueous suspension of monodisperse polystyrene spheres, ø= 0.265 μm. The thickness of the sample is 1.2 mm. Circularly polarized light has been used. The smooth curve is a calculation using diffusion theory yielding an enhancement factor of 2.005 $\pm$ 0.005.

scattering contribution drops out since single scattering occurs only in the front part of the sample. The contribution of singly scattered light is exponentially damped in the sample: the total contribution from parts deeper than three mean-free paths in the sample is only 5% of the total singly scattered intensity. Thus being more specific on 'thin' and 'thick' slabs: 'thin' means a thickness of around three mean-free paths, and 'thick' means considerable thicker than the thin slab to retain enough intensity after the subtraction. This method gives also insight in the relative contributions of the various scattering orders.

In Fig. 2 we plot the measured intensity as a function of the backscatter angle. The sample is an aqueous suspension containing 10 vol. % monodisperse polystyrene spheres with a diameter of 0.265 μm. The incident light is circularly polarized, the helicity preserving component of the backscattered intensity is measured. A theoretical curve obtained from Eq. (2.89) of Chapter 2 is also shown. We derive from the best fit of theory to the experimental curve an enhancement factor of 2.005 $\pm$ 0.005, and a transport mean-free path 21.8$\pm$0.5 μm.

In Fig. 3 and Fig. 4 we plot 'difference backscatter cones' of a scattering

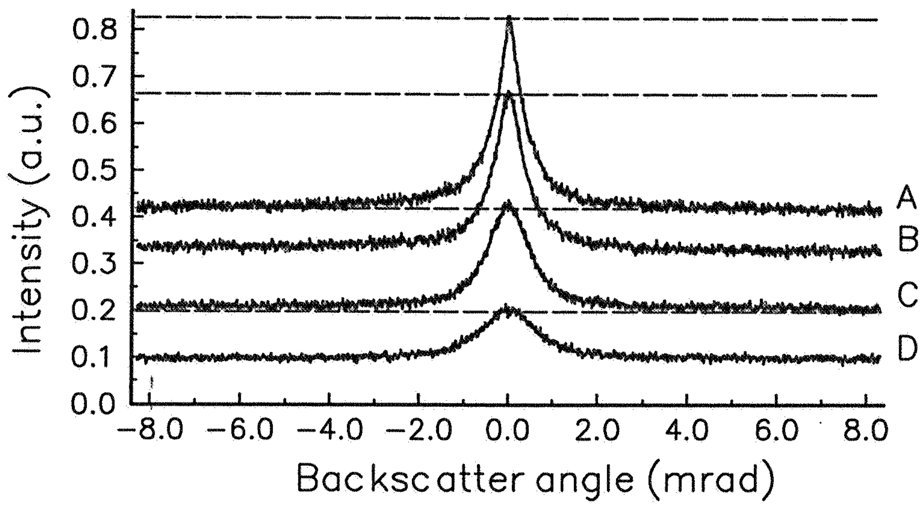

Figure 3: Measured contributions to the backscattered intensity for various penetration depths of the light into the scattering medium. A: $(440-3.8)l_{tr}$, B: $(57-3.8)l_{tr}$, C: $(21-3.8)l_{tr}$, D: $(9.7-3.8)l_{tr}$. $l_{tr} = 17 \pm 1\ \mu m$. Dashed lines indicate twice the intensity of the diffuse background of each curve.

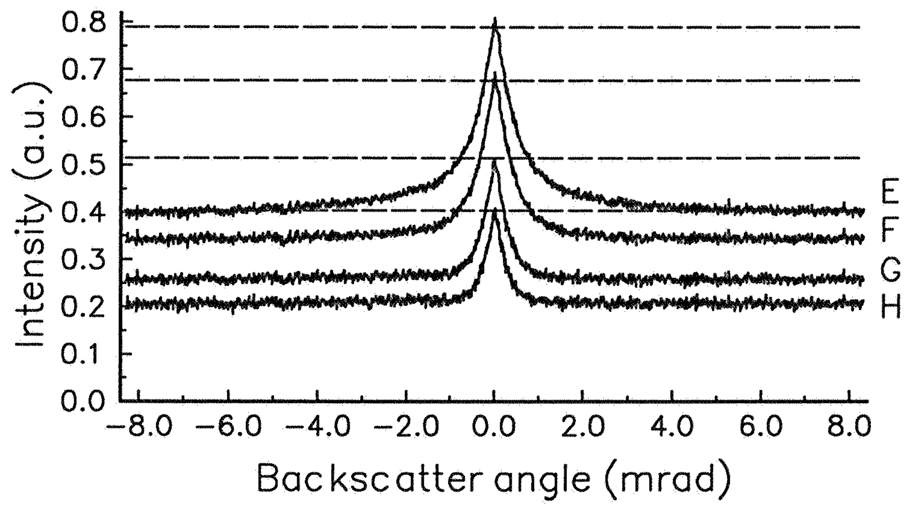

Figure 4: Measured contributions to the backscattered intensity for various penetration depths of the light into the scattering medium. E: $(145-0.88)l_{tr}$, F: $(145-3.8)l_{tr}$, G: $(145-9.7)l_{tr}$, H: $(145-15.6)l_{tr}$. $l_{tr} = 17 \pm 1\ \mu m$. Dashed lines indicate twice the intensity of the diffuse background of each curve.

medium consisting of TiO_2-particles suspended in hexamethylene glycol. Size TiO_2-particles: $240 \pm 70\ nm$, index of refraction TiO_2: 2.7. We have measured the copolarized component of the reflected light by scanning the detector in a plane *perpendicular* to the initial polarization. The transport mean-free path, 17 ± 1 μm, is determined by fitting Eq. (2.89) of Chapter 2 to a backscatter cone measured from a thick slab. In Fig. 3 we plot the backscattered intensity for various thicknesses of the scattering medium. We have subtracted the intensity measured for a thin slab of 65 μm thickness. Hence, we set boundaries for the penetration depth of the light into the scattering medium, thereby keeping the shortest depth constant and varying the largest depth. We clearly see the suppression of long light paths for thin slabs: the top of the backscatter cone has a triangular shape for thick slabs, curves **A** and **B**, and is rounded off for the thinner slabs, curves **C** and **D**. A triangular shape indicates a strong contribution of light that has traversed a large distance parallel to the sample boundary, and that has therefore probed the deeper part of the sample. These long paths are cut off when the sample is thin. In Fig. 4 we vary the boundary for the smallest penetration depth. Now we observe the opposite, i.e. the suppression of the short paths. The backscatter cone becomes sharper the deeper the difference slab is situated in the sample. This behaviour is confirmed by diffusion theory.[2]

The values of the enhancement factor of the helicity preserving component of the backscattered light and that of the difference cones are all within the boundaries 1.98 to 2.02. This fully confirms the theoretical prediction that the enhancement factor of coherently backscattered light is 2 when only diffusion paths contribute.

To end this section we demonstrate the anisotropy in the angular distribution of the backscattered light and give an example of a crossed-polarized backscatter cone. In Fig. 5 we plot the measured intensity of the copolarized backscattered light for two scanning directions of the detector. When we scan the detector in the plane of the incident polarization, the intensity of the backscatter cone decreases slower with increasing backscatter angle than when we scan perpendicularly to the incident polarization. This result was also found earlier in Ref. [6]. In Fig. 6 we plot the measured backscattered intensity for the copolarized and the crossed-polarized component. Two things should be noticed: the diffuse background for the copolarized component is higher than that for the crossed-polarized one since complete depolarization of the incident light is established only after a few scattering events. Secondly, the crossed-polarized backscatter cone has a low enhancement factor and a blunt top indicating that only low order of scattering processes contribute. According to Ref. [3] the backscattered intensity in the crossed-polarized channel is proportional to θ^{-2} for large backscatter angles, in contrast to the copolarized backscatter cone that, according to Ref. [3], decays as θ^{-1}. Besides the fact that in the case of a backscatter measurement it is difficult to distinguish between a θ^{-1} or a θ^{-2}-decay, already the prediction for the copolarized backscatter cone

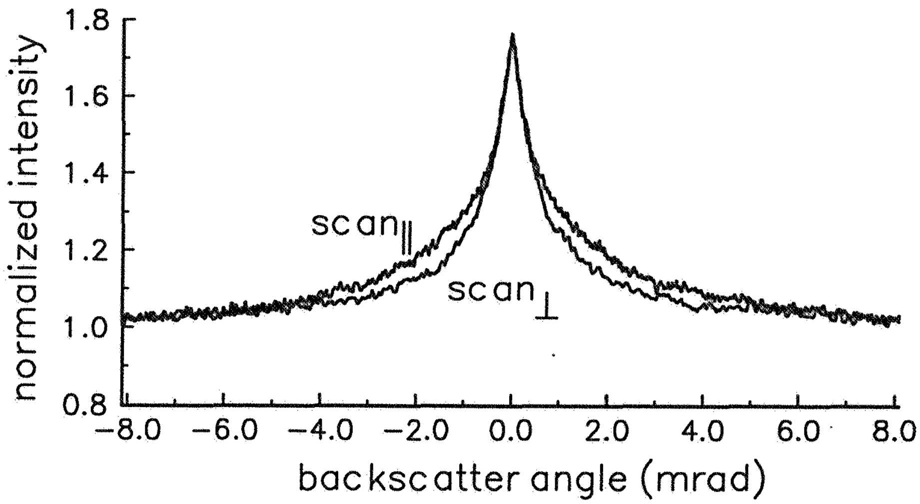

Figure 5: **Copolarized backscattered intensity from suspended monodisperse latex spheres ϕ= 0.215 μm for two scanning directions: detector scanned parallel to the polarization of the incident light ($\parallel$), and perpendicular ($\perp$).**

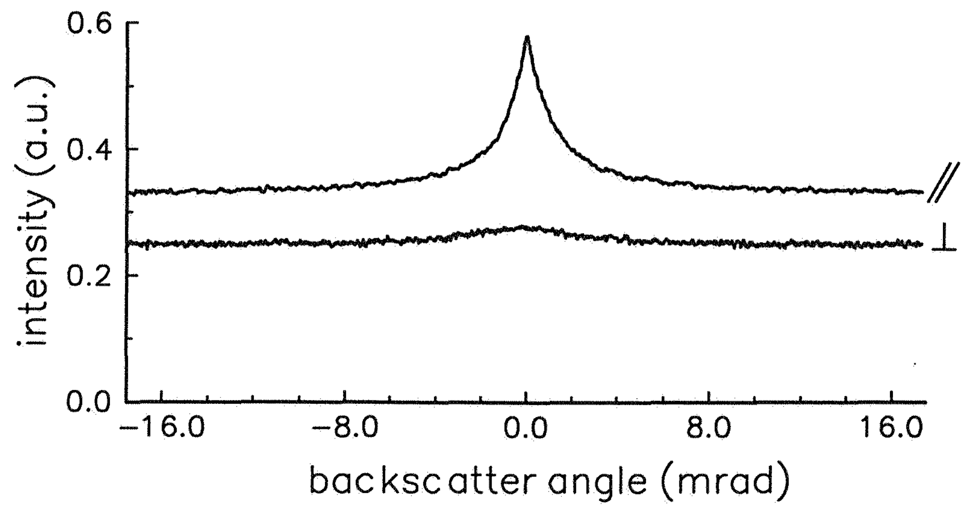

Figure 6: **The intensity of the copolarized component ($\parallel$) and the crossed-polarized component ($\perp$) of the backscattered light are plotted. Sample: 3.8 vol % suspension of 0.215 μm latex spheres.**

is not confirmed by the experiments. Moreover, experiments for the copolarized backscatter cone indicate a θ^{-2}-decay. One should first understand this discrepancy before exploration of the crossed-polarized backscatter cone on the θ^{-2}-decay can be carried out.

4.2.2 Conclusions

The vector nature of light clearly enriches the multiple scattering problem. The freedom of choosing the initial and final polarization state of the light allows for a detailed study of the coherently backscattered light. The results of such a study should be described by a vector theory that also takes into account the phase function of the scatterers. A scalar wave theory describing coherent backscattering applies only to experiments where the polarization preserving component of the incident light is measured. In this extent we have confirmed the maximum intensity of the reflected intensity to be twice the intensity of the diffuse background, when single scattering and recurrent scattering events are eliminated.

4.3 Forward cone and anti-specular reflection

We have already encountered weak localization as an important interference contribution for the diffusely reflected intensity; the backscattered intensity is enhanced. By exploring in detail the diagrammatic representation for the multiply scattered intensity, interference contributions to the diffusely *transmitted* intensity are found as well.[1]-[4] How important are these interference contributions for the average transmitted intensity, and can they be distinguished from the diffuse transmission in an experiment?

The interference contributions to the transmitted intensity can be depicted by the following types of diagrams

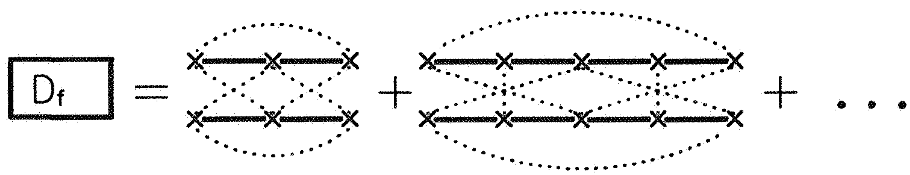

(4.2)

and

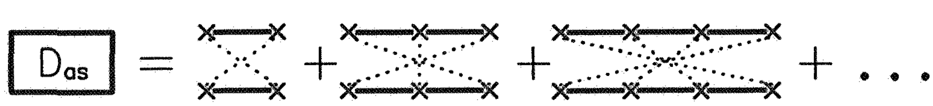

(4.3)

The conventions of the scattering diagrams are described in Chapter 2. For clarity, we have omitted the in- and outgoing lines in the drawings of the diagrams. Again as in the case for reflection, we are dealing with interference of (partly) time reversed waves because this type of interference survives the averaging over scattering configurations. The diagrams in Eq. (4.2) describe the forward cone: an increased intensity with respect to the diffuse background in the forward direction. The simplest scattering sequence contributing to the forward cone contains two scatterers: first diagram of Eq. (4.2). The time forward path starts at particle 1 scatterers to 2 and than back to particle 1. The time reversed path starts at particle 2 and ends via a scattering at particle 1 again at 2. Higher order scattering contributions consist of an arbitrary loop located entirely inside the medium with in- and outgoing lines attached to it. The time forward wave starts at some scatterer contained in the loop, it makes a round trip and then leaves the sample in the forward direction. The time reversed wave does the same but starts at a different location at the loop. The time forward wave will develop the same phase shift as the time reversed wave, and thus they will interfere constructively. The forward cone is essentially a correction to single scattering in transmission.

The diagrams of Eq. (4.3) result in an increased intensity in the direction *opposite* to the reflected beam (at the transmission side): the anti-specular reflection. The diagrams are exactly equal to those yielding the backscatter cone. Only in this case the outgoing lines are directed in the anti-specular direction, see Fig. 7.

We will first argue that an unambiguous observation of the forward cone is extremely difficult, which makes the forward cone as a contribution to the transmitted intensity negligible. As we already know from enhanced backscatter experiments, statements about interference contributions of scalar waves should be carefully translated to vector waves. Although a scalar wave approach applied to vector waves yields enhancement of the backscattered intensity in both polarization channels, geometrical phase shifts are responsible for the absence of fully constructive interference in the crossed-polarized channel. Proceeding as in Fig. 1 in section. 4.2, we find a different geometrical phase shift for the two counterpropagating paths yielding the forward cone. Consequently, the forward cone does not occur for vector waves. A way to circumvent geometrical phase shifts is by restricting the scattering to two dimensions. Experimentally, this can be achieved by using samples consisting of randomly placed parallel fibers that are illuminated perpendicularly to the axis of the fibers by a plane wave. The mapping on scalar waves is perfect if the polarization of the incident light is aligned parallel to the fibers. The sample should be optically thin in order to have a contribution of the forward cone, because the time forward and time reversed waves follow different paths towards the loop. This requirement introduces new problems. If the sample is optically thin, the intensity of the direct transmitted light will be high. It may outweigh the intensity of the multiply scattered light. Spatial filtering of the directly transmitted light can solve this problem, but then one cannot observe the top of the cone anymore.

Furthermore, the forward cone should be distinguished from the singly scattered light, which is in intensity of the same order as the forward cone. For

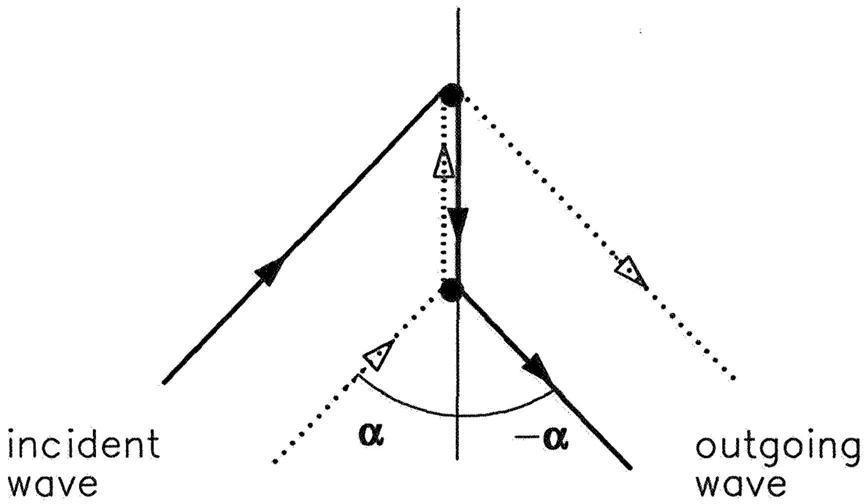

Figure 7: Waves following the scattering sequences depicted will interfere constructively in opposite direction to the reflected light, yielding anti-specular reflection. The incident angle with respect to the sample surface is denoted by α.

experiments with visible light, we are for technical reasons automatically in the situation that the diameters of the fibers are much larger than the wavelength of light. Hence, the fibers will scatter dominantly in the forward direction, which will suppress the forward cone contribution.

According to Ref. [3] the angular distribution of the forward cone will be broad, which makes it less detectable and easily confused with the singly scattered light. In conclusion, it will be very difficult even for mimicked scalar waves to observe the forward cone unambiguously.

We will now concentrate on the anti-specular reflection. The diagrams of the anti-specular reflection, Eq. (4.3), depict two counter propagating waves that will interfere constructively in the direction opposite to that of the reflected beam. A difference with the backscatter cone is that the incoming line of the forward sequence and the *outgoing* line of the *reversed* sequence are not the same, and visa versa. Consequently, the acquired phase shifts of the paths are only equal when all scatterers of the sample lie in the same plane, see Fig. 7. This means that the sample should be a monolayer of scatterers on a flat transparent substrate.

The geometrical phase shift acquired along a scattering path yielding the anti-specular reflection for the copolarized component is equal in both propagating directions. The diagrams involved are the same as those yielding the backscatter cone. The projection of the polarization state of the light leaving the last scatterer onto the outgoing polarization state is over the same angle (but in opposite direction) as in the backscatter situation. Therefore, the additional phase shifts introduced by the vector nature of light do not influence the interference of the time reversed waves in the anti-specular direction (which only holds for the polarization preserving component).

Experimental verification of the existence of anti-specular reflection is easier than for the forward cone. The directly transmitted beam is not in the observation direction, and an anti-specular reflection peak can unambiguously be distinguished from a single scattering pattern by changing the angle of incidence. The angular pattern of singly scattered light is oriented with respect to the incoming light beam only, whereas the direction of the anti-specular reflection is defined with respect to the incident beam *and* the surface normal of the sample. Hence, for fixed detector and light beam, tilting the sample should have no effect on the singly scattered light pattern, whereas an anti-specular peak should follow the tilting angle.

4.3.1 Experiments on anti-specular reflections

The experimental setup to measure the anti-specularly reflected light is similar to that for the backscatter measurements. The difference is that the beamsplitter of the backscatter setup is now replaced by the sample and the sample by a second beam dump (for the transmitted light), see Fig. 8. The beam dumps are dark glass plates placed at Brewster angle to suppress a second reflection.[1] Replacing the sample by a beamsplitter, we did not detect backscattered light from the beam dumps and other components in the anti-specular direction.

One important experimental problem remains to be solved: the speckle pattern coming from the sample should be averaged. We cannot use a suspension of scatterers, because all scatterers should be within a fraction of the wavelength in the same plane. Rotating a solid sample around its surface normal will average the speckle pattern, but this cannot be done in this case either. Contrary to backscatter measurements, the orientation of the sample surface is important; it determines the direction of the anti-specular peak. Wobbling of the sample would average out the peak in the anti-specular reflection. Instead of rotating the sample we place it on a translation stage. During the measurements we gently translate the sample parallel to its surface.

We use a one dimensional diode array to measure the scattered light in a horizontal plane around the anti-specular direction. The longitudinal dimensions of each diode pixel provides us with a possibility to have additional averaging of the speckle pattern. Integration of the scattered light over a solid angle in the

[1] Illumination of e.g. walls by the transmitted and reflected light (by the sample) is exactly in the field of view of the detection system. Any (retro) reflection of the illumination will produce an increased intensity in the anti-specular direction. Therefore, the two beam dumps are needed.

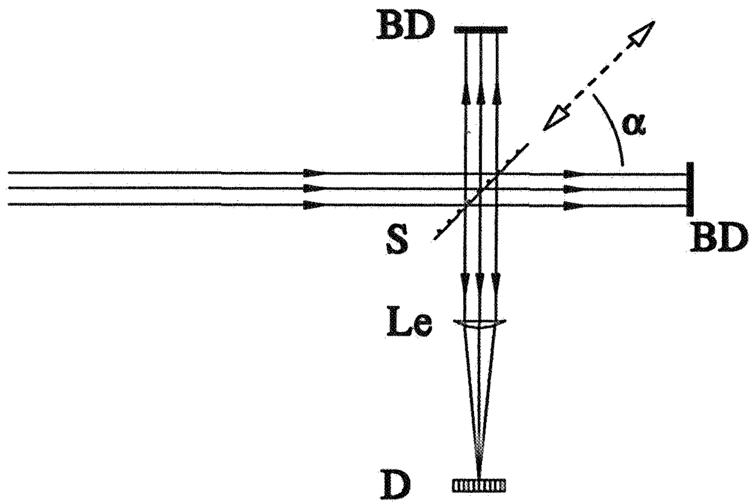

Figure 8: The experimental setup to measure the anti-specular reflection is shown. Labels S: sample, BD: beam dump, Le: lens, D, diode array, α indicates the tilting angle of the sample, the dashed double arrow the direction of translation during the measurement.

vertical direction averages out a fine grained speckle pattern, and has little impact on the angular resolving power in the horizontal plane, which is the direction of interest. A fine grained speckle pattern is produced by a large illuminated area on the sample.

Aligning the setup was done as follows. The incident beam reflected by the sample, is reflected back exactly through the illuminated area on the sample. This direction defines the anti-specular direction. We can now position the diode array and a 50 mm camera lens. The lens in front of the array images outgoing directions from the sample onto positions on the diode array.

We first tried to make a monolayer of particles by submerging glass windows in a suspension of TiO_2-particles in methanol. A thin layer of unknown thickness of TiO_2-particles sets at the glass (it colours the glass purple in transmission). We did not observe any indication towards the existence of anti-specular reflection for these samples. We are successful with a roughly cleaned mirror. The rough 'cleaning method' resulted in small islands of silver on the mirror substrate: a 5 mm thick optically flat window. This sample produces a speckle pattern over almost the whole hemisphere. Angular scans around the anti-specular direction are shown in Fig. 9. Clearly, a peak is visible. Additionally, the peak moves when we tilt the sample as is demonstrated by the other curves in Fig. 9.

A possible alternative explanation for this observation is as follows. The transmitted light through the silver islands is reflected by the window-air inter-

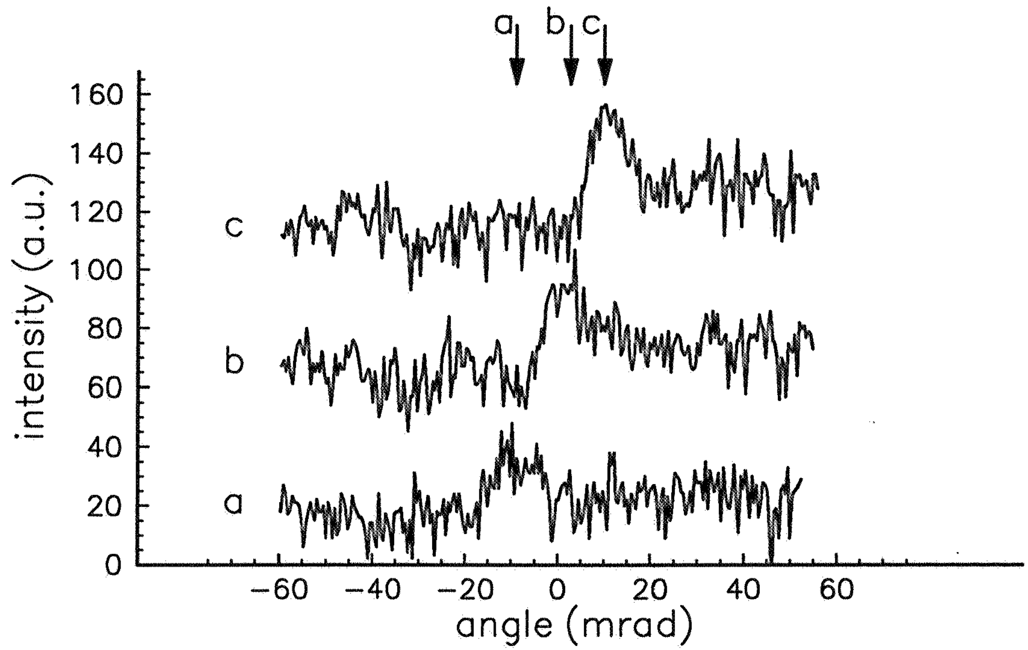

Figure 9: Reflected intensity in the anti-specular direction. The sample is a flat substrate with small islands of silver. Curve **a** and **c** are vertically shifted for presentation reasons. The corresponding arrows indicate the anti-specular direction for each curve.

face onto the silver film again. Enhanced backscattering of this reflected light is exactly in the anti-specular reflection direction. However, an estimation of this contribution yields a peak height of 1.1 relative to the diffuse background. Our observation shows a much higher contribution. Moreover, if this alternative explanation would hold, we should have also seen reflected enhanced backscattering for the thin TiO_2-samples (the submerged windows) and we did not. We conclude that this alternative explanation does not hold, and that we really have observed anti-specular reflection.

Further exploration of this interference phenomenon was not carried out because it seems to occur only on a rough metallic surface. A rough metallic surface is very difficult to control experimentally and to treat theoretically.

4.3.2 Conclusion

Interference phenomena of time reversed waves can also be found in the transmitted light though far less pronounced as in the reflected intensity. Interference corrections are only of small importance for thin slabs, for thick slabs these corrections are completely negligible.

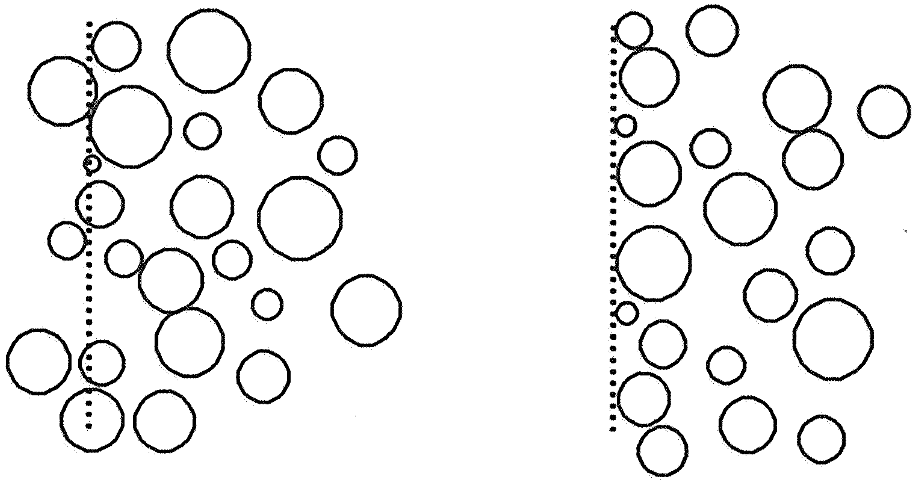

Figure 10: Schematic drawing of two possible boundaries of a scattering medium. A dried sample will usually have a rough boundary (left figure), a suspension of scatterers in a fluid is usually contained by an optically flat window (right figure).

4.4 Rough boundaries of multiply scattering media

Both multiple scattering in a bounded random medium and scattering from rough surfaces exhibit many interesting phenomena,[2] and have therefore been studied extensively.[12]-[15] The combination of the two situations however, has been left unexplored because both cases in themselves are already difficult to treat.

In multiple scattering experiments with light, we will often deal with scattering media bounded by a rough surface, since the scattering medium usually consists of grains suspended in a host material. If we zoom in on the boundary, we will observe something depicted in Fig. 10. The right illustration shows the situation where a scattering medium is abruptly ended by a non-scattering medium, while in the left illustration this is not the case. The right illustration holds typically for grains suspended in a fluid contained by windows, the left one for a dried sample. The typical length-scale of the surface roughness is of course not necessarily equal to that of the disordered medium.

[2]In rough interface scattering problems one is interested in for instance the angular scattering properties like depolarization, blurring of the incident beam and enhanced backscattering as a result of retro-reflection or interference.

Because the refractive indices of sample and air differ, the light is reflected by the sample surface. A surface that is smooth on the length scale of the wavelength will reflect and transmit the light following Snell's refraction laws. A rough interface however, will induce (multiple) scattering of the incident light *before* it enters the disordered sample, and thus changes the properties of the light by which the disordered sample is probed. In the same manner, additional scattering occurs for light leaving the sample. If the sample has a rough surface, the surface reflection will extend over a wide solid angle and might be submerged in the speckle pattern of the light reflected by the bulk of the sample. In a backscatter experiment, this blurred surface reflection will have a similar impact on the coherently backscattered light as single scattering, i.e. it reduces the enhancement factor.

To study the impact of surface roughness on the scattering properties of disordered media, we perform reflection and transmission experiments.

4.4.1 Reflection

We measure the backscattered light from a teflon sample as a function of the angle between the incident light and the surface normal of the sample. We use teflon as a sample because it is chemically inert, which is required for this particular experiment. The polarization of the incident light is perpendicular to the plane through the surface normal and laser beam (s-polarized light) to avoid the occurrence of a Brewster minimum in the specularly reflected light. We measure the copolarized light by moving the detector parallel to the polarization of the incident light. We make the following observation: starting at normal incidence, the enhancement factor of the backscatter cone increases from 1.6 to 1.8, and then saturates for angles of incidence beyond 30 degrees (circles in Fig. 11). With a glass window on top of the teflon sample, and a fluid in between matching the refractive index of the glass (n=1.52), we do not observe this effect (triangles in Fig. 11). The enhancement factor is 1.8, and remains constant when changing the angle of incidence.

The experimental observations can be explained as follows: the refractive index mismatch between teflon and air produces a specular reflection (the refractive index of teflon is 1.4). Because the sample surface is rough, this specularly reflected light is not confined in a small solid angle but blurred. On the angular scale of the backscatter cone the intensity of the blurred specular reflection is constant and thus the enhancement factor is reduced. The glass window on top of the sample reduces the specular reflection at the sample interface; the largest reflection is now that of the glass-air interface. The reduction of the enhancement factor for this situation is only due to single scattering. Apparently, the specular reflection of this teflon sample is blurred over 15 degrees.

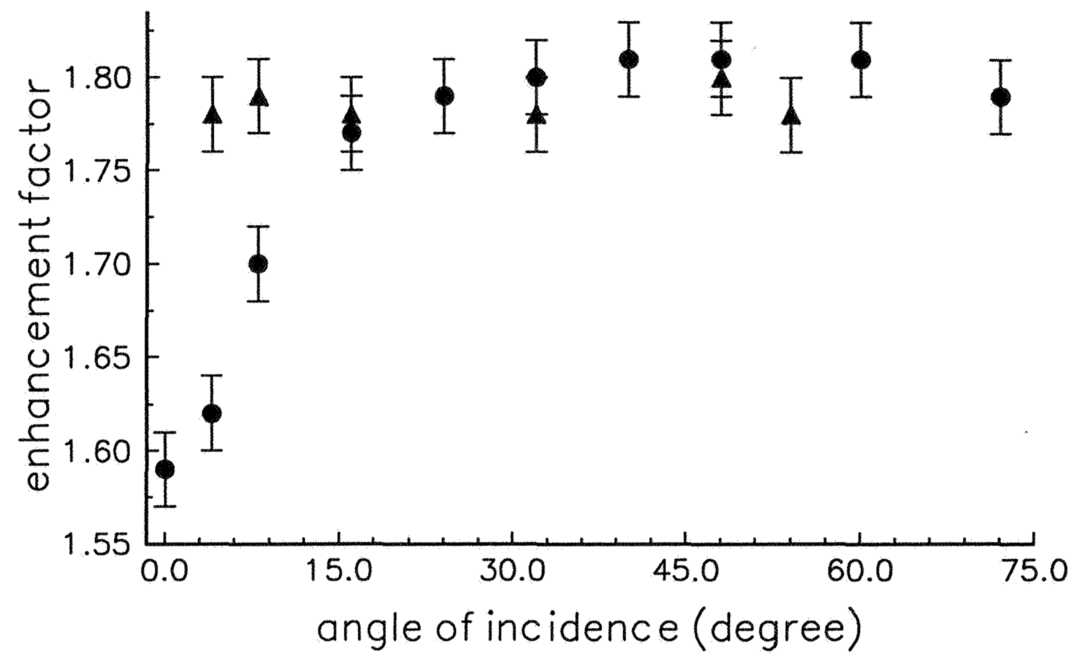

Figure 11: Enhancement factor of the coherently backscattered intensity as a function of the incident angle of s-polarized light. Circles: teflon in air, triangles: teflon behind glass (BK7).

Similar observations are made with TiO_2-samples: dry samples always have a lower enhancement factor than suspensions of TiO_2-particles that are necessarily contained by an optically flat window. Since dry samples have a smaller mean-free path, loop-diagrams might also reduce the enhancement factor.[9].

4.4.2 Angular and polarization resolved transmission

In the bulk of any optically thick scattering medium, light diffuses and has completely lost the correlation with the initial direction of propagation and the polarization state of the incident light. The transmitted light is thus only subject to the scattering properties of the exit surface. This makes the study of the angular and polarization dependency of the transmission a good method to investigate surface roughness of disordered media.

We use samples of different materials with mean-free paths ranging from 1 μm to 160 μm, which were determined by measuring the backscatter cone. The samples have a disc-shape, and are optically sufficiently thick to ensure that the amount of unscattered light is completely negligible. The thickness of the samples is determined by using a calliper or by using a microscope for thin samples. For thin samples, a scratch was made through the sample. A calibrated microscope is then focused at the surface of the sample and on the sample substrate in the scratch. The thickness is obtained from the difference in the focus points. The diameter of the samples is approximately 1.5 *cm*. The roughness of the sample surfaces is expressed in the measured angular divergency of a specularly reflected collimated beam,[3] except for one sample that has too rough a surface to detect any specularly reflected light. The sample properties are summarized in Table 4.1.

The samples are illuminated with unpolarized white light. The transmitted light is restricted by a circular aperture with a diameter of 5 *mm* placed directly on the sample. The sample side with the aperture is carefully placed at the center of rotation of the detector. A 50 *mm* lens focuses the transmitted light onto a photodiode. Both are mounted on a computer controlled rotation stage with a minimal step size of 0.002 degrees. The angular resolving power is 0.1 degrees. A sheet polarizer is placed between the lens and diode to discriminate between s- and p-polarized light. We monitor simultaneously the incident intensity to correct for intensity variations of the light source.

The transmitted intensity curves are plotted in Fig. 12 A to D. The figure labels refer to the sample labels of Table 4.1. The solid lines give the measured transmitted intensity. It is readily seen that the intensity of the p-polarized light is higher than that of the s-polarized light for all samples. Although the incident light is unpolarized, the transmitted light becomes (partly) polarized when it crosses the boundary of the scattering medium. The dashed curves are identical for all plots A-D, and were obtained from diffusion theory, see Chapter 2. Fig. 13 plots the visibility of the polarization of the transmitted light as a function of the outgoing angle. We observe that the smoother the sample surface, the higher the polarization of the transmitted light. Note that even for the sample consisting of

[3] We have measured the diameter of the spot size of the reflected light at a particular distance from the sample.

sample index	material	thickness (μm)	mean-free path (μm)	divergency of reflection
A	TiO_2-particles	10	0.7	1.4 mrad
B	TiO_2-particles	14	0.7	20 mrad
C	Teflon	9300	160	< 90 mrad
D	10 μm latex spheres	1500	2.4	-

Table 4.1: Properties of the samples used in the transmission experiment.

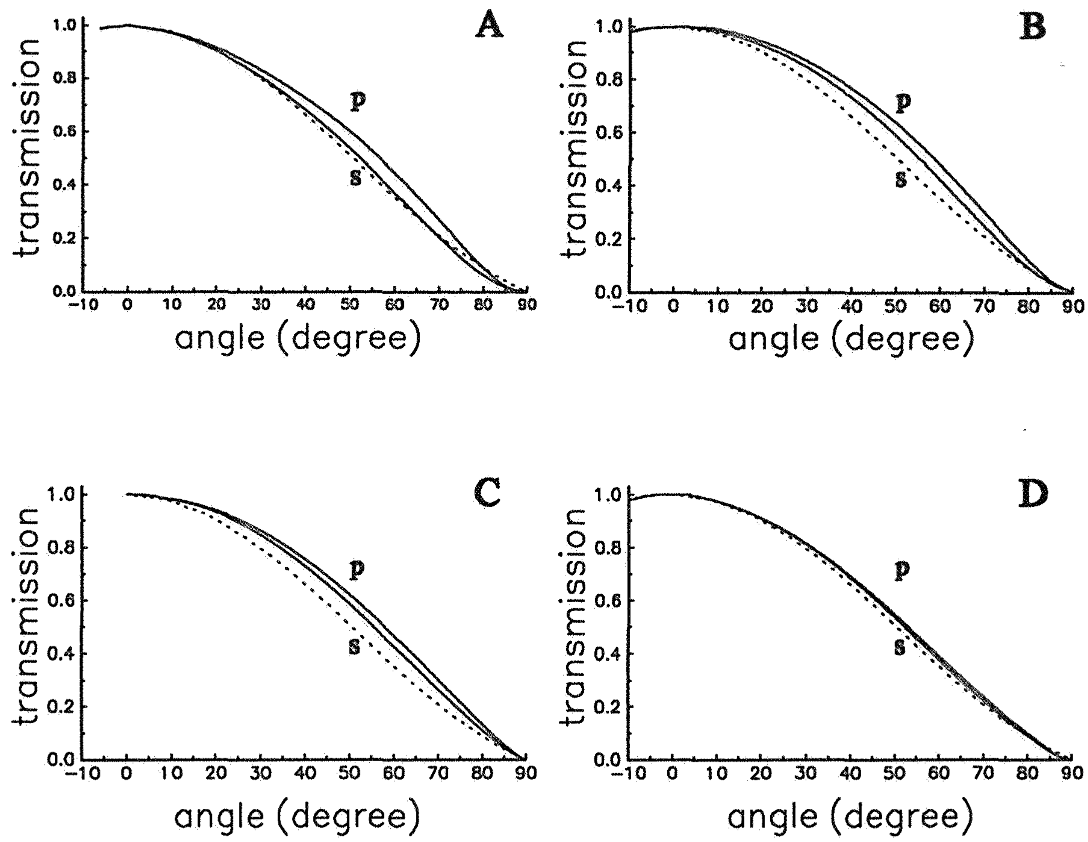

Figure 12: Angular resolved transmission for four multiple scattering samples A,B,C, and D. Properties of the samples are give in Table 4.1. The labels 's' and 'p' refer to s-polarized and p-polarized light, the dashed curves are calculated using diffusion theory, Eq. (2.95) of Chapter 2.

10 μm latex spheres, with consequently a surface roughness of 10 μm steps, the transmitted intensity is slightly polarized for outgoing angles near 90 degrees.

The dotted line in Fig. 13 shows the polarization of the emitted radiation from a semi-infinite medium (smooth interface) containing scatterers with a Rayleigh phase function. It represents a numerical solution of the equation of transfer.[16] Reflections at the interface between scattering and non-scattering medium were not taken into account. The combination of the direction of the light flux propagating to the boundary (directed normally to the surface of the scattering medium) and the Rayleigh phase function of the scatterers, suppresses scattering of p-polarized light towards grazing angles: the transmitted intensity will be s-polarized. Introducing forward scattering for this situation will *reduce* the polarization of the

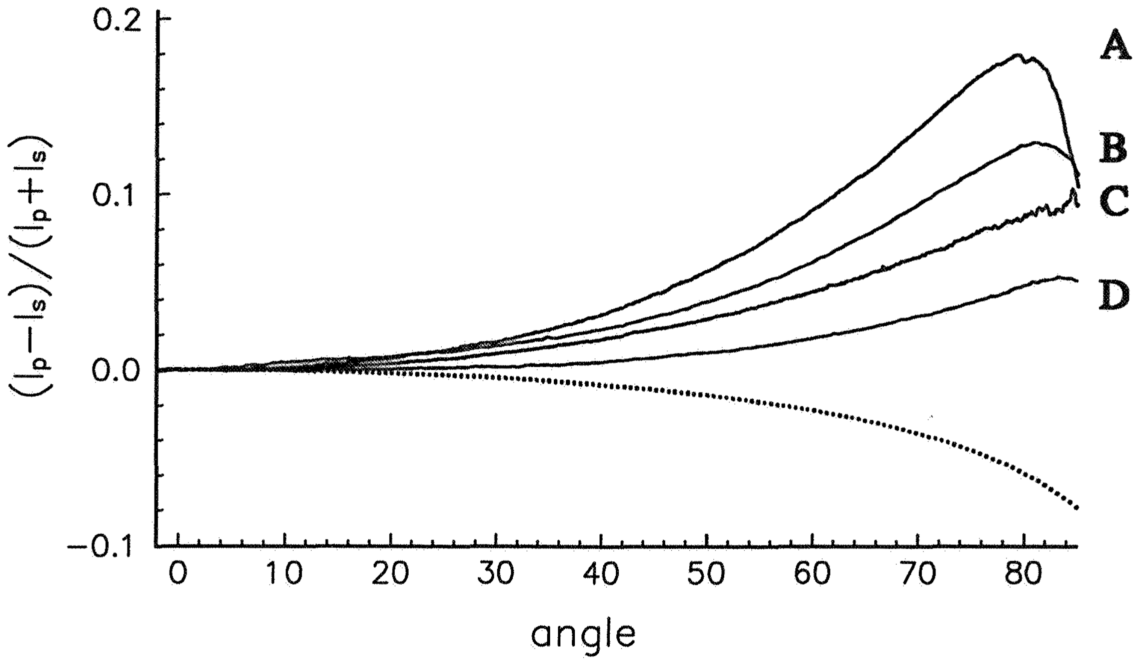

Figure 13: The visibility of the polarization of the transmitted light through the samples A,B,C, and D is plotted as a function of the outgoing angle. The sample properties are listed in Table 4.1. The dotted line is a numerical solution of the equation of transfer for scatterers with a Rayleigh phase function.[16]

emitted light, because the intensity difference between s- and p-polarized scattered light is small for forward scattering particles. However, when the indices of refraction of scattering and non-scattering media differ, the diffuse transmission will be p-polarized because the transmission coefficient of p-polarized light is higher than that of s-polarized light.

Surface roughness diminishes the induced polarization which can be understood as follows: the degree of polarization of the emitted light is determined by the propagation direction of the light with respect to the local surface normal. For a rough surface, the local surface normals make random orientations to the global surface normal, and hence the polarization of the transmitted light is reduced. Additionally, surface roughness will induce extra scattering of the transmitted light which also reduces the polarization of the light.

Our observations are consistent with experiments of Eliyahu *et.al.* [17]. In Ref. [17] the angular resolved transmission was studied as a function of the optical thickness of a scattering aqueous suspension contained by a glass cell. Consequently, the reflections at the sample surface (the suspension-cell interface) were low. Full depolarization of the incident light is observed for optically thick slabs. This means that the transmitted light is not polarized when the refractive index of the sample is matched with that of the non-scattering medium.

Results similar to ours have been obtained recently by Jordan and Lewis.[18] In Ref. [18] the polarization of thermal radiance of *homogeneous* samples is studied as a function of the outgoing angle and surface roughness. A higher degree of polarization is found for smoother sample surfaces.

Multiple scattering in combination with surface roughness can also be studied by measuring speckle correlations of the reflected intensity for samples with the same mean-free path but different surface roughness. In such an experiment one changes the angle of incidence and the angle of detection with the same pace, and measures the correlation of the reflected intensity as a function of the angle. For a multiply scattering sample, the decay rate of the correlation with respect to the change in angle is not only determined by the mean-free path of the sample,[19] but also by the length-scale of the surface roughness. These two length scales are of course not equal. It is to be expected that the two length scales can be determined by measuring correlation functions for different arrangements of light source and detector and orientations of the incident and detected polarization with respect to the sample surface.

4.4.3 Conclusion

On top of single and multiple scattering, the incident light is also 'specular' reflected at the surface of the scattering medium due to the refractive index contrast between the scattering and the non-scattering medium. The roughness of the sample surface determines the divergency of the specularly reflected intensity and thereby the impact on the enhancement factor of the coherently backscattered light. Internal reflection of light leaving the sample induces polarization of the light, which may be scrambled depending on the surface roughness of the sample.

References

[1] A.R. McGurn and A.A. Maradudin, *An analogue of enhanced backscattering in the transmission of light through a thin film with a randomly rough surface*, Opt. Comm. **72**, 279 (1989).

[2] M.B. van de Mark, 'Propagation of light in disordered media: a search for Anderson localization', Ph.D. thesis, Universiteit van Amsterdam, 1990.

[3] B.A. van Tiggelen, 'Multiple scattering and localization of light', Ph.D. thesis, Universiteit van Amsterdam, 1992.

[4] F.M. Ismagilov and Yu.A. Kravtsov, *Enhanced forward scattering on a system of two small randomly oriented scatterers*, Phys. Lett. A **188**, 91 (1994).

[5] M.B. van de Mark, M.P. van Albada, and A. Lagendijk, *Light scattering in strongly scattering media: Multiple scattering and weak localization*, Phys. Rev. B. **37**, 3575 (1988).

[6] M.P. van Albada, M.B. van der Mark, and A. Lagendijk, *Observation of weak localization of light in a finite slab: anisotropy effects and light path qualifications*, Phys. Rev. Let. **58**, 361 (1988).

[7] M.P. van Albada, *Berry's phase in multiple point-dipole scattering*, Proceedings of Progress In Electromagnetics Research Symposium (PIERS 1994), Eds. B. Arbesser-Rastburg, M. Borgeuad, S. Buinomon, J. Belshaw, J. Matagne, J. Noll, (Kluwer acad. pub. 1994) (on cd-rom).

[8] M. Ospeck and S. Fraden, *Influence of reflecting boundaries and finite interfacial thickness on the coherent backscattering cone*, Phys. Rev. E. **49**, 4578 (1994).

[9] D.S. Wiersma, M.P. van Albada, and A. Lagendijk, *Experimental evidence for recurrent light scattering*, Submitted to Phys. Rev. Lett.

[10] P.M. Saulnier and G.H. Watson, *Role of surface reflectivity in coherent backscattering measurements*, Opt. Lett. **17**, 946 (1992).

[11] M.P. van Albada, A. Lagendijk and, M.B. van de Mark, *Towards observation of Anderson localisation of light*, Analogies in Optics and Micro Electronics, Eds. W. Haeringen and D. Lenstra. (Kluwer Acad. Pub. 1990).

[12] M. Saillard and D. Maystre, *Scattering from metallic and dielectric rough surfaces*, J. Opt. Soc. Am. A **7**, 982 (1990).

[13] C. Macaskill, *Geometric optics and enhanced backscattering from very rough surfaces*, J. Opt. Am. Soc. A **8**, 88 (1991).

[14] M. Nieto-Vesperinas and J.A. Sánches-Gil, *Light scattering from a random rough interface with total internal reflection* J. Opt. Soc. Am. A **9**, 424 (1992).

[15] G. Videen, J. Hsu, W.W. Bickel, and W.L. Wolfe, *Polarized light scattered from rough surfaces*, J. Opt. Soc. Am. A **9**, 1111 (1992).

[16] S. Chandrasekhar, 'Radiative Transfer', (Dover, New York, 1960).

[17] D. Eliyahu, M. Rosenbluh, and I. Freund, *Angular intensity and polarization dependence of diffuse transmission through random media*, J. Opt. Soc. A **10**, 1 (1993).

[18] D.L. Jordan and G. Lewis, *Measurements of the effect of surface roughness on the polarization state of thermally emitted radiation*, Opt. Lett. **19**, 692 (1994).

[19] J.F. de Boer, M.P. van Albada, and A. Lagendijk, *Transmission and intensity correlations in wave propagation through random media*, Phys. Rev. B. **45**, 658 (1992).

Chapter 5

Internal reflection

5.1 Introduction

In this chapter we will study the influence of the contrast in index of refraction of a scattering and non-scattering medium on the propagation of light. Two subjects are of major interest: coherent backscattering influenced by internal reflection and the average or effective index of refraction of the scattering medium itself.

Internal reflection occurs when light propagates from the interior of the scattering medium towards the boundary of the medium. The bulk properties of the scattering medium appear to be modified because the light is forced to make extra trajectories in the scattering medium. For instance, the diffusion constant seems to be reduced since the light remains longer in the sample. On the other hand, the blurring of a point source by the disordered medium (in reflection) is enlarged which could be misinterpreted in terms of a larger mean-free path[1]-[7].

The effective index of refraction of the scattering medium is an important parameter, since the contrast in index of refraction of the scattering and the non-scattering medium determines the magnitude of internal reflection. Calculating the effective refractive index of a scattering medium, a composite of two materials with different indices of refraction, is a difficult problem. Only for some specific situations can reliable approximations be found; this is the long-wavelength limit, the situation where the mean-free path is much larger than the wavelength. Known mean-field approximations are: Average T-matrix Approximation (ATA), usually referred to as Maxwell Garnett or Clausius-Mossotti Approximation[8], Coherent Potential Approximation (CPA) or Effective Medium approximation[9]. The outcome of ATA is symmetric in interchanging the two components (keeping the volume fractions constant), whereas the outcome of CPA depends on whether the medium with the lowest or the highest index of refraction is embedded in the other component. If the indices of refraction are almost equal, the expression of

Maxwell Garnet reduces to the simplest effective medium theory:

$$<n>= fn_1 + (1-f)n_2, \tag{5.1}$$

where f is the volume fraction of medium 1 in medium 2, and n_1 and n_2 are the indices of refraction of the corresponding media.

However, the mean-free path for our scattering media is comparable to the wavelength of light and comparable to the size of the scatterers. Thus the mean-field approximations cannot be used to make a useful estimate of the value for the effective index of refraction of our samples.

An experimental method to measure the effective index of refraction could be the determination of the Brewster angle. At the Brewster angle the reflection of p-polarized light is minimal. The location of this angle is directly related to the index of refraction of the sample. As will become clear later, enhanced backscattering can also be used to determine the effective index of refraction.

Measurements in reflection are more sensitive for internal reflection than transmission measurements, because the extra trajectories made by the light should be a substantial increase of the total path length. In reflection, arbitrarily short paths contribute to the reflected intensity, whereas in transmission the average path length is of order L^2/l, L being the typical dimension of the scattering medium and l the mean-free path. A clear manifestation of internal reflection is thus only to be expected for reflection measurements.

Since the total path length is increased by internal reflection, the distance traversed parallel to the interface is increased also, as can be seen from Fig. 1. Consequently, the width of the backscatter cone is decreased because the angular width of the backscatter cone is inversely proportional to this distance. Moreover, the higher the surface reflections, the narrower the backscatter cone. An experiment by Saulnier and Watson[3] confirms this statement. They used a number of 'half-mirrors' of known reflectivity in water to contain their samples. In Ref. [3] the backscattered intensity was measured of suspended latex spheres in water. For higher reflection coefficients of the half-mirrors, a smaller width of the backscatter cone was indeed found.

So far, all experiments have concentrated mostly on varying the reflection properties of the sample walls, i.e. using mirrors to induce reflections[3]-[4]. In this case, the magnitude of the reflections is more or less independent of the sample properties. In contrast, we will vary the index of refraction of the surrounding homogeneous medium. Now, reflection at the boundary depends on the contrast in the index of refraction of the surrounding homogeneous medium and the disordered scattering medium. The experiments will not only yield the behaviour of the backscatter cone for a number of refractive index contrasts, but also values for the effective index of refraction of the scattering media. In comparing the theory

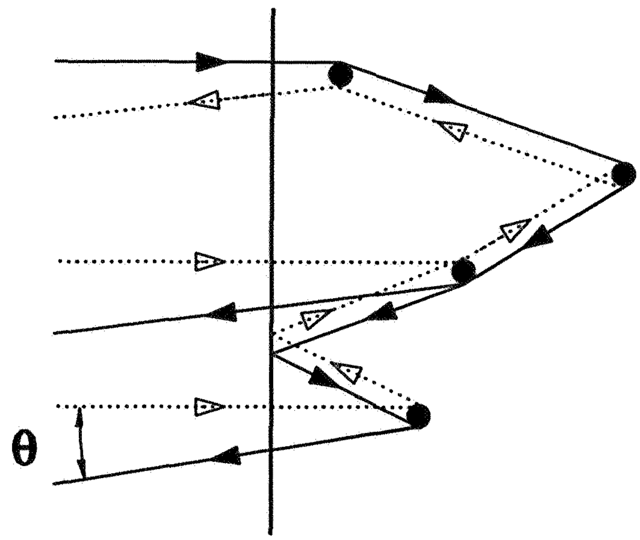

Figure 1: A typical backscatter sequence responsible for coherent backscattering is shown. Reflection at the interface increases the transversal distance between first and last scattering event.

on internal reflection with the experiments, we will use the effective index of refraction of the samples as a fit parameter to obtain the best correspondence. If the theoretical models would be at variance with our data, we can still make an estimate of the effective index of refraction of the samples: knowing that internal reflection reduces the width of the backscatter cone, an optimally matched sample will produce a backscatter cone with a maximal width. In this way we have defined the effective index of refraction as a property of the diffuse intensity, and not as is usual, a property of the coherent beam. However, it is to be expected that when the intensity is not reflected at the interface, meaning an optimal match is achieved, this also holds for the amplitude of the wave.

5.2 Theory

Our approach to calculate the influence of internal reflection on coherent backscattering is a conjunction of two papers[1][2]. The calculations are based on the diffusion approximation, but we will also use results of the underlying transport theory; i.e. the Milne equation. In Ref. [1] surface reflectivity is incorporated at the level of intensity Green's functions, or diffusion propagators. The diffusion propagator $P(\mathbf{r}', \mathbf{r})$ describes the response, intensity, at $\mathbf{r}'$ due to a point source at $\mathbf{r}$. The diffusion propagator is adjusted to take account of surface reflection. An average reflection parameter R is introduced. It describes the reflection of diffusive waves impinging on the boundary from inside the sample. In Ref. [2] a closed expression is derived for this reflection coefficient R in terms of the Fresnel coefficients.

The thickness of the samples in the experiments is much larger than the mean-free path, and absorption of light inside the samples is not important. Therefore, we will consider only a semi-infinite non-absorbent scattering medium. The scattering medium is bounded by the z=0-plane. For $z < 0$ we have vacuum and for $z > 0$ there is scattering. Making use again of the translational invariance in the xy-plane, we write for the intensity

$$I(\mathbf{r}) = \int d\mathbf{q}_\perp \exp(i\mathbf{q}_\perp \cdot \rho)\, I(z, \mathbf{q}_\perp), \qquad \text{with} \quad \rho \equiv (x, y). \tag{5.2}$$

Fourier transformation of the diffusion equation over the transfer vector ρ, yields the differential equation for the one dimensional Green's function with perpendicular momentum transfer $\mathbf{q}_\perp$. The Green's function should fulfil

$$\frac{d^2}{dz^2} P(z', z; \mathbf{q}_\perp) - q_\perp^2 P(z', z; \mathbf{q}_\perp) = -\delta(z - z'). \tag{5.3}$$

The solution for the infinite medium is given by

$$P_0(z', z; \mathbf{q}_\perp) = \frac{1}{2q_\perp} \exp(-q_\perp |z - z'|). \tag{5.4}$$

Reflection at the edge of a scattering medium can be incorporated in the boundary condition for the diffusion propagator as follows[11]

$$P(z', -z_0; \mathbf{q}_\perp) = \frac{R}{1 - R} \left.\frac{\partial P(z', z; \mathbf{q}_\perp)}{\partial z}\right|_{-z_0} \equiv \epsilon \left.\frac{\partial P(z', z; \mathbf{q}_\perp)}{\partial z}\right|_{-z_0}. \tag{5.5}$$

If reflection is absent, $R = 0$, one retains the normal boundary conditions: $I(z = -z_0) = 0$. A finite reflection allows for a finite intensity at the boundary. For $R = 1$, the intensity near the boundary should, to first order, not depend on z; the derivative normal to the xy-plane should be zero to fulfil Eq. (5.5). This shows a new consequence of a (partly) reflecting boundary: the extrapolation length should depend on the reflection parameter R. The extrapolation length should even diverge for totally reflecting boundaries. In that case, the intensity at the boundary is finite, whereas the slope at that point is zero. Thus the virtual crossing of the extrapolated intensity with the z-axis is at minus infinity. This is equivalent to an infinite extrapolation length. We will come back to the reflection dependency of the extrapolation length later.

Without internal reflection, the Green's function for the semi-infinite medium is easily constructed by adding one Green's function (with opposite sign) mirrored in the z=-z_0-plane. This results in zero intensity at the mathematical boundary, as required. To construct the Green's function for a semi-infinite medium with a partly reflecting boundary we proceed similarly and try

$$P(z', z; \mathbf{q}_\perp) = P_0(z', z; \mathbf{q}_\perp) + AP_0(z', -(z + 2z_0); \mathbf{q}_\perp) \tag{5.6}$$

Using Eq. (5.5) we find the coefficient A

$$A = \frac{\epsilon l_{tr} q_\perp - 1}{\epsilon l_{tr} q_\perp + 1}. \tag{5.7}$$

Thus we have found the diffusion propagator for a semi-infinite medium with a partly reflecting boundary. However, we have not said much about the magnitude of this reflection parameter R and its dependence on the contrast in the indices of refraction of scattering and non-scattering media. Boundary condition (5.5) applies to a one dimensional random walk, the same holds for the reflection coefficient R. It is not trivial to choose the right procedure to calculate from first principles a value for R applicable in three dimensions. It cannot be a simple average of the Fresnel coefficients over all incoming angles. To obtain an expression for R valid in three dimensions, we adapt the approach of Ref. [2]. We will first review the derivation of the reflection dependency of the extrapolating length z_0 and after that, obtain an expression for the reflection parameter R in terms of the Fresnel reflection coefficients.

In a slab or semi-infinite scattering medium with a plane wave source, we have translational invariance in the xy-plane. The z-axis is perpendicular to the boundaries of the scattering system. We assume an almost isotropic intensity distribution such that the flux density $\mathbf{J}(\mathbf{r}, \hat{\mathbf{s}})$ is much smaller than the local intensity $I(\mathbf{r})$.[10] In this case, the specific intensity $I(\mathbf{r}, \hat{\mathbf{s}})$ can be approximated by

$$I(\mathbf{r}, \hat{\mathbf{s}}) = I(z, \mu) \approx I(z) + \frac{3}{v}\mu J_z(z), \tag{5.8}$$

with v being the energy transport velocity, $\mu \equiv \cos\theta$, θ the angle between the direction of propagation $\hat{\mathbf{s}}$ and the z-axis. We thus have

$$J_z(z) = \frac{v}{4\pi}\int I(z, \mu)\mu d\Omega, \tag{5.9}$$

which gives for the flux density per solid angle $d\Omega$,

$$\frac{dJ_z}{d\Omega} = \frac{v}{4\pi}\mu I(z, \mu) = \frac{1}{4\pi}\{\mu v I(z) + 3\mu^2 J_z(z)\}. \tag{5.10}$$

The total flux at depth $z = 0$ in positive z-direction, (flowing inwards), is

$$J_z^+(0) \equiv \int_0^1 d\mu \int_0^{2\pi} d\phi \frac{dJ_z}{d\Omega} = \frac{v}{4}I(0) + \frac{1}{2}J_z(0) = \frac{v}{4}I(0) - \frac{v l_{tr}}{6}\left.\frac{dI(z)}{dz}\right|_0. \tag{5.11}$$

Unless there is reflection, $J_z^+(0)$ will be zero

$$J_z^+(0) = 0 \Longrightarrow I(0) = \frac{2}{3} l_{tr} \left. \frac{dI(z)}{dz} \right|_0 . \tag{5.12}$$

A straight line through $I(0)$ fulfilling Eq. (5.12) will cross the ($I=0$)-axis at $-\frac{2}{3}l_{tr}$. Hence, Eq. (5.12) is equivalent to an extrapolating length $z_0 = \frac{2}{3}l_{tr}$. This is the diffusion result for zero surface reflectivity, and is quite close to the Milne result: $z_0 = 0.7104l$.

If $J_z^+(0)$ is non-zero, this must result from reflection of the flux propagating in negative z-direction $J_z^-(0)$. The last is defined as

$$J_z^-(0) \equiv \int_{-1}^{0} d\mu \int_0^{2\pi} d\phi \frac{dJ_z(0)}{d\Omega} = \frac{v}{4} I(0) + \frac{v l_{tr}}{6} I'(0). \tag{5.13}$$

So we write for the total flux in positive z-direction

$$J_z^+(0) = -R J_z^-(0), \tag{5.14}$$

and find, using Eq. (5.11) and Eq. (5.13),

$$I(0) = \frac{2}{3} l_{tr} \frac{1+R}{1-R} I'(0) \Longrightarrow z_0(R) = \frac{2}{3}\frac{1+R}{1-R} l_{tr}. \tag{5.15}$$

Indeed an infinite extrapolating length is found for totally reflecting boundaries.

We would like to have a value for the reflection parameter R that can be calculated using the Fresnel coefficients $r_{\parallel}(\mu)$ and $r_{\perp}(\mu)$. The reflection coefficients are given by

$$r_{\parallel}(\mu) = \left| \frac{m\mu - \sqrt{1 - \frac{1}{m^2}(1-\mu^2)}}{m\mu + \sqrt{1 - \frac{1}{m^2}(1-\mu^2)}} \right|^2 . \tag{5.16}$$

for p-polarized light (polarization vector in the plane of reflection) and

$$r_{\perp}(\mu) = \left| \frac{\mu - \sqrt{m^2 - (1-\mu^2)}}{\mu + \sqrt{m^2 - (1-\mu^2)}} \right|^2 . \tag{5.17}$$

for s-polarized light (polarization perpendicular to the plane of reflection).[12] The equations hold for light propagating in a medium with an index of refraction n_1 reflected from a medium with an index of refraction n_2, $m \equiv n_1/n_2$. A reflection parameter R averaged over polarization as a function of angle can be simply constructed as

$$R(\mu) = \frac{1}{2}\left(r_{\perp}(\mu) + r_{\parallel}(\mu) \right). \tag{5.18}$$

To obtain an angle-averaged reflection parameter R, we return to Eq. (5.14). The right hand side of Eq. (5.14) now becomes

$$-\int_{-1}^{0} d\mu R(\mu) J_z^-(0) = -\frac{1}{2} v I(0) C_1 - \frac{1}{2} v l_{tr} I'(0) C_2. \tag{5.19}$$

with

$$\begin{aligned} C_1 &= \frac{1}{2}\int \left(r_\perp(\mu) + r_\parallel(\mu)\right) \mu d\mu \\ C_2 &= \frac{1}{2}\int \left(r_\perp(\mu) + r_\parallel(\mu)\right) \mu^2 d\mu \end{aligned} \tag{5.20}$$

From which follows

$$I(0) = \frac{2}{3} l_{tr} \frac{1+3C_2}{1-2C_1} I'(0) \Longrightarrow z_0 = \frac{2}{3} l_{tr} \frac{1+3C_2}{1-2C_1}. \tag{5.21}$$

The reflection parameter R is derived by comparing Eq. (5.21) with Eq. (5.15)

$$R = \frac{2C_1 + 3C_2 + 1}{3C_2 - 2C_1 + 2}. \tag{5.22}$$

We can now derive an expression for the backscatter cone for non-zero surface reflection using the found Green's function for non-zero surface reflection. We find for the coherently backscattered intensity $I(\theta)$, c.f. Chapter 2

$$\begin{aligned} I(\theta) &\propto \frac{1}{(\alpha+\nu)^2 + u^2} \times \\ &\left(\frac{1}{\nu} + \frac{1}{\alpha}(1 - \exp[-2\alpha z_0(R)/l_{tr}]) + \frac{2}{\epsilon^{-1}+\alpha} \exp[-2\alpha z_0(R)/l_{tr}]\right), \end{aligned} \tag{5.23}$$

with

$$\alpha \equiv k l_{tr}\, |\sin\theta|, \quad \nu \equiv \frac{1}{2}(1 + \frac{1}{\cos\theta}), \quad u \equiv k l_{tr}(1-\cos\theta).$$

In Fig. 2, we plot the calculated backscattered intensity for various reflection coefficients R, using Eq. (5.23). We plot also backscatter cones for $R = 0$ but with scaled mean-free paths l_0. For each curve the mean-free path is scaled (increased) to match the width of the backscatter cone for $R \neq 0$. Comparing those curves, one verifies that the major effect of internal reflection is a decrease of the width. The shapes differ only for high values of R.

Calculating the width of the backscatter cone as a function of the reflection parameter R reveals a surprisingly simple behaviour: the width is just a linear function of R, shown in the inset of Fig. 2.

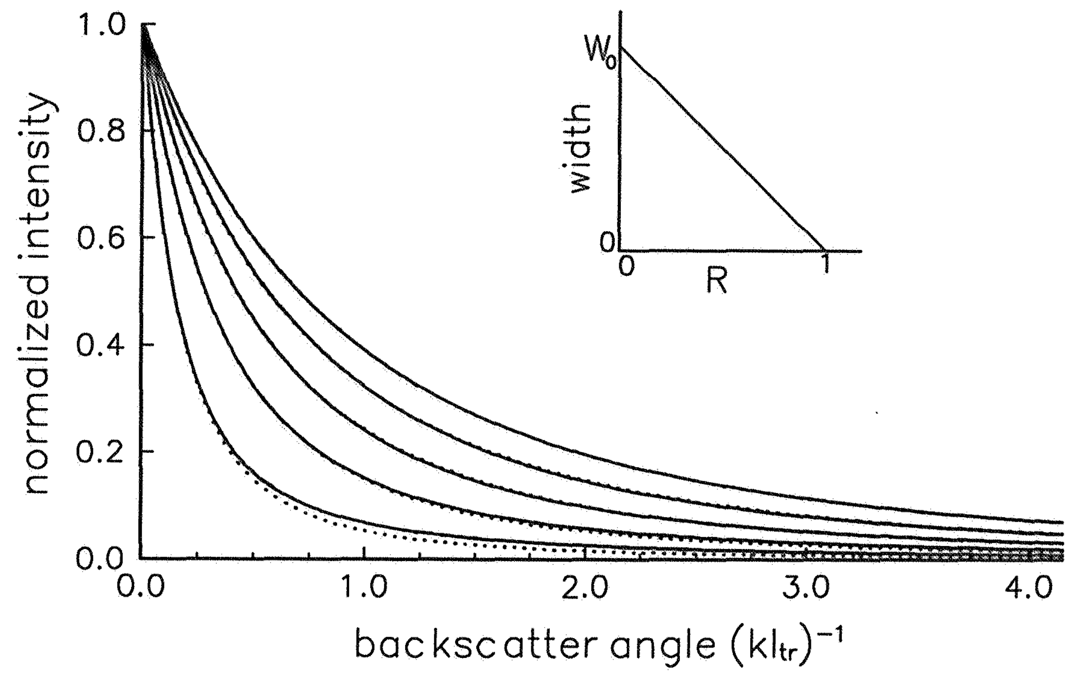

Figure 2: Calculated line shapes using Eq. (5.23) for the backscatter cone with various reflection coefficients R, solid lines. From upper to lower curve: R=0, 0.2, 0.4, 0.6, 0.8. Dotted lines show calculated backscatter cones for $R = 0$ with scaled mean-free path l_0. From upper to lower curve: $l_0 = l, 1\frac{1}{4}l, 1\frac{2}{3}l, 2\frac{1}{2}l, 5l$ respectively. Inset: width of the backscatter cones as a function of the reflection parameter R. W_0 refers to the width of the cone for $R = 0$.

5.3 Experimental procedures

We will now discuss the experimental procedures for backscatter measurements. The idea of the experiment is to compare backscatter cones measured from the same sample for a number of different refractive index contrasts. Glass types with different indices of refraction are used as windows on top of the sample to produce the different contrasts.

The width of the backscatter cone is not influenced by refraction at the glass interfaces; there is an exact compensation. This is easily shown by calculating the refraction of a light ray leaving the sample with an initial direction that makes an angle θ_s to the surface normal of the glass. Let θ_g be the direction inside the glass and θ_a the direction in air, we find with Snell's Law

$$\sin\theta_a = \frac{n_g}{n_a}\sin\theta_g = \frac{n_g}{n_a}\frac{n_s}{n_g}\sin\theta_s = \frac{n_s}{n_a}\sin\theta_s, \tag{5.24}$$

where n_s, n_g, and n_a are the indices of refraction of the sample, glass and air, respectively.

We use 5 different glass types: Fused Quartz n=1.46, BK7 n=1.52, F1 n=1.63, LaSF1 n=1.80, and ZnSe n=2.6, indices of refraction hold for 600 nm light. In addition, we aslo measure on a sample-air interface.

5.3.1 Sample preparation

After trying several fluids, the best results were obtained with suspension of TiO_2-particles in methylpentanediol (n=1.43) and in benzylalcohol (n=1.54). Methylpentanediol hardly evaporates and benzylalcohol is not very volatile. The volume fractions of TiO_2 in methylpentanediol and benzylalcohol were around 0.33 and 0.35, respectively. Clusters of TiO_2-particles in the suspensions were disintegrated ultrasonically and by shaking the suspensions with glass beads. Encountered problems with the samples were: spots of higher density of TiO_2-particles adhering to the window and evaporation of the solvent during preparation and during measurements. Especially fluids like water and methanol exhibit these problems, and were therefore not used. The samples are rotated in a vertical plane to prevent sedimentation of the TiO_2-particles during the measurement.

The reason to use suspensions instead of dried out samples is that a fluid always makes a good optical contact with the glass. Optical contact exists when, for instance, two pieces of glass of the same refractive index do not produce a reflection when they are pressed on each other. The reflection disappears when the distance between the two glass pieces is much smaller than the wavelength. Dried out samples often crack, and not every part of the sample remains in optical contact with the glass. The latter shows up as a non-uniform radiance of the sample surface if observed through the glass. The parts of the sample surface that have lost optical contact exhibit a higher radiance. An explanation for this higher radiance is given in the beginning of section 5.4 and in Fig. 5.

Another disadvantage of dried samples is the possibility of sedimentation of TiO_2-particles during the evaporation of the fluid. It results in slight variations in the mean-free path inside the samples and variations from sample to sample.

We made sandwiches of the scattering suspensions in between two glass windows. The thickness of the windows, 10 mm, is large enough to prevent the totally internal reflected light at the glass-air interface from reentering the sample, cf. Chapter 7. The suspensions are contained by a flat 'O-ring' of 250 μm thick, which also separates the windows. The sides were sealed with 'parafilm' that holds the two windows together and prevents evaporation of the fluid. A sketch is drawn in Fig. 3.

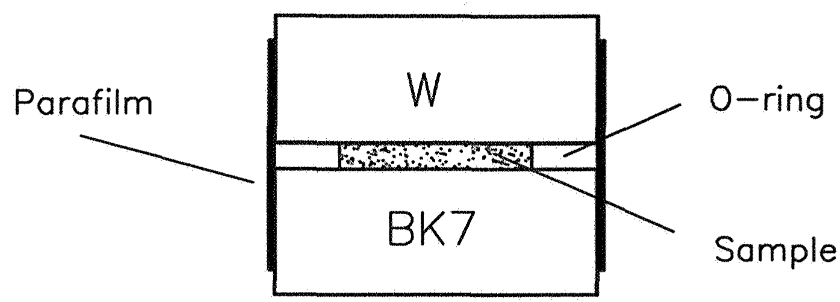

Figure 3: A suspension of TiO_2-particles is sandwiched between two different windows. The backscatter cone can be recorded from either side. The windows are denoted by 'W', and 'BK7'.

5.3.2 Determination of the width

To determine accurately the width of the backscatter cones, we perform numerical fits of the following equation to the measurements

$$I(\theta) = I_d(\theta) + I_c(\theta), \tag{5.25}$$

with $I_d(\theta)$ the incoherent or diffuse background given by

$$I_d(\theta) = \cos\theta \left\{ 1 + z_0/l_0 - \frac{1}{1+\cos\theta} \right\}, \tag{5.26}$$

and $I_c(\theta)$ the coherently backscattered light

$$I_c(\theta) = \frac{B-1}{(\alpha+\nu)^2 + u^2} \left\{ \frac{1}{\nu} + \frac{1}{\alpha}(1 - \exp[-2\alpha z_0/l_0]) \right\}. \tag{5.27}$$

With

$$\alpha \equiv k l_0\, |\sin\theta|, \quad \nu \equiv \frac{1}{2}(1 + \frac{1}{\cos\theta}), \quad u \equiv k l_0(1-\cos\theta).$$

The derivation of these equations, and their intrinsic approximations are reviewed in Chapter 2. It is important to note that these equations are derived for zero surface reflectivity. The expression for the coherently backscattered light is the same as in Eq. 5.23 for $R = 0$, and $z_0 = 0.7104 l_0$. Using these equations to describe our measurements, l_0 should not be seen as the transport mean-free path but as a width determining fit parameter. Knowing a theoretical lineshape, the whole measured curve can be used to determine the width. The enhancement factor B varies typically between 1.8 and 1.9 for TiO_2-samples.

In Fig. 4 we plot an example of measured backscattered light for both sides of the benzylalcohol-suspension sandwiched between the LaSF1-window and the

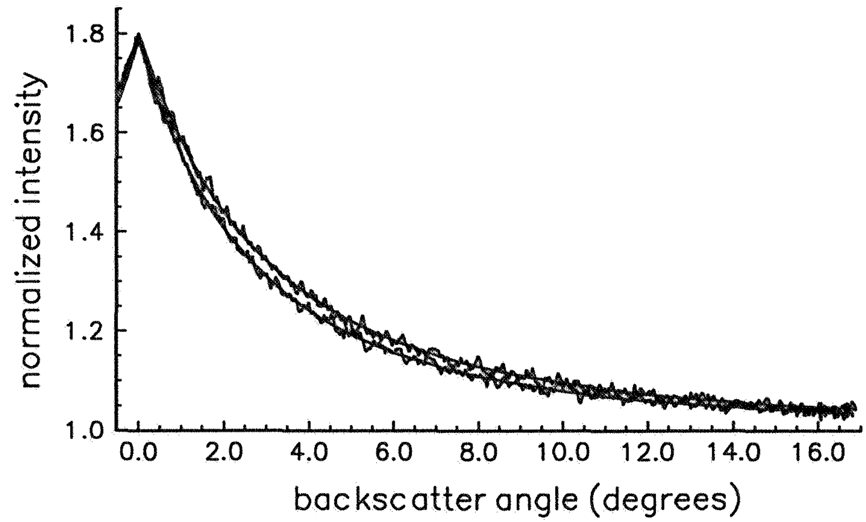

Figure 4: Detail of the measured backscatter cones, for TiO_2 in benzylalcohol. Upper curve: BK7-window, Lower curve: LaSF1-window. Smooth curves are obtained from Eq. (5.25) using $l_0 = 0.760 \pm 0.006$ μm, enhancement factor: 1.80 ± 0.01 upper curve, and $l_0 = 0.852 \pm 0.006$ μm, enhancement factor: 1.79 ± 0.01, lower curve. The intensity of the diffusive background is normalized to 1.

BK7-window. The intensity at the top, the enhancement factor and the 'mean-free path' are adjusted to obtain the best correspondence with Eq. (5.25) to the measured curves.

5.4 Results

5.4.1 Internal reflection measurements

The experimental apparatus that measures the scattered intensity as a function of the backscatter angle is discussed in detail in Chapter 3.

A remarkable observation is a dramatic decrease of the reflected intensity when a scattering sample is in optical contact with a glass window. An example is shown in Fig. 5. The measured backscattered intensity from a teflon sample is plotted for two situations, the upper curve is for a teflon sample in air, the lower curve is for the same sample behind BK7-glass. An index-matching fluid was used to make an optical contact between the sample and the glass. Of course, the total reflected intensity cannot change. If the thickness of the scattering system is much larger than the mean-free path all light is reflected. The cause of the decreased

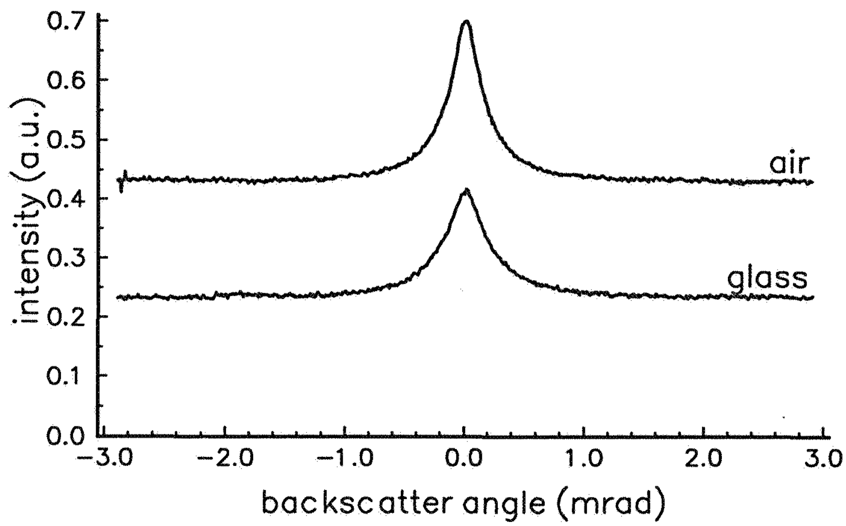

Figure 5: Backscattered intensity from teflon. Upper curve: teflon in air. Lower curve: teflon behind a BK7-window with index matching fluid. The decrease in intensity is real, and caused by trapping inside the window.

intensity is trapping of light inside the window. Without a window on top of the sample, the contrast in indices of refraction between sample and air defines a critical solid angle in the sample. Light inside this solid angle is capable of escaping the sample, and is refracted over the whole hemisphere. Light outside this solid angle is totally reflected by the interface and reenters the sample. Eventually it will leave the sample within this solid angle after more scattering has occurred. A window on top of the sample changes the situation. The solid angle, wherein the light can escape the sample, is enlarged and thus more light enters the glass. However, this extra light cannot cross the window-air interface, the angle is beyond the total internal reflection angle. It leaks out through the sides of the glass and the backscattered intensity is reduced.

In Fig. 6 and Fig. 7 we plot the measured values for the widths of the backscatter cone as a function of the refractive index of the windows. A strong dependence on the index contrast is observed for the width of the backscatter cone.

To minimize the experimental errors introduced by temporal changes of the suspensions we always had the same BK7-window to one side of the sandwich. All measured changes in the width of the backscatter cone are related to the width measured through this BK7-window. In the case of an air-sample interface, two angular scans are compared, one with and one without the BK7-window on top of the sample. For each other data point, six scans were made, alternating the BK7-window side with one of the glass sides of interest. Small variations in the

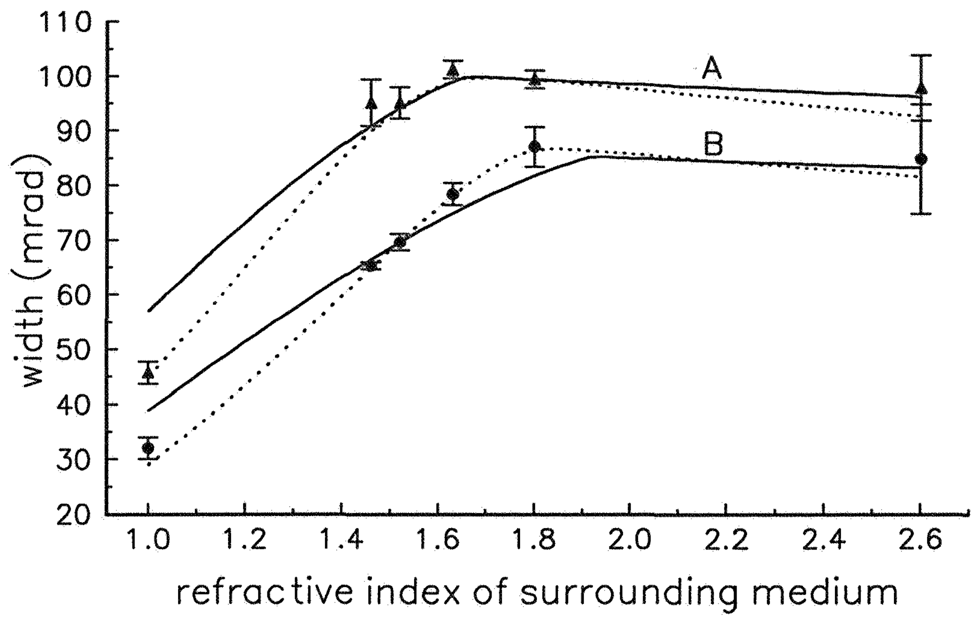

Figure 6: Width of the backscatter cone for different contrast in the refractive-index. Spheres: benzylalcohol-sample, triangles: methylpentanediol-sample. Dotted lines: Eq. (5.23), curve A: $n = 1.665 - 0.09i$, and curve B: $n = 1.82 - 0.05i$. Solid lines: Eq. (5.23) with the reflection dependence of the extrapolation length neglected, using for A: $n = 1.66$, curve B: $n = 1.92$.

width of the backscatter cone measured through the BK7-window are scaled out to follow the behaviour of the width over the whole refractive index range.

The ZnSe-window was only 3 mm thick resulting in a deformed backscatter cone; a small peak on top of the backscatter cone. To mimic a thick window of ZnSe, a double window was constructed by putting an F1-window on top of the ZnSe-window. Reflections, at the interface between the two windows, were reduced with diiodomethane (index of refraction 1.8). This construction improved the measurement considerably, but it did not solve the problem completely. The backscatter cone measured through the double window was still a little deformed.

We will now compare our measurements with theoretical models that take into account the dependence of the width of the backscatter cone on the refractive index mismatch. The values of the index of refraction of the samples are varied in the theoretical models to obtain the best correspondence with the measurements. Weighted least square fits are performed. We fix the theoretical curves at the width for the backscatter cone measured through the BK7-window, because all measurements are related to this width.

In Fig. 6 we plot the calculations performed in section 5.2. There is good agreement with the measurements. Note that we have taken a complex index of refraction for the samples to calculate the reflection coefficient R. A complex index of refraction accounts for extinction of light, which for our sample is entirely due to scattering. To show that the reflection dependency of the extrapolation length cannot be neglected, we also plot in the same figure the model without taking this reflection dependency into account. In that case, we cannot obtain an agreement with the measurements.

In Fig. 7 we plot two other models dealing with internal reflection. In Ref. [2] calculations are performed with a constant injection depth for the diffuse light source, contrary to our calculations where we integrate over the incoming beam. In Ref. [7] besides the refractive index mismatch between sample and surrounding medium, also the effect of the skin layer (where the coherent beam turns into a diffuse wave) was taken into account. The Milne equation was solved numerically for arbitrary index mismatch and analytically in the regime of large index mismatch. Although, the theoretical results of Ref. [7] we use were obtained for the scalar-wave equation and in the limit of large index mismatch, they appear to describe our measurements surprisingly well for the whole refractive-index range.

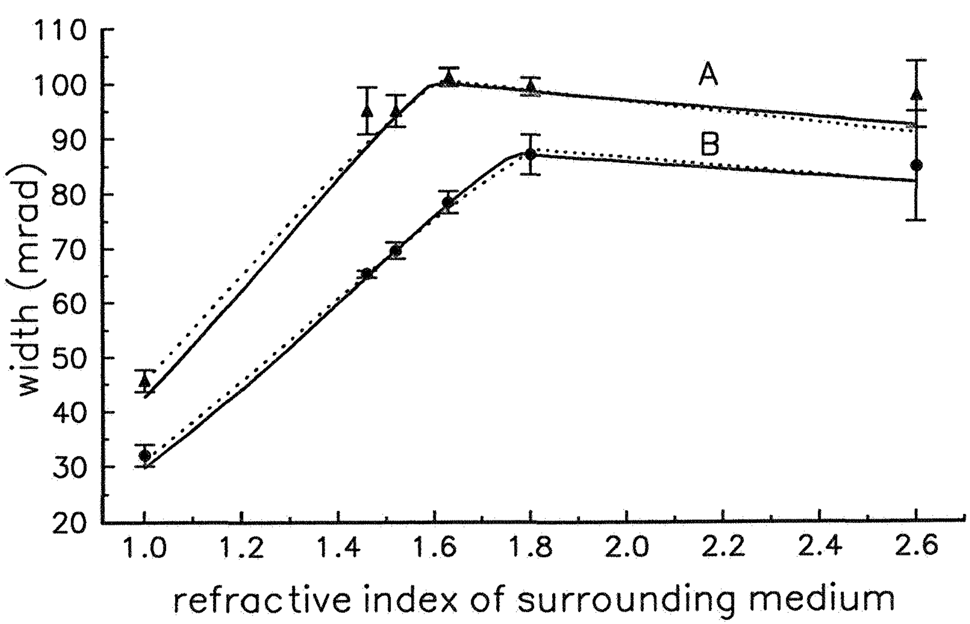

Figure 7: Width of backscatter cone for different contrasts in the refractive index. Spheres: benzylalcohol-sample, squares: methylpentanediol-sample. Dotted lines: model of Ref. [2], curve A: $n = 1.60$, curve B: $n = 1.771$. Dashed lines: skin layer model of Ref. [7], curve A: $n = 1.61$, curve B: $n = 1.81$.

5.4.2 Average index of refraction

The results of the backscatter measurements can be used to extract the effective indices of refraction of the samples. We infer the effective index of refraction from the best numerical fit of theoretical models to our backscatter measurements. In Table 5.1 we compare the indices of refraction acquired from our measurements with calculated values using basic models for the effective index of refraction of heterogeneous media.

The results of a geometrical average and a mean-field theory usually referred to as Maxwell-Garnett[8] are shown, together with a 'Mie-type' of calculation. In this 'Mie-type' of calculation the effective k-vector for a given density of spherical particles is calculated using Mie-theory in the independent scattering-approximation. The effective k-vector is averaged over the size distribution of the particles yielding a value for the effective index of refraction (in Table 1 this result is denoted as Mie-theory). We find an experimental estimate for the imaginary parts of the effective index of refraction using the mean-free path of the samples 0.066(3), and 0.077(2) for benzylalcohol and methylpentanediol respectively.[1]

We see that the mean-field models give higher values than found in the experiment. Only the calculations based on Mie-theory give an effective index of refraction comparable with our measurements. Our results suggest that, in accordance with Mie-theory, the effective index of refraction of a strongly scattering medium can be very low, even close to that of the embedding medium.

[1] We have used the maximal measured width of the backscatter cone to determine the mean-free path of the samples.

		EXPERIMENT			*THEORY*		
		Green's function	fluxes	skin layer	Mie-theory	Maxwell Garnett	Geom. average
A	real	1.59(1)	1.61(1)	1.61(1)		1.79	1.87
	complex	1.66(1)-0.09(1)i	1.64(1)-0.03(1)i		1.67-0.08i		
B	real	1.73(1)	1.77(1)	1.81(1)		1.86	1.92
	complex	1.82(5)-0.05(2)i	1.85(5)-0.03(2)i		1.78-0.13i		

Table 5.1: Values for the effective index of refraction derived from the backscatter experiments using three models on internal reflection compared with basic theories on heterogeneous media. A: methylpentanediol-sample, B: benzylalcohol-sample. Numbers between brackets denote the error in the last decimal.

5.5 Brewster angle measurements

In this section, we compare our results of the previous section (section 5.4.2) with a different experiment where we determine the effective index of refraction as a function of the density of titaniumdioxide via a measurement of the Brewster angle of the samples. As can be checked easily if the index of refraction of the sample is real, there exists an angle θ_b where the specular reflection of p-polarized light is zero (use Eq. (5.16)). This angle is called the Brewster angle and is directly related to the index of refraction of the sample

$$\theta_b = \arctan(n_2/n_1). \tag{5.28}$$

The phenomenon of a Brewster angle can be understood as follows: specular reflection can be regarded to be constructed from radiation of coherently excited dipoles along the refracted beam. At the Brewster angle, the refracted beam is at right angle with the reflected beam. For p-polarized light, the orientation of the dipoles is thus exactly in the direction of the reflected beam. Since light is a transverse wave, the intensity of the reflected beam will be zero.

Besides measurements with light in the visible range ($\lambda = 633$ nm), we measure also with infrared light ($\lambda = 1096$ nm) in order to reduce the sensitivity for density fluctuations at the surface of the samples.[13] Using the Brewster angle to determine the index of refraction, the probe-depth into the sample is only on the order of the wavelength.

We made samples of pressed TiO_2-particles (ø240 ± 70 nm). One part of the press was polished to obtain samples with an optically flat surface: the specular reflection of the sample is clearly visible, and has a divergence of a few mrad. The TiO_2 volume fraction of the samples is obtained by determining the weight and volume of each sample. The thickness of the samples was determined with a calibrated microscope, and most of the samples have a thickness of around 2 mm. The area of the irregularly shaped samples is measured with the help of a photocopy of the sample onto ruled paper. The transport mean-free path is of order 1 μm for visible wavelengths and about a factor of 7 larger for 1096 nm.

The samples are centered on a rotation table. The angle of incidence is calibrated by reflecting the light back towards the laser. The spot size of the laser beam on the samples is approximately 3 mm. A photodiode is used to measure the intensity of the specularly reflected beam. The intensity adjacent to the specular reflection is measured also and subtracted from the intensity of the reflected beam. This corrects for the diffuse background. Near the Brewster minimum the intensity is measured at every degree. The minimum of a parabolic fit through these points is taken as the Brewster angle.

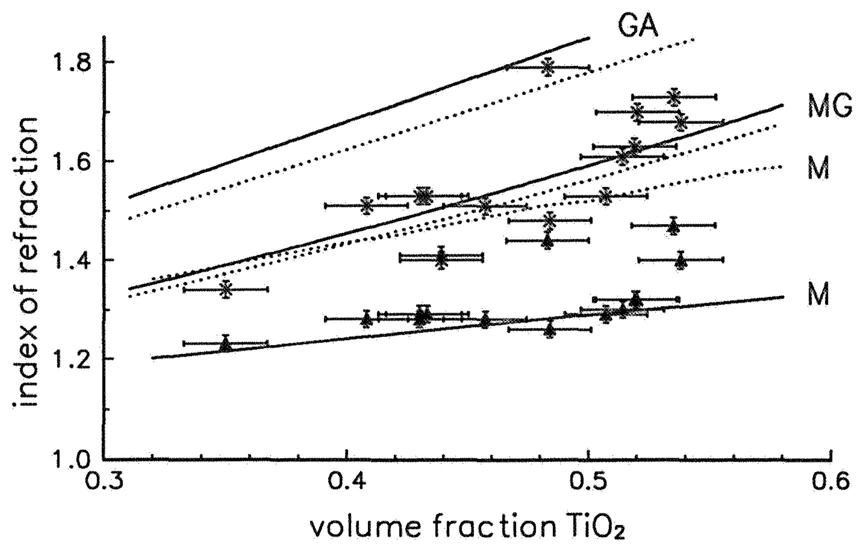

Figure 8: Values for the effective index of refraction of TiO_2-samples obtained from Brewster angle measurements as a function of the volume fraction. Theoretical approximations are shown as solid and dotted lines. Triangles and solid lines: λ = 633 nm, crosses and dotted lines: λ = 1096 nm, labels; GA: geometrical average, MG: Maxwell Garnett, M: 'Mie theory'.

In Fig. 8 we plot the effective indices obtained from the measured Brewster angle as a function of the volume fraction of TiO_2. As can be seen from the plotted results, the spread in the data points is large for both wavelengths. This is probably due to the intrinsic problem of this optical method to determine the index of refraction that probes only a wavelength into the sample. Additionally, the small dimensions of the pressed samples introduce a large experimental uncertainty in the determined density of titaniumdioxide in the samples.

This large spread of the data points makes it hard to draw conclusions concerning the effective index of refraction as a function of the volume fraction of TiO_2. Nevertheless, we find on average a lower value for the effective index of refraction for 633 nm than for a wavelength of 1096 nm. Contrary to this observation, effective medium theories predict a higher effective index of refraction, since titaniumdioxide has a slightly higher index of refraction at 633 nm. However, much more important for the index of refraction is that experimentally the scattering by the TiO_2-particles is more effective at visible than at infra red wavelength. The model, which uses Mie-theory to calculate the effective index of refraction, takes account of this fact, and indeed, a lower index of refraction is calculated for 633 nm wavelength than for 1096 nm.

Note that the agreement between Mie-calculations and the experiments as indicated by Fig. 8 is slightly fortuitous. Because the TiO_2-particles have a large spread in size, the uncertainty in the calculated index of refraction is around 10 % for the calculations with 633 nm light. For large wavelengths or smaller contrasts as in case of the samples used for the backscatter measurement, the uncertainty is smaller, around 3 %.

In conclusion, the effective index of refraction of a strongly scattering medium is indeed much lower than the geometrical average value, which is also indicated by the results of the previous section. To calculate the effective index of refraction of a multiply scattering medium, a scattering approach seems to be the most appropriate.

References

[1] A. Lagendijk, R. Vreeker, and P. de Vries, *Influence of internal reflection on diffusive transport in strongly scattering media*, Phys. Lett. A **136**, 81 (1989).

[2] J.X. Zhu, D.J. Pine, and D.A. Weitz, *Internal reflection of diffuse light in random media*, Phys. Rev. A **44**, 3948 (1991).

[3] P.M. Saulnier and G.H. Watson, *Role of surface reflectivity in coherent backscattering measurements*, Opt. Lett. **17**, 946 (1992).

[4] N. Garcia, A.Z. Genack, and A.A. Lysyansky, *Measurement of the transport mean free path of diffusing photons*, Phys. Rev. B **46**, 14475 (1992).

[5] I. Freund, *Surface reflections and boundary conditions for diffusive photon transport*, Phys. Rev. A **45**, 8854 (1992).

[6] M. Keijzer, W.M. Star, and P.R.M. Storchi, *Optical diffusion in layered media*, Appl. Opt. **27**, 1820 (1988).

[7] Th.M. Nieuwenhuizen and J.M. Luck, *Skin layer of diffusive media*, Phys. Rev. E **48**, 569 (1993).

[8] J.C. Maxwell Garnett, Philos. Trans. R. Soc. London **203**, 385 (1904). See also, C.F. Bohren and D.R. Huffman, 'Absorption and scattering of light by small particles', (Wiley, New York, 1983).

[9] D.A.G. Bruggeman, Ann. Phys. (Leipzig) **24**, 636 (1935) See also, C.F. Bohren and D.R. Huffman, 'Absorption and scattering of light by small particles', (Wiley, New York, 1983).

[10] A. Ishimaru, 'Wave propagation and scattering in random media ', Vol. I, (Academic press, New York, 1978).

[11] N.G. van Kampen, 'Stochastic processes in physics and chemistry', (North-Holland, Amsterdam, 1981).

[12] J.D. Jackson, 'Classical electrodynamics', (Wiley, New York, 1975).

[13] P.A. Molenaar, 'Optical time-resolved transmission experiments on strongly scattering media', M.Sc. thesis, universiteit van Amsterdam, 1990.

Chapter 6

Anisotropic scattering

6.1 Introduction

Anisotropic scattering of light means that the intensity of the scattered light is not equal in all directions. The direction of the scattered light is thus correlated with the direction of the light that was incident on the scatterer. The measure of anisotropy, $<\cos\vartheta>$, expresses the average of the component of the scattered light propagating in the forward direction ($\vartheta = 0$). For metallic spheres, small compared to the wavelength, $<\cos\vartheta>$ is smaller than 0, meaning that most of the light is scattered backwards. Dielectric particles usually scatter in the forward direction, $<\cos\vartheta> \geq 0$. For short wavelengths or large particles $<\cos\vartheta>$ approaches 1 as illustrated in Fig. 1. In Fig. 1 we have plotted the value of $<\cos\vartheta>$ for polystyrene spheres in water as a function of the radius of the sphere.

In a multiply scattering environment, anisotropic scattering can be accounted for by the replacement of the extinction mean-free path l_{ex} by the transport mean-free path. The transport mean-free path is the distance the light should traverse to obtain full decorrelation with an initial direction and to obtain effectively isotropic scattering. The transport mean-free path l_{tr} is related to the extinction mean-free path by

$$l_{tr} = l_{ex}/(1 - a <\cos\vartheta>), \tag{6.1}$$

with a being the albedo of the scatterer, see for more details and references Chapter 2. In this way a random system of anisotropic scatterers is described by isotropic scatterers at a somewhat lower density. Anisotropic scattering thus increases the length scale on which diffusion takes place.

Notice however that l_{tr} is an *average* property of the medium, namely an average over many scattering events. Whenever low order of scattering processes dominate, this approximation may break down.

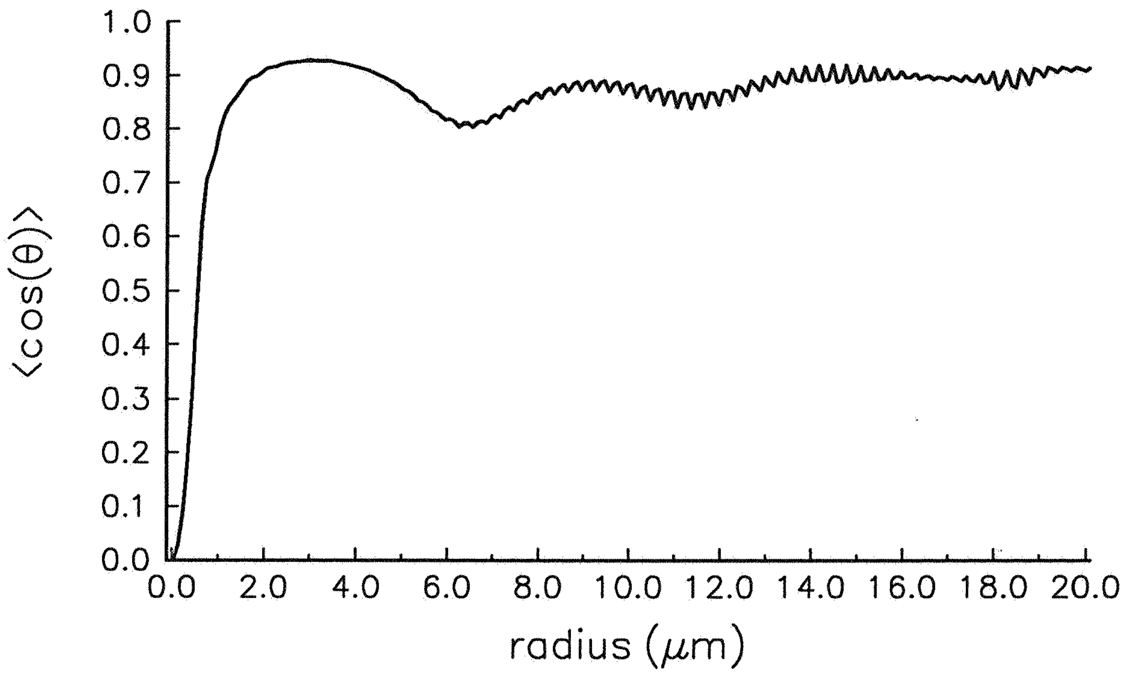

Figure 1: The average scattering angle of polystyrene spheres in water as a function of the radius r. Vacuum wavelength: 633 nm.

Obviously, the contribution of low order of scattering processes is large for the reflected intensity: the n^{th}-order scattering contribution is proportional to $n^{-3/2}$, for large n.[1] The intensity distribution over the different scattering orders can be studied through the shape of the backscatter cone. Recalling the interference pattern of two coherent point sources, one understands that long light paths, with a large separation between start and end point, contribute dominantly in the top of the backscatter cone and that the wings of the backscatter cone originate only from low order of scattering. Hence, by examining the wings of the backscatter cone, the relative contribution of the lowest order scattering processes can be studied. We perform backscatter measurements on aqueous-suspensions of monodisperse polystyrene spheres. By choosing the size of the scatterers, we set the anisotropy of the scattering as can be seen from Fig. 1. We report on our findings in section 6.2.

One could also think of *transmission* experiments where the low order of scattering processes are dominant. In a time resolved experiment, the first transmitted light consists of waves that have taken the shortest paths to cross the system. The shortest paths will be along a low number of almost aligned scatterers, and are thus a selection of the scattering events in the forward direction. These type of experiments are in particular important for imaging applications of objects embedded by diffusely scattering media.[2] Clearly, anisotropic scattering will have a large impact on the properties of the first transmitted light. To study the properties of the first transmitted light in detail we perform simulations, the results of which are given in section 6.3.

6.2 Coherent backscattering

In theory, the shape of the backscatter cone becomes independent on the anisotropy of the scatterers by the use of Eq. (6.1) to incorporate anisotropic (forward) scattering particles.[3] The functional form of the backscattered intensity distribution can then be calculated in a closed expression using a diffusion theory. However, diffusion theory is only valid when the number of scattering events is large. The wings of the cone have only contributions of the lowest order of scattering events. Hence, the full shape can never be described correctly by diffusion theory. Comparing diffusion theory with numerical solutions of the Milne equation one indeed finds that diffusion theory underestimates the lower order of scattering processes. This translates itself into an underestimation of the coherently backscattered light at large backscatter angles.[4] Notwithstanding, measurements on TiO_2-particles are best described with *diffusion* theory.[1]

The key-issue is probably the fact that the TiO_2-particles scatter in the forward direction. Apparently, the errors introduced by diffusion theory are cancelled by the fact that the TiO_2-particles scatter in the forward direction. To support this statement we will study the influence of forward scattering on the shape of the backscatter cone by performing experiments on monodisperse spheres. The size of the spheres sets the amount of forward scattered light per scattering event. Particles which are large compared to the wavelength scatter predominantly in the forward direction, whereas small particles scatter isotropically, see Fig. 1.

We want to study the impact of forward scattering only, therefore we should choose the polarization of the incident light perpendicular to the scanning plane. Small particles with $<\cos\vartheta>=0$ have a Rayleigh phase function that is '8-shaped' for p-polarized light. As a consequence, the p-polarized backscatter cone (scanning plane parallel to the incident polarization) differs from the s-polarized backscatter cone;[5][6] an example is given by Fig. 5 in Chapter 4. By choosing the polarization perpendicular to the scanning plane, we will not encounter this polarization effect.

6.2.1 Measurements

Samples

In the experiments we use various 10 vol. % aqueous-suspensions of monodisperse polystyrene spheres. The diameters of the spheres were chosen such that the values for the average cosine were equidistantly distributed between 0 to 1. In Fig 2 we show polar plots of the scattering behaviour of the polystyrene spheres in water for the polarization vector in and out of the plane of scattering.

We have tried to increase the volume fraction of the spheres in the suspensions by evaporation of the water, in order to have the same transport mean-free path for all samples and to reveal a possible dependence of the shape of the backscatter cone on the transport mean-free path. However, at higher concentrations, 15 vol. %, the spheres cluster and adhere to the container sides. At even higher concentrations they start to form a glassy material. Diluting the suspensions would have given problems with the experimental angular resolving power. So unfortunately, we are not able to make samples with the same transport mean-free path and different anisotropy, nor to vary the mean-free path of the samples over a wide range.

Experimental

The experimental setup used to measure the backscattered light is described in detail in Chapter 3. We use light linearly polarized *normal* to the scanning plane.

In order to exclude the possibility that single scattering could influence the shape of the backscatter cone, we also measure the helicity preserving component of the backscattered light from incident circularly polarized light. By doing this, the single scattering contribution is filtered out.

Differences in the shape of the backscatter cone are made visible by comparing the measurements with a theoretical curve calculated using diffusion theory. Diffusion theory yields a functional form for the backscattered intensity independent on the anisotropy of the scatterers. This is because Eq. (6.1) is used and the backscatter angle is expressed in $(kl_{tr})^{-1}$. Since we are interested in the shape, we will only use the data points near the top to scale the theoretical curve to the measured curve. Long light paths contribute predominantly to the top, as for these paths the diffusion approximation is valid, and it is a natural approach to look at the shape of the cone. There are however theoretical investigations on anisotropic scattering which show that the apex angle of the backscatter cone does not only depend on the transport mean-free path, but also on the second moment of the phase function.[7][8] Investigation of such a correction is not accessible by experiments. The transport mean-free path cannot be determined unambiguously by

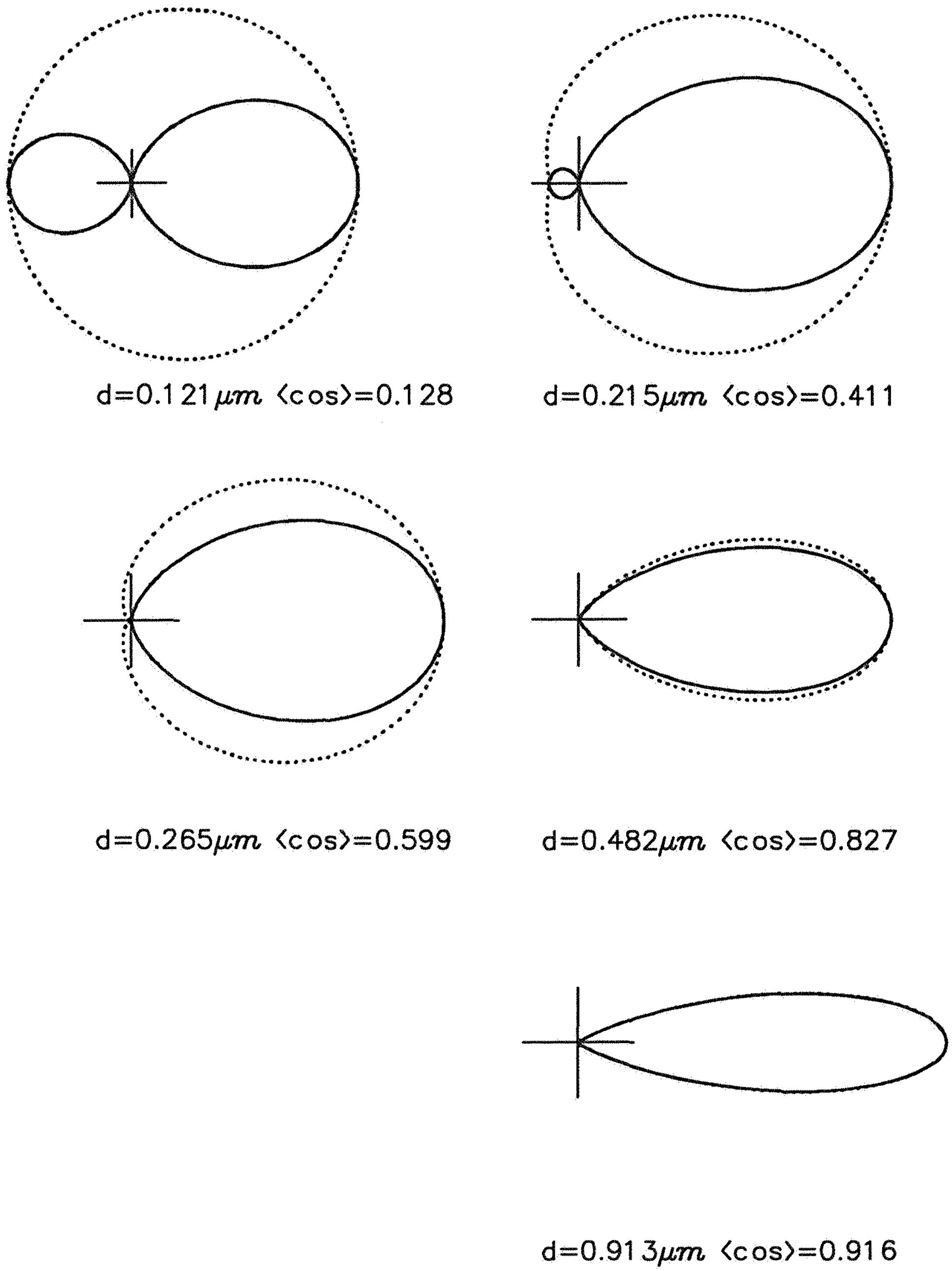

Figure 2: Polar scattering diagrams of polystyrene spheres in water, n=1.195. Light impinges from the left side. Solid lines: polarization in the scattering plane, dotted lines: polarization out of the scattering plane, *d*: diameter, $<\cos>$: average cosine of the scattering angle.

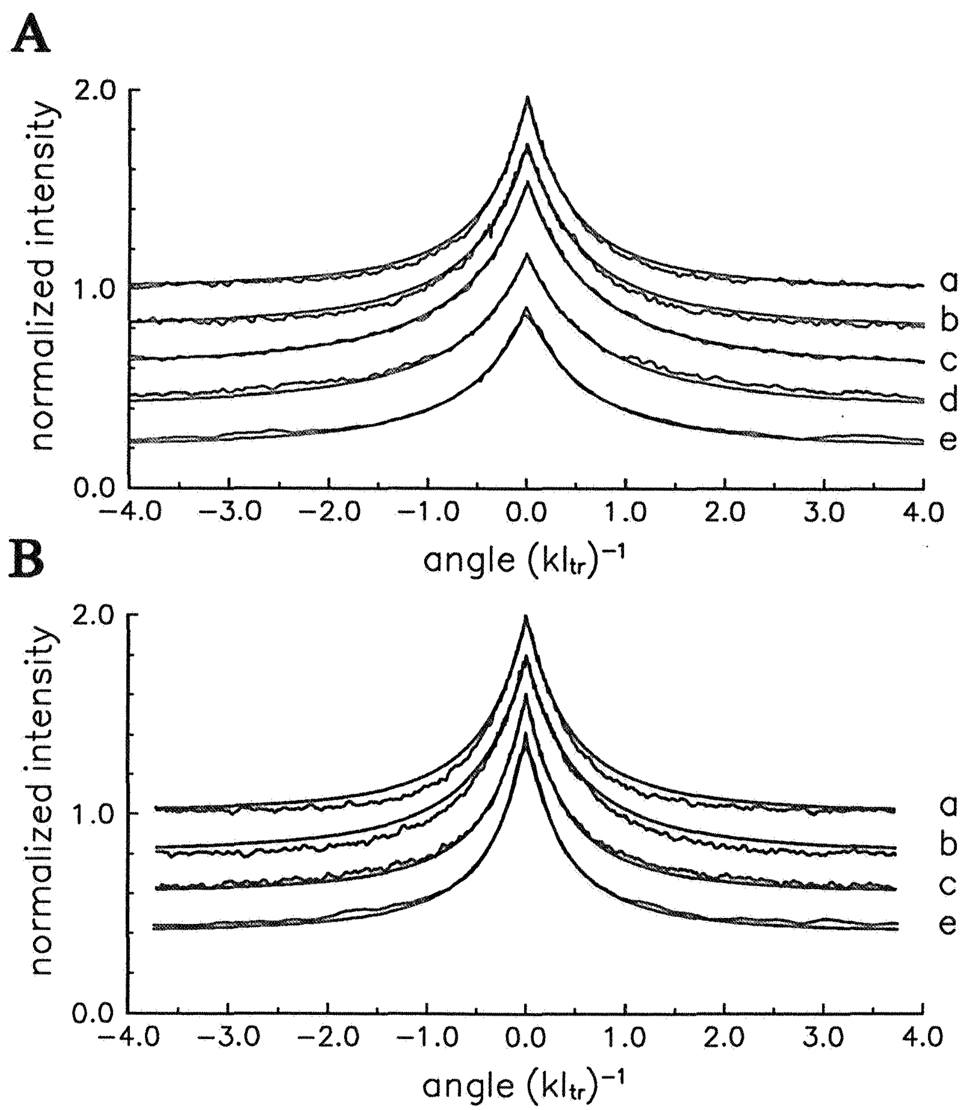

Figure 3: Details of measured backscatter cones from 10 vol. % suspensions of polystyrene spheres. **A**: linear polarization, **B** circular polarization. a) $<\cos\vartheta>= 0.914(1)$; b) $<\cos\vartheta>= 0.808(3)$; c) $<\cos\vartheta>= 0.547(1)$; d) $<\cos\vartheta>= 0.367(1)$; e) $<\cos\vartheta>= 0.114(1)$. Background intensity is normalized to 1, the y-axes have been offset by 0.2 for each successive curve with respect to curve a) in both plots. Smooth curves, diffusion theory, are identical.

other means like a measurement of the total transmission. The total transmission is proportional to the transport mean-free path over the thickness of the sample, but the numerical prefactor might depend on the anisotropy of the scatterers as well. We will assume that the top of the cone is well described by diffusion theory and that its opening angle yields the *transport* mean-free path of the sample.

Results

In Fig. 3A we present details of measured backscattered light. Each curve is accompanied by a theoretical curve calculated using diffusion theory. The backscatter cones for circularly polarized light are shown in Fig. 3B. The scatter angle for each curve in both figures is expressed in $(kl_{tr})^{-1}$ which scales each curve to the same width. The y-axes have been offset in both plots for clarity.

We see clearly that for large particles, the wings of the backscatter cone decay faster with increasing angle than for small particles. For particles having an average cosine of 0.6, the shape coincides with the calculated shape using diffusion theory. This is consistent with experimental observations with TiO_2-samples.[1]. The value of the average cosine of TiO_2-samples is approximately 0.5. Hence, the errors of a theory that underestimates the low order of scattering are here completely compensated by applying the theory to an anisotropic multiple

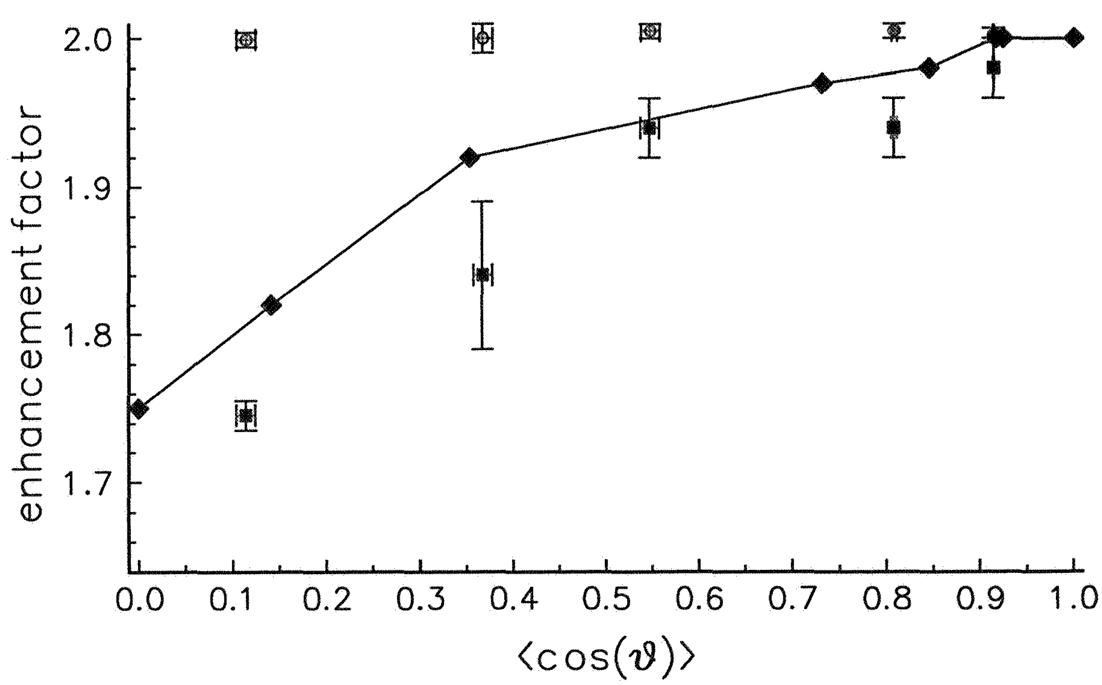

Figure 4: The intensity of the top of the backscatter cone normalized to the diffuse background as a function of the average of the cosine $<\cos\vartheta>$. Circles: circularly polarized light, squares: linearly polarized light. Diamonds connected by a solid line show calculations by Mishchenko.[9]

scattering problem.

In Fig. 4 we plot the enhancement factors of the measured backscatter cones. We show results for linearly as well as for circularly polarized incident light. For circular polarization the determined enhancement factor of the backscatter cone is 2 for all particles. For linearly polarized incident light a reduction of the enhancement factor occurs as a consequence of single scattering. The overall trend is clear, the larger the particle, the more it scatters in the forward direction and the more the single scattering contribution to the reflected light is suppressed. The results of a calculation by Mishchenko are shown as a solid line in the plot.[9] In Ref. [9] the vector radiative transfer equation is solved numerically for the exact backscatter direction.

We do not expect the values of the enhancement factor for linear case to lay much higher as indicated by the calculations of Ref. [9] because we measure an enhancement factor of two for circularly polarized light. In addition, the enhancement factor of the suspension of particles having $<\cos\vartheta>= 0.914(1)$ is already 1.96, which means that if there are still experimental artifacts reducing the enhancement factor in the linearly polarized case, this reduction cannot be larger than 0.04. Note that the calculation of the enhancement factor is not at all a trivial problem, it requires knowledge of the depolarized components of the reflected light as well.

6.2.2 Numerical simulations of the coherent reflected intensity

We can interpret our experimental results on the shape of the backscatter cone as if the transport mean-free path differs from its average value for the low order scattering contributions. An alternative explanation can be put forward as well: 'the amplitude difference between direct and reversed path'.

Calculating in the far field limit the reflected intensity by two scattering events, one finds that the amplitudes of the direct and the time-reversed paths are not necessarily equal. This happens when the observation angle is not strictly backwards, and the particles scatter predominantly in the forward direction. This also holds for higher order scattering sequences. As can be seen in Fig. 5, the total angles traversed by the direct and time-reversed paths differ by twice the angle between backscatter and observation direction. The more away from the backscatter direction, the larger the amplitude difference. Figure 5 plots the polar scattering diagrams at the last scatterer of the followed scattering sequence. Clearly, the amplitudes are unequal for the clockwise and counter clockwise paths. The amplitude difference is larger for forward scattering particles than for more

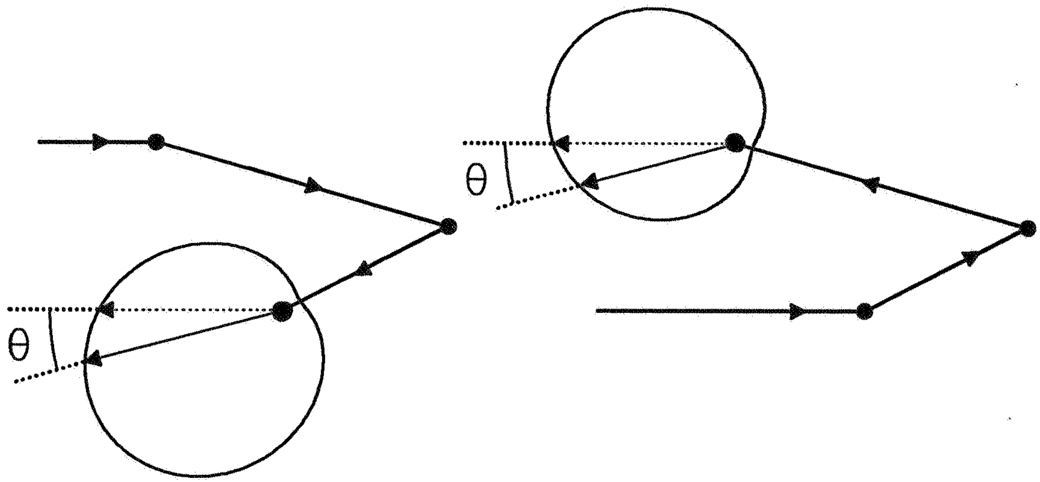

Figure 5: Polar plots of the amplitude of the field scattered from the last particle of a backscatter sequence for two propagation directions (left and right plot). The dotted arrows pointing in the backscatter direction are equal in length, whereas the solid arrows that make an angle θ with the backscatter direction are not.

isotropically scattering ones. The interference term yielding the backscatter cone thus has an extra angle dependence. Additionally, a short mean-free path means a broad cone, the line shape of the backscatter cone should depend also on the mean-free path with respect to the wavelength of the light.

We will investigate whether this explanation is valid by numerical simulation of the coherently backscattered light. We will investigate the influence of the amplitude inequality by comparing simulated backscatter cones where we have taken account of the amplitude inequality with simulated backscatter cones where this is neglected.

The simulation program follows a large number of 'photons' that are one by one injected in a 'disordered medium'. The disorder is a random distribution of identical scatterers, with no restriction on their position. The scattering is conservative, and constrained to two dimensions. In two dimensions, the intermediate polarization states are identical to the initial one, whereas in three dimensions, intermediate polarization states are usually elliptical. This makes two dimensional multiple scattering far more easier to treat than three dimensional scattering. A study of two dimensional scattering is sufficient for our purpose.

Every photon carries the same amount of intensity. The distance to the first and between successive scattering events is randomly chosen from a negative exponential distribution. Hence, the positions of the scatterers are not preset but generated during the simulation for each scattering event and every photon is thus subject to a microscopically different system. This negative exponential distribution also leads directly to an exponentially decaying incoming intensity. This requires less computing time than adjusting the intensity of the photon with respect to the distance it has traversed. In the latter case, a lot of photons are followed that carry little intensity. Furthermore, if the distance to the next scatterer is always the scattering mean-free path, the diffusion constant will not be proportional to the transport mean-free path; an extra term depending on the average cosine enters.[10]-[12] The change in direction is chosen randomly from a distribution of angles, where the probability to pick an angle is taken proportional to a particular phase function (the phase functions we use are comparable with those of the particles in the experiment). Here, the anisotropy of the scattering is thus introduced. The first scattering angle is stored. The distance to the second scattering event is chosen from the negative exponential distribution. Now the amplitude of the reversed light path relative to the direct path is calculated. For this, the stored first scattering angle is needed. The amplitudes and the position of the scatterers determine the interference pattern in the far field. The third and following scattering events are generated by repeating the same procedure. This procedure continues until the photon is outside the sample or it has had more than a certain number of scattering events (it is abruptly absorbed). A next photon is injected and this whole procedure is repeated until a reasonable smooth curve for the backscattered intensity is obtained.

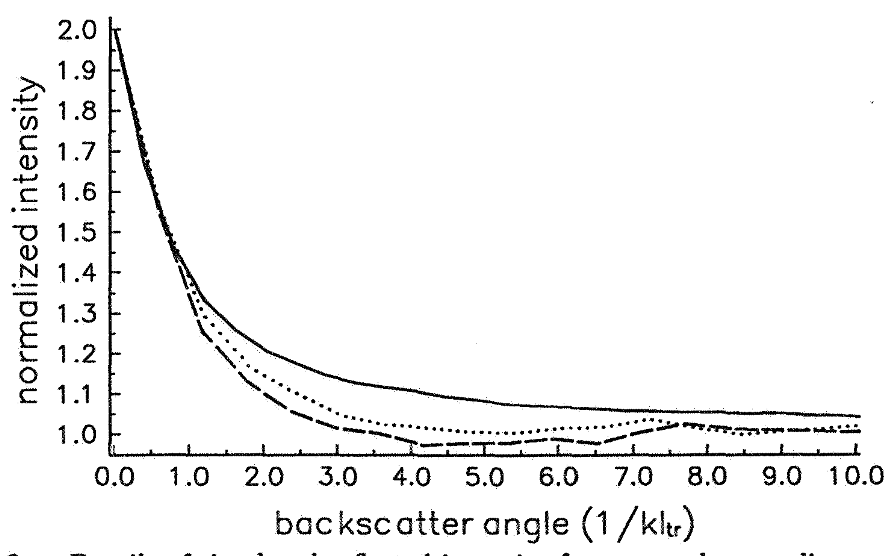

Figure 6: Details of simulated reflected intensity from a random medium containing point scatterers. Solid line: $<\cos\vartheta>=0.14$, dotted line: $<\cos\vartheta>=0.864$, dashed line $<\cos\vartheta>=0.961$. The diffuse background is normalized to 1.

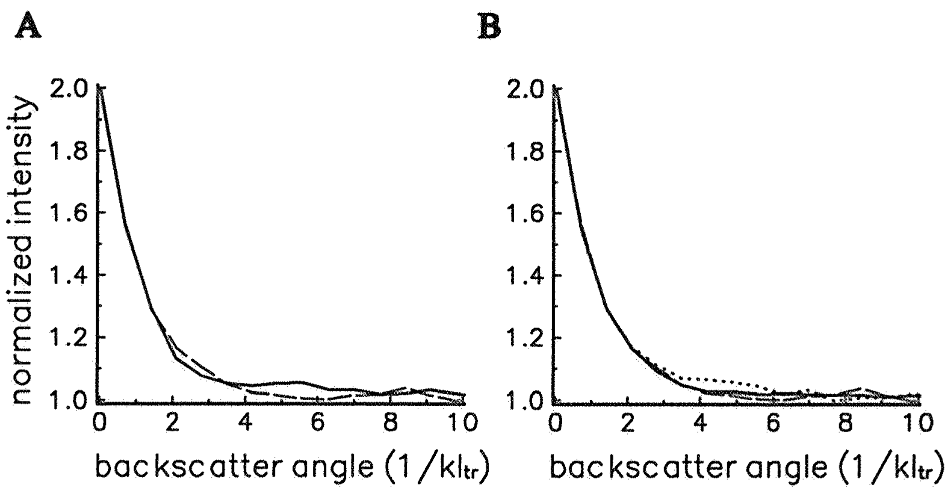

Figure 7: Simulated reflected intensity from a random medium containing point scatterers with $< \cos\vartheta >= 0.864$. Plot A: with amplitude difference (solid line), and amplitude difference neglected (dashed line). Plot B: solid curve $kl_{tr} = 200\pi$, dotted curve $kl_{tr} = 20\pi$, dashed curve $kl_{tr} = 4\pi$.

Results

In Fig. 6 we plot the simulated reflected intensity for three different phase functions. We indeed observe similar behaviour as in the experiment: forward scattering particles have a lower intensity in the wings of the backscatter cone than isotropically scattering particles.

We compare the simulated backscatter cones with those when the amplitude difference is neglected, i.e. taking account only of the relative position of the scatterers. Surprisingly, we do not observe noticeable differences between the two ways of simulation, see Fig. 7 A. The shape of the backscatter cone also turns out to be independent on the mean-free path, Fig. 7 B. The reflected intensity is simulated for 3 different values of kl_{tr}. Evidently, the amplitude difference is not important to explain the experimental observations.

6.2.3 Conclusions

We found that forward scattering is not fully taken into account by the use of the transport mean-free path. The shape of the backscatter cone is subject to the anisotropy of the scattering. Diffusion theory, which underestimates the low order of scattering events, yields the same shape as a measurement on particles with a phase function having an average cosine of 0.5. The numerical simulations

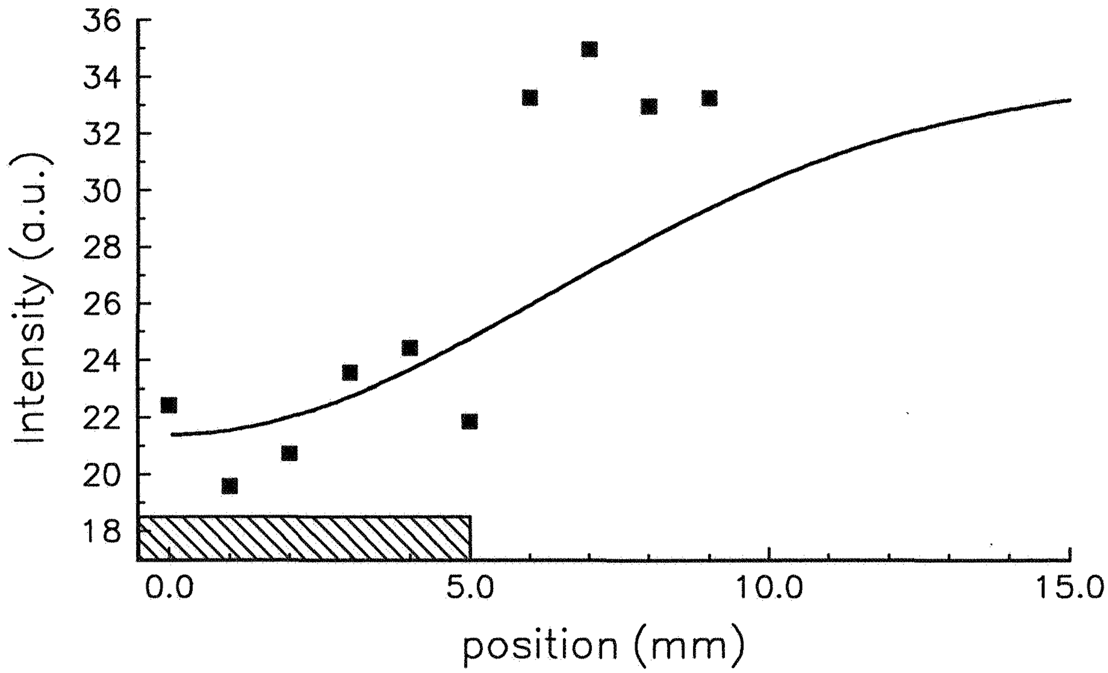

Figure 8: Experimental results of Ref. [13] (squares) compared with diffusion theory (solid line). See text for explanation.

have shown that the inequality in amplitudes of direct and reversed paths is not important for the shape of the backscatter cone.

6.3 Simulation of the time resolved transmission

Time resolved transmission experiments are performed to image objects embedded by a multiply scattering medium.[2] The first idea was to measure the direct transmitted light of a short laser pulse. However, the limitations on the probing depth are serious because the intensity of the directly transmitted light decays exponentially with increasing sample thickness. To improve on the probing depth, one uses the scattered light that is first transmitted.[13]-[17] This light has crossed the scattering medium in almost straight lines and can still be used to create an image of an embedded object. We will adopt from the literature the term 'snake-like photons' for the first transmitted light. The intensity of the snake-like photons still decays exponentially with increasing sample thickness, but the length scale is much larger.

To give an idea of the type of experiments that are performed, we plot in Fig. 8 the experimental results of Yoo *et.al.*[13] The intensity transmitted between 0.240 and 0.290 *ns* after the injection of a short light pulse (0.1 *ps*) was measured. A detector and the focused light source, with fixed distance to each other, were scanned parallel along the slab. The diffusion constant inside the slab is $4 \cdot 10^5 m^2/s$, a small region with a lower diffusion constant is embedded by the slab, i.e. the object to be imaged. In Fig. 8 the extension of this region is indicated as a hatched area. A blurred 'shadow' of this region is observed. Comparing this experimental result with diffusion theory, it becomes clear that this blurring is actually very small; diffusion theory gives a large overestimation. The blurring of the shadow according to diffusion theory is represented by a solid line in the same figure.

Similar observations are made in *static* transmission experiments through thin slabs by Li *et.al.*[18] In thin slabs, only low order of scattering processes can occur, and also here an overestimation by diffusion theory is found for the blurring of a point source (the width of the point spread function). In fact, the overestimation of the width of the point spread function, when the number of scattering events is small, is consistent with the results of section 6.2. Too broad a point spread function means a relative too high contribution of the higher order scattering events, or equivalently, an underestimation of the low order scattering contributions as found in section 6.2.

An important point is whether the transport of the snake-like photons can be described by a diffusion equation. If this is indeed the case, the snake-like photons do not contain, in principle, more information of the embedded object than the multiply scattered light.[1] One can rephrase this point into the question if the snake-like photons are those waves that scatter only a few times with a large separation.

Since the experiments performed[13][14] cannot be described fully by a diffusion theory, we will not learn more about the snake-like photons by studying solutions of the diffusion equation at short time scales. Moreover, we want to know whether or not the snake-like photons fulfil a diffusion equation. Therefore, we will perform simulations.

The interesting parameter to vary in the simulations is the anisotropy of the scatterers. The snake-like photons are a selection of multiply scattering events in the forward direction, and hence the expected influence of anisotropic scattering (forward scattering) is large. We will study the impact of forward scattering on the length scale of the exponential decay of the transmission, determining the transmission coefficient, the point spread function, which is inversely proportional to the imaging resolution, and the number of scattering events needed to traverse the sample. In addition, the influence of forward scattering on the total (time

[1]What information of the object is still contained by the multiply scattered light will be investigated in the next chapter.

integrated) transmission is also studied.

The influence of an embedded object on the transmission of the snake-like photons is not simulated. Anticipating on the results of Chapter 7, if one knows the response of a system to a point source, which is studied in this section, in principle the response of the system with an embedded object can constructed.

We will present the results of the simulation in section 6.3.2. To interpret our results, we will make a comparison with diffusion theory in section 6.3.3.

6.3.1 Structure of the simulations

The structure of the simulation is the same as that of the simulation of the backscatter cone. Again the scattering is restricted to two dimensions. The snake-like photons are defined experimentally as the light transmitted within a certain time window. Usually, the time window extends from the 'coherent time' to cross the sample to 1.1 times the coherent time. The coherent time t_c is the time needed for the coherent beam to cross the sample. It is given by the sample thickness L over the phase velocity v, $t_c = L/v$. In the simulation we define the time delay between injection and transmission to be the total path length a 'photon' has taken to cross the scattering medium. We set four 'time windows' for the transmitted photons: a path length smaller than $1.1L$ (the snake-like photons) between $1.1L$ and $2L$, between $2L$ and $7L$, and longer than $7L$. The distance ρ the photon has traversed parallel to the slab is meshed into 361 positions symmetrically around the location directly opposite to the point source. The maximum detectable transversal displacement is restricted to 4L. As a consequence, a small fraction of the transmitted photons, less than 0.1 percent typically, will not be counted. These photons will have a minimal path length of $\sqrt{17}L$ and thus belong in the third or fourth time window. The exact total transmission can still be obtained from the number of reflected photons, which are only counted. We do not take into account the direction of the transmitted photons. A few preliminary simulations have shown that only for slabs with a thickness $L < 4l_{tr}$, improvement of the resolution cannot be made by selecting photons that are transmitted normally to the slab.

6.3.2 Results

In Fig. 9 we plot the simulated 'time resolved' transmission. The noteworthy shape of the point spread function for the second and third time window occurs only for thin slabs ($L < 4l_{tr}$). For thicker slabs, the highest transmission is opposite to the point source for all time windows. Note that diffusion theory gives for all thicknesses and time windows the highest transmission probability directly

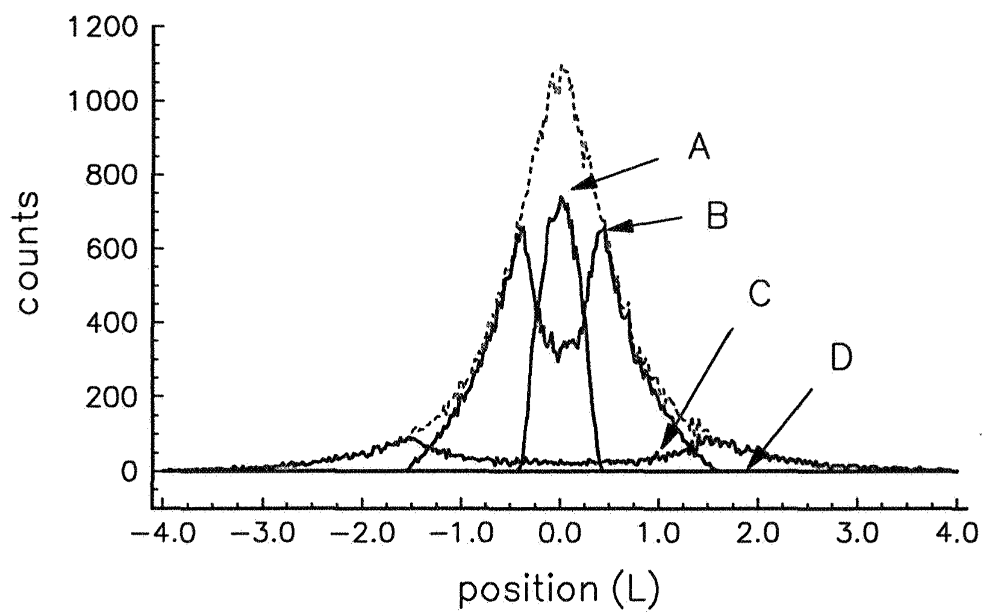

Figure 9: Simulated transmission for four time windows. Thickness of the slab: $L = 45.72$, $l_{tr} = 45.72$, $<\cos\vartheta>= 0.978$, number of injected photons: $1 \cdot 10^5$. Curve A: contributions with path length $< 1.1L$, A: $1.1L <$ path length $2L$, C: $2l <$ path length $< 7L$, D: $7L <$ path length, the dashed curve is the sum of all contributions.

opposite to the point source.

First, we discuss the total 'time' and angle integrated transmission which should be inversely proportional to the thickness of the slab. Applying diffusion theory to calculate the total transmission however, yields different prefactors depending on the approximation made for the source of diffuse intensity and the boundary conditions on the diffuse intensity.

The solution of the diffusion equation with a point source for the diffuse intensity, and boundary conditions on the diffuse intensity given by

$$I(0) - z_0 \left.\frac{dI}{dz}\right|_{z=0} = 0, \quad \text{and} \quad I(L) + z_0 \left.\frac{dI}{dz}\right|_{z=L} = 0, \tag{6.2}$$

yields for the total transmission (integrated over the transverse coordinate)

$$T(L) = \frac{z_s + z_0}{L + 2z_0}, \tag{6.3}$$

with z_0 being the extrapolation length and z_s the effective location of a diffuse point source. The diffusion result for the extrapolation length z_0 for two dimensions can be calculated similarly as in Chapter 5. We find $z_0 = \frac{\pi}{4} l_{tr}$. The effective location

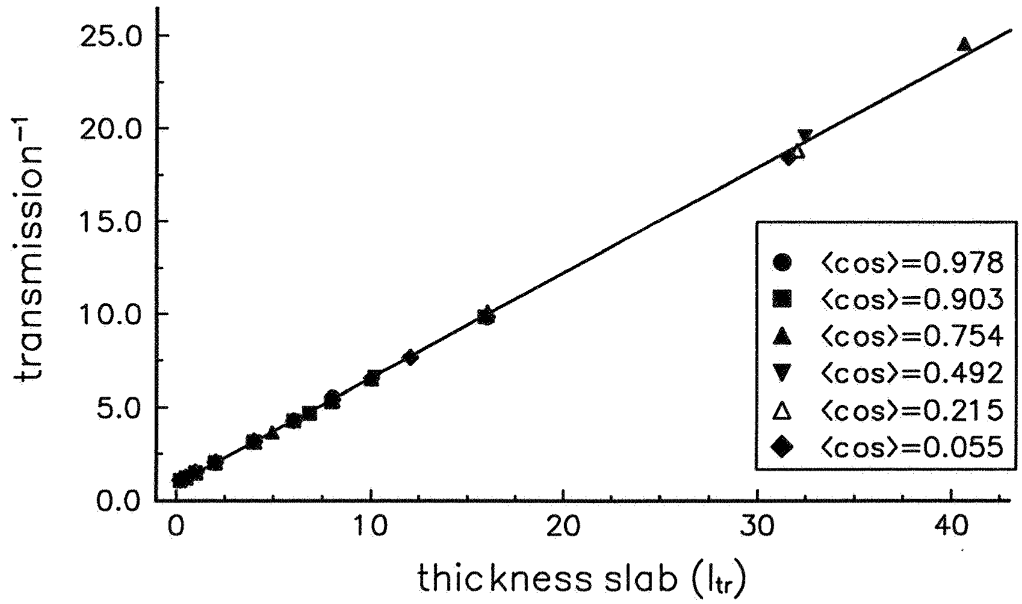

Figure 10: The inverse of the total transmission as a function of the thickness of the slab for various phase functions of the scatterers. The solid line is a numerical fit of Eq. (6.3).

of the diffuse point source can be taken at one transport mean-free path in the sample.

Following Van de Hulst[19] we plot in Fig. 10 the *inverse* of the total transmission as a function of thickness of the slab expressed in the transport mean-free path. Actually, we have plotted the inverse of the diffuse *plus* the directly transmitted light. As should be noticed from the plot, the total transmission is independent on the phase function of the scatterers. We show also the prediction of Eq. (6.3) with z_0 and z_s varied to obtain the best correspondence with the simulated data points. We find for the extrapolation length $z_0 = (0.77 \pm 0.02)l_{tr}$ which is close to the diffusion result $z_0 = \frac{\pi}{4}l_{tr} \approx 0.785 l_{tr}$. The effective location of the diffuse source is found to be $z_s = (0.98 \pm 0.02)l_{tr}$ which was expected to be close to one transport mean-free path. Hence, experiments involving a high number of scattering events, anisotropic scattering is completely accounted for by the introduction of the transport mean-free path.

The transmission of the snake-like photons as a function of the thickness of the slab is shown in Fig. 11. Only the photons are counted that are transmitted directly opposite to the source, $|\rho| < L/45$. The thickness is expressed in scattering mean-free paths. We indeed observe an exponential decay of the intensity with increasing thickness. There is a strong dependence on the phase function of the

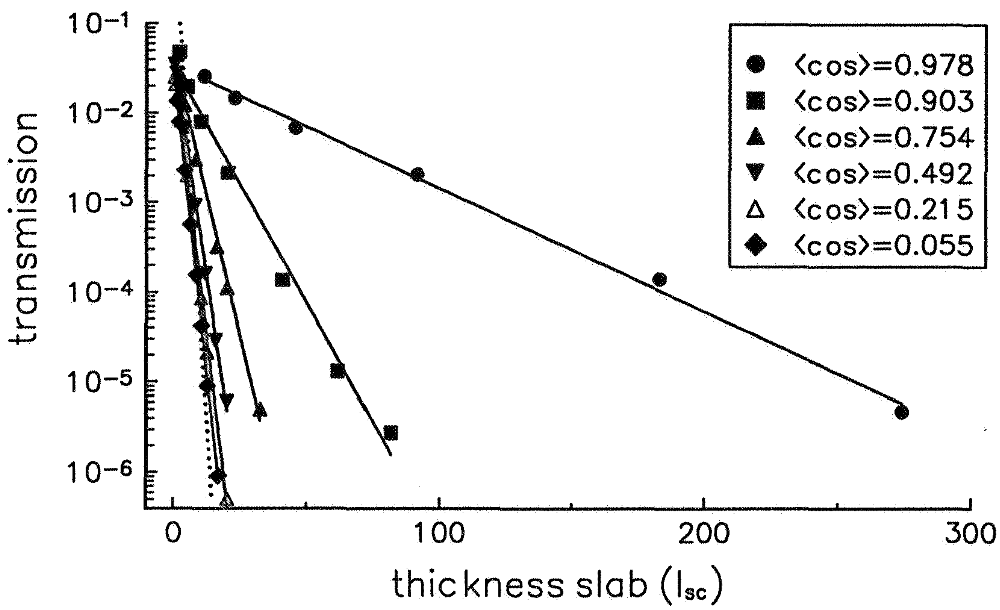

Figure 11: Transmission of 'photons' with total path length $< 1.1L$. Solid lines are exponential fits to the data points. The dotted line is the direct transmitted light.

scatterers. In Fig. 12 we plot the decay constant of the transmission for the different phase functions, i.e. the 'snake mean-free path' l_{sn}, as a function of the average cosine. The transport mean-free path is slightly larger than the snake mean-free path for strictly forward scattering phase functions. A straight line as a function of the average cosine is found by dividing the snake mean-free path by the transport mean-free path, see Fig. 12. We find empirically the relation

$$l_{sn} = \frac{(1.57 \pm 0.02) - (0.89 \pm 0.03) <\cos\vartheta>}{1- <\cos\vartheta>} l_{sc}. \tag{6.4}$$

Figure 13 plots the number of steps taken by the snake-like photons to traverse the system as a function of the thickness of the slab. The result indicates that the average number of steps increases *linearly* with increasing sample thickness, and not quadratically as one would expect for a diffusion process.

It became clear that the intensity of the snake-like photons can be orders of magnitude higher than the direct transmitted light. Forward scattering is crucial to have this higher transmitted intensity. Hence, we can win intensity by using the first transmitted light instead of the direct transmitted light, but resolution is lost since the probing light is scattered.

To study the achievable resolution in a transmission measurement, we de-

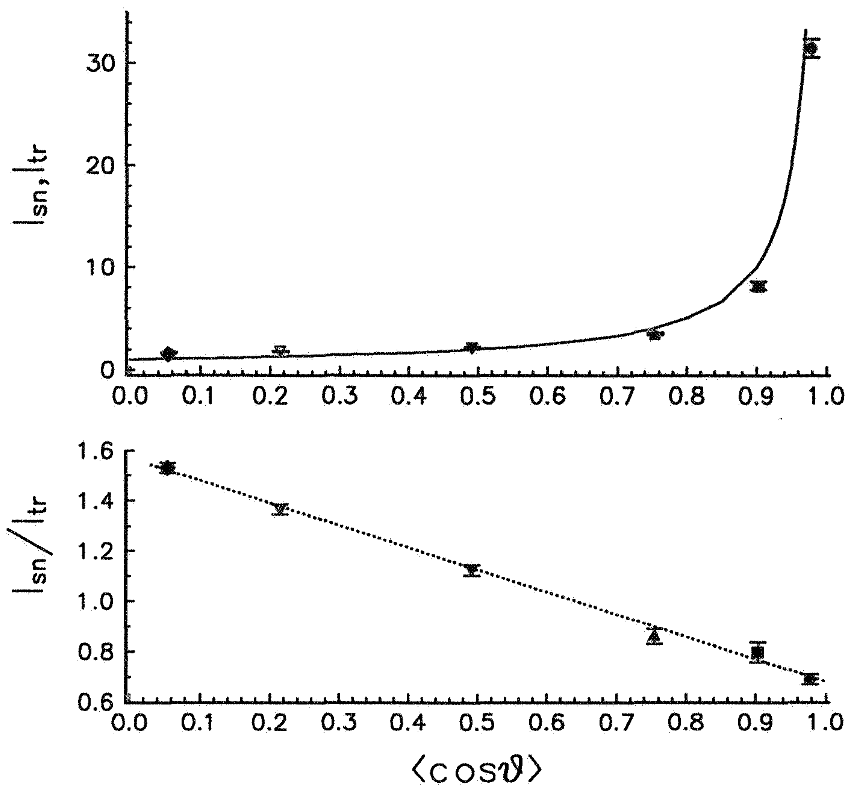

Figure 12: The 'mean-free path' of the snake-like photons plotted vs. the average cosine of the phase function of the point scatterers, solid line: transport mean-free path. Lower plot: quotient of snake mean-free path and transport mean-free path, dotted line Eq. (6.4). The legend used is that of Fig. 11.

termine for each simulation the width of the intensity profiles at half maximum, which is essentially inversely proportional to the resolution. We should compare (divide) this width with that of the time-independent intensity profile. This ratio expresses the achieved improvement in resolution when using the snake-like photons. For slabs optically thicker than 6, the time integrated point spread function follows the prediction of diffusion theory, given in Chapter 7. A triangular shaped intensity profile is found for optically thin slabs, and we just use the width at half maximum.

In Fig. 14 we plot the width of the point spread function of the snake-like photons, $PSF(p < 1.1L)$, relative to the width of the time independent point spread function, PSF, as a function of the thickness of the slab. Two plots are shown: in the left plot the thickness of the slab is expressed in scattering mean-free path, in the right plot the transport mean-free path is used to express

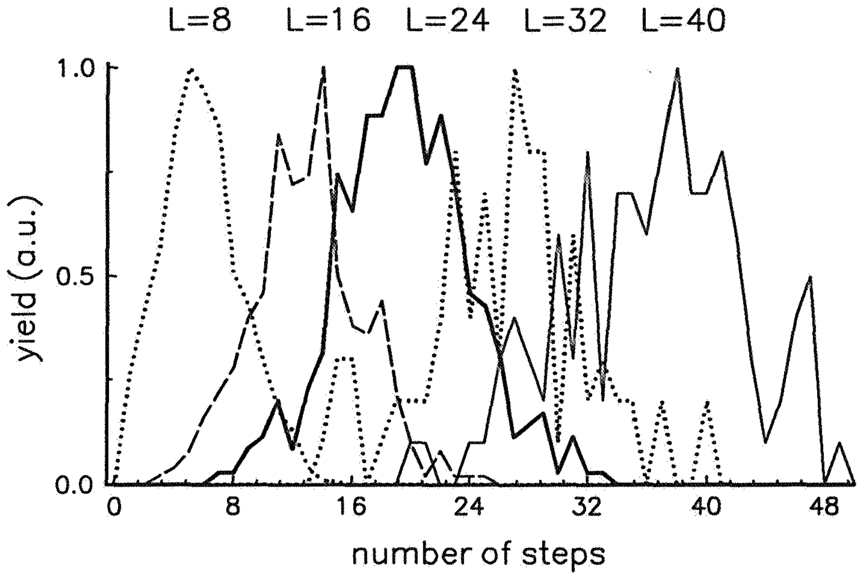

Figure 13: Number of steps needed to cross the sample for the snake-like photons. Scatterers with <cos ϑ>= 0.754.

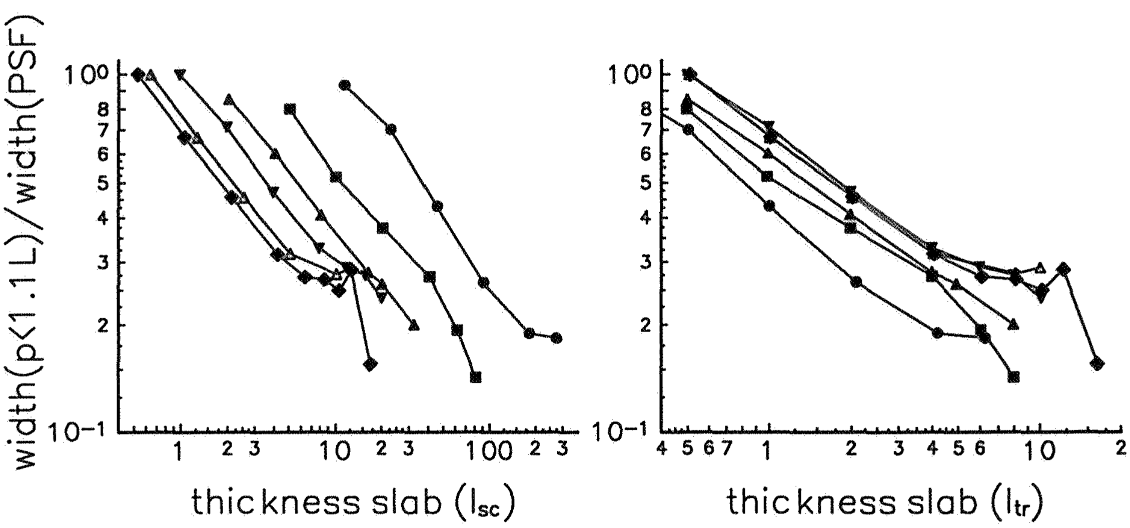

Figure 14: Width of the point spread function of the snake-like contribution relative to the width of the time-independent transmission profile as a function of the thickness of the slab for various phase functions of the point scatterers. The legend used is that of Fig. 11.

this thickness. Striking is that isotropic scatterers yield a better resolution than forward scatterers when a slab thickness is given in units of scattering mean-free paths. In contrast, when using the transport mean-free path, we find the opposite. Hence, similarly as for the snake mean-free path, a residual dependency of the resolution on the average cosine <cos ϑ> is found.

The simulations indicate that the resolution improves with a power law as the thickness of the sample increases; and generally: the lower the transmission the higher the resolution.

6.3.3 Diffusion theory

Although diffusion theory does not give quantitatively correct results for low order of scattering processes, it can still be very useful to understand qualitatively some of the experimental or simulation results. The time dependent diffusion equation is given by

$$\frac{\partial}{\partial t} I(\mathbf{r},t) = D\Delta I(\mathbf{r},t), \tag{6.5}$$

with $D = \frac{1}{3} v l_{tr}$ the diffusion constant of the scattering medium, and v the energy transport velocity, see Chapter 2. The difference between phase and energy transport velocity will be small if the scattering inside the disordered medium is non-resonant,[20] which is the situation in practice for the systems we are interested in here. We will take v the phase velocity in the sample.

The solution of the time dependent diffusion equation for a slab geometry can again be found by using mirror images of the solution for the infinite medium. The slab is situated between $z = 0$ and $z = L$ as before. We will assume the incoming beam to create a diffuse source at one mean-free path l_{tr}. The transmitted intensity through the slab is then given by

$$\begin{aligned} T(L,t,a) &= \frac{\exp(-D/L_{abs}^2 t)}{(4\pi D t)^{\frac{3}{2}}} \sum_{n=-\infty}^{n=\infty} \exp\left(-\frac{\rho^2 + (L - l_{tr} + 2n(L+2z_0))^2}{4Dt}\right) \\ &\qquad - \exp\left(-\frac{\rho^2 + (L + l_{tr} + 2z_0 + 2n(L+2z_0))^2}{4Dt}\right), \qquad (6.6) \\ \rho^2 &= x^2 + y^2. \end{aligned}$$

The snake-like photons are defined as the intensity transmitted within a certain time window: i.e. the coherent time to cross the sample, $t_c = L/v$, to $(1+\alpha)t_c$, with α small ($\alpha = 0.1$ typically). Examining Eq. (6.6) for times close to the coherent time, we can approximate Eq. (6.6) by retaining only the lowest order of n. Here we see the large advantage of the use of the snake-like photons: the intensity distribution on these short time scales is insensitive to the boundaries of the scattering medium; the snake-like photons behave as if they are in an infinite medium. Taking into account only the first term of Eq. (6.6), the integration over time can be performed analytically to obtain the intensity of the snake-like photons. The total intensity of the snake-like photons is (integrated over ρ, and for $a = 1$)

$$T_s(L) = \int_{t_b}^{(1+\alpha)t_b} dt \frac{1}{\sqrt{4\pi Dt}} \exp\left(-\frac{(L-l_{tr})^2}{4Dt}\right). \tag{6.7}$$

Introducing the variable ζ by writing $t = (1+\zeta)L/v$ we find

$$\begin{aligned} T_s(L) &\approx \frac{1}{\sqrt{4\pi D}}\sqrt{\frac{L}{v}} \int_0^{\alpha} d\zeta (1 - \frac{1}{2}\zeta) \exp\left(-\frac{3(L-l_{tr})^2}{4Ll_{tr}}(1-\zeta)\right) \\ &\approx \frac{1}{\sqrt{4\pi D}}\sqrt{\frac{L}{v}} \alpha \exp(-\frac{3}{4}\frac{L}{l_{tr}}). \end{aligned} \tag{6.8}$$

Hence, diffusion theory also predicts an exponential decay of the snake-like photons for increasing sample thickness. The intensity is proportional to the width of the time window. The snake mean-free path l_{sn} is $(4/3)l_{tr}$, which would be $2l_{tr}$ in two dimensions, since the diffusion constant is $D = \frac{1}{2}vl_{tr}$ for two dimensions.

The resolution is inversely proportional to the width of the point spread function of the snake-like photons. The latter is essentially the width of the Gaussian function of Eq. (6.6) at a time $t = 1.1t_c$. Dividing by the width of the time-independent intensity profile, we find for large thicknesses for this ratio

$$W_d = \sqrt{2.2\ln(2)l_{tr}/L}. \tag{6.9}$$

There is indeed a power law behaviour. We also learn that the width of the point spread function of the snake-like photons is proportional to the transport-mean free path. This explains the counter intuitive results of the left plot in Fig. 14: the blurring of a point source is larger if the scattering is anisotropic than when the scattering is isotropic for a given thickness of a slab expressed in *scattering* mean-free paths.

To study the influence of the time window on the snake-like photons we will integrate Eq. (6.6) numerically for various upper integration boundaries. This upper boundary can be chosen proportional to the coherent time to cross the sample: $t_{max} = (1+\alpha)t_b$, or just a constant delay time independent on the thickness of the slab: $t_{max} = t_b + \Delta t$. The first situation is shown in the left plot, the latter in the right one of Fig. 15. The intensity of the transmitted snake-like photons changes drastically when the upper integration boundary is varied. The influence on the exponent or 'mean-free path' of the snake-like photons is larger for the thickness dependent integration boundary (left plot) than for the fixed one. If the upper integration boundaries are close to the coherent time to cross the sample, both ways of integration give the same exponent.

It is illustrative to calculate the transmission as a function of thickness by numerical integration of Eq. (6.6) for a much wider range of upper integration boundaries. When the upper integration boundary becomes large, the exponential

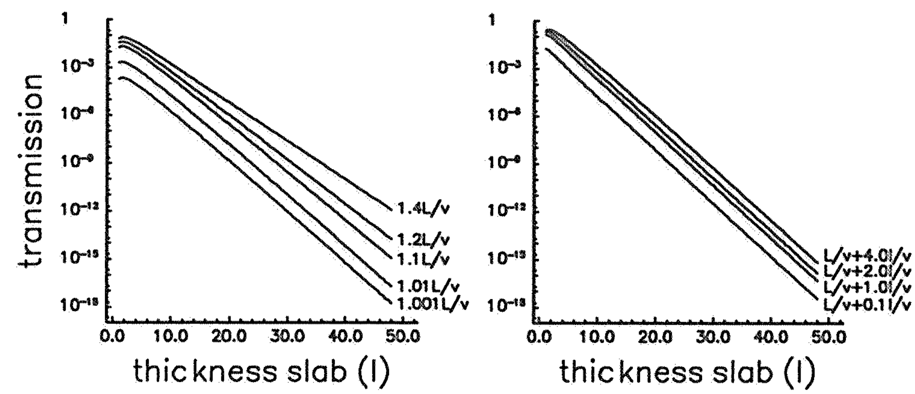

Figure 15: Intensity of the snake-like photons as a function of the thickness of the slab. In the left curve the upper integration boundary is proportional to the thickness of the slab, where as in the left plot it is fixed.

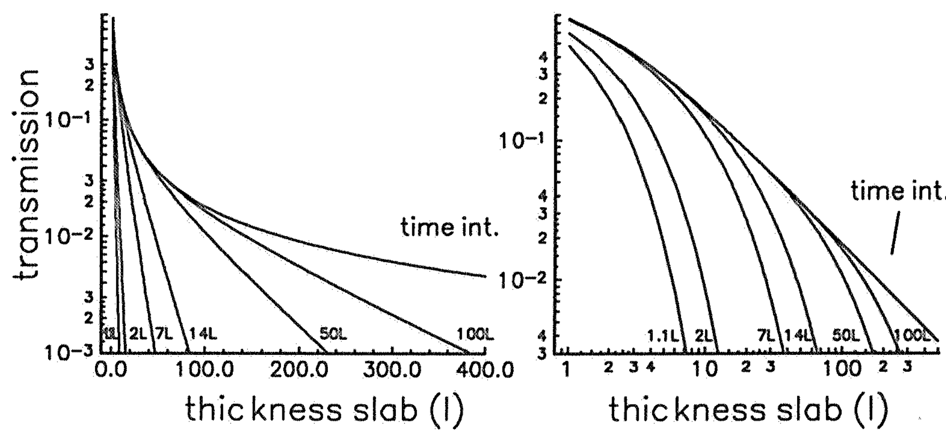

Figure 16: Integration of the time resolved transmission for different upper integration boundaries. The upper integration boundary is $t_{max} = \alpha L/v$. The left plot shows that for fixed α there is always an exponentially decaying contribution for sufficiently thick slab. The right plot reveals the time-independent diffusion result: $T \propto \frac{1}{L+2z_0}$.

decay turns over into the algebraic decay for the time independent situation, see Fig. 16. In the left plot we observe that, no matter how large we choose the upper boundary, there is always an exponential decay of the transmission for sufficiently thick slabs. In the right plot (double logarithmic plot), the inverse proportionality of the transmission on the thickness of the slab emerges.

Thus we quantitatively understand the results of the simulations. However, a residual dependency on $<\cos\vartheta>$ clearly exists after the transport mean-free path is used to measure the thickness of the slabs. Diffusion theory does not give this result because it is essentially a theory for isotropic scattering. Using a transport mean-free path, isotropic scattering is only mimicked. Note however that a summation has implicitly been performed over all orders of scattering events by the introduction of the transport mean-free path. For any property $F(a)$ of multiply scattered light the contribution per scattering order is given by[1]

$$F(a) \quad = \quad \sum_0^{\infty} \frac{1}{n!} \left. \frac{d^n F(a)}{da^n} \right|_{a=0} a^n. \tag{6.10}$$

Applying this formula to the transport mean-free path, one clearly sees it to be the sum of an infinite series of scattering events

$$l_{tr} \quad = \quad l_{ex} + a <\cos\vartheta> l_{ex} + a^2 <\cos\vartheta>^2 l_{ex} + a^3 <\cos\vartheta>^3 l_{ex} .... \tag{6.11}$$

At the boundary of a scattering medium, or for short times as in the case of the snake-like photons, this summation is definitely truncated, and a different value for l_{tr} occurs. Guided by this idea, we will recalculate the snake mean-free path as a function of the average cosine. But now we build in a truncation on the highest order of scattering event depending on the slab thickness

Starting from Eq. (6.6) for 2 dimensional systems, we first integrate out the transversal coordinate $\rho = y$ over a small interval proportional to the thickness of the slab (similarly as in the simulations). Again, we only take account of the first term of the summation of Eq. (6.6)

$$\begin{aligned} T_s(L,t,a) \quad \approx \quad & \frac{2L}{4\pi v l_{ex} t} \exp[-(\frac{v}{l_{ex}}t + \frac{2L^2}{4 v l_{ex} t})] \times \\ & \exp[a(\frac{v}{l_{ex}}t + \bar{\mu}\frac{2L^2}{4 v l_{ex} t})](1 - a\bar{\mu}), \end{aligned} \tag{6.12}$$

where $\bar{\mu} = <\cos\vartheta>$, and we have used the two dimensional analogue of Eq. (2.107) of Chapter 2. Applying Eq. (6.10) we find for the $\mathrm{n^{th}}$-order scattering contribution

$$\begin{aligned} T_n(L,t,a) \quad = \quad & \frac{1}{n!} a^n \frac{L}{2\pi v t l_{ex}} \exp[-(\frac{vt}{l_{ex}} + \frac{L^2}{2 v t l_{ex}})] \times \\ & \left\{ (\frac{vt}{l_{ex}} + \bar{\mu}\frac{L^2}{2 v t l_{ex}})^n - n\bar{\mu}(\frac{vt}{l_{ex}} + \bar{\mu}\frac{L^2}{2 v t l_{ex}})^{n-1} \right\}. \end{aligned} \tag{6.13}$$

The results of the simulations indicate that the number of steps needed to cross the sample is proportional to the sample thickness, see Fig. 13. Hence, we will make a crude approximation by restricting the number of scattering events to a number given by the total distances the photons have traversed ($1.1L$) divided by

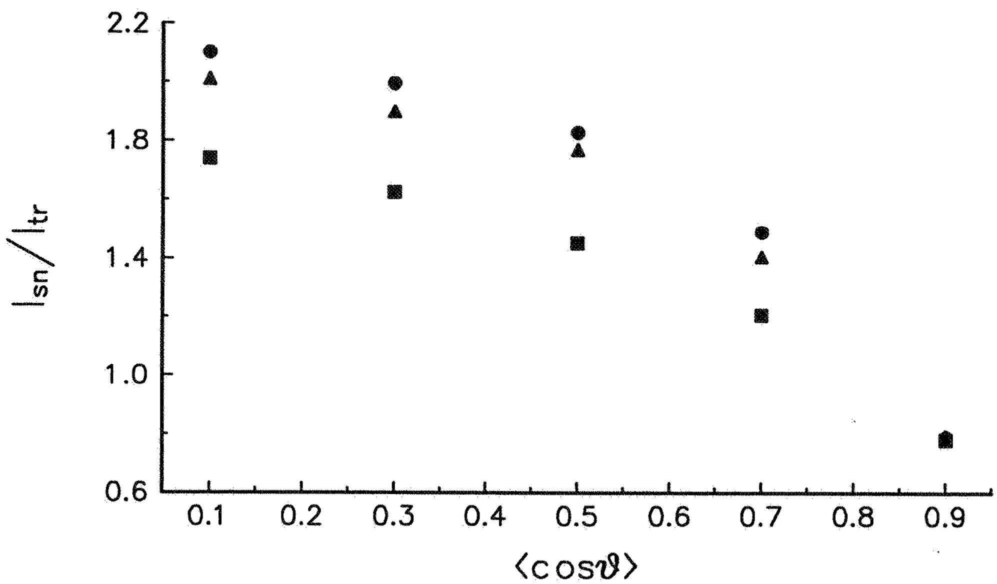

Figure 17: Snake mean-free path calculated by restricting the maximal number of scattering events for different albedo's of the scatterers. Circles: a=0.99, triangles: a=0.97, boxes: a=0.9.

the average distance between scattering events (l_{ex}), $N_{max} = 1.1L/l_{ex}$. We thus express the transmitted intensity of the snake-like photons as

$$T_s(L, t = 1.1L/v, a) = \sum_{n=0}^{N_{max}} T_n(L, t = 1.1L/v, a). \tag{6.14}$$

Using this equation we calculated the snake mean-free path as a function of the average cosine. The result is given in Fig. 17. Indeed, we observe now a functional dependency of the snake-mean free path on the average cosine $<\cos\vartheta>$ different from the behaviour of the transport mean-free path. Since in general the resolution improves when the transmission decreases, we understand in the same scope the better resolution for forward scattering particles as found in the right plot of Fig. 14. The cut off of the summation at a number close to $1.1L/l_{ex}$ is probably too stringent, consequently a too strong dependency on the average cosine compared with the simulations is found.

We conclude that the snake-like photons scatter only a few times with a large separation between successive scattering events. Therefore, they do not diffuse through the medium and thus may carry more information of an embedded object than the diffuse light. Returning to the results of section 6.2, truncation of the summation yielding the transport mean-free path happens also at the boundary. This probably explains that the shape of the backscatter cone depends on the anisotropy of the scatterers and that the enhancement factor of the backscatter cone does not follow the calculations of Mishchenko.[9]

References

[1] M.B. van der Mark, M.P. van Albada, and A. Lagendijk, *Light scattering in strongly scattering media: Multiple scattering and weak localization*, Phys. Rev. B **37**, 3575 (1988).

[2] *see Chapter 7 for review.*

[3] P.E. Wolf, G. Maret, E. Akkermans, and R. Maynard, *Optical coherent backscattering by random media: an experimental study*, J. Phys. France, **49**, 63 (1988).

[4] B.A. van Tiggelen, 'Multiple scattering and localization of light', Ph.D. Thesis, Universiteit van Amsterdam, 1992.

[5] M.P. van Albada, M.B. van der Mark, and A. Lagendijk, *Observation of weak localization of light in a finite slab: anisotropy effects and light path qualifications*, Phys. Rev. Let. **58**, 361 (1988).

[6] M. Ospeck and S. Fraden, *Influence of reflecting boundaries and finite interfacial thickness in the coherent backscatter cone*, Phys. Rev. E, **49**, 4578 (1994).

[7] V.D. Ozrin, *Exact solution for coherent backscattering from a semi-infinite random medium of anisotropic scatterers*, Phys. Lett. A **162**, 341 (1992). V.D. Ozrin, *Exact solution for coherent backscattering of polarized light from a random medium of Rayleigh scatterers*, Waves in Random Media **2**, 141 (1992).

[8] Th.M. Nieuwenhuizen, private communication.

[9] M.I. Mishchenko, *Enhanced backscattering of polarized light from discrete random media: calculations in exactly the backscattering direction*, J. Opt. Soc. Am. A **9**, 978 (1992).

[10] A.H. Gandjbakhche, R.F. Bonner, and R. Nossal, *Scaling relationships for anisotropic random walks*, J. Stat. Phys. **69**, 35 (1991).

[11] A.S. Martinez, 'Statistique de polarisation et effet Faraday en diffusion multiple de la lumiere', Ph.D. thesis, Grenoble, 1993.

[12] A. Heiderich, A.S. Martinez, R. Maynard, and B.A. van Tiggelen, *The role of the step length distribution in wave-diffusion*, submitted to Phys. Lett. A.

[13] K.M. Yoo, B.B. Das, and R.R. Alfano, *Imaging of a translucent object hidden in a highly scattering medium from the early portion of the diffuse component of a transmitted ultrafast laser pulse*, Opt. Lett. **17**, 958 (1992).

[14] L. Feng, K.M. Yoo, and R.R. Alfano, *Transmitted photon intensity through biological tissues within various time windows*, Opt. Lett. **19**, 740 (1994).

[15] J.A. Moon and J. Reintjes, *Image resolution by use of multiple scattered light*, Opt. Lett. **19**, 521 (1994).

[16] J.A. Moon, R. Mahon, M.D. Duncan, and J. Reintjes, *Resolution limits for imaging through turbid media with diffuse light*, Opt. Lett. **18**, 1591 (1993).

[17] G. 't Hooft, private communication.

[18] J.H. Li, A.A. Lisyansky, T.D. Cheung, D. Livdan, and A.Z. Genack, *Transmission and surface intensity profiles in random media*, Europhys. Lett. **22**, 675 (1993).

[19] H.C. van de Hulst, 'Multiple scattering of light', Vols. I, II (Academic Press, New York, 1980).

[20] M.P. van Albada, B.A. van Tiggelen, A. Lagendijk, and A. Tip, *Speed of propagation of classical waves in strongly scattering media*, Phys. Rev. Lett. **66**, 3132 (1991).

Chapter 7

Location of objects in multiply scattering media

7.1 Introduction

In this chapter, we will consider imaging through multiply scattering media. We will investigate what information of an object to be imaged is still present in the multiply scattered light, and how it is possible to extract this information from the multiply scattered light. The usefulness of this study is quite clear for anyone who got lost on a foggy day. Perhaps a less expected, but far more important application is imaging through (human) tissues. The key issue here is to have a completely harmless, non-invasive imaging technique. Blood is usually red, hence it absorbs strongly in the green. For red or near infra-red light, absorption is less important, but the more is (multiple) scattering of the light by (blood) cells and different tissue layers. Issues of medical interest are for instance, detection of breast tumour cells. Tumour tissue often has a higher vascularization, which makes it absorb more in the red or near infra-red. Another example is mapping of the entire blood system of a patient. Nowadays, the map is created with the help of an intravenous contrast fluid. Besides some strange sensation in the patient, it may also endanger her/his life. It is clear that measurements with light are important tools for medical care. Understanding multiple scattering of light is crucial to interpret these measurements and to create clinically applicable apparatuses.

Many researchers have been attracted by imaging problems.[1]-[9] As a first step towards solving the problem of imaging, one tries to reduce the multiply scattered light contribution to the image either by making the media absorb, or by filtering out the non-scattered light with the help of femtosecond light pulses and ultrafast detection methods,[4]-[6]. Absorbing dye affects the long paths the most, so only the shortest paths, containing unblurred information of the object, come through. When the non-scattered light is detected, one obtains a shadow of the hidden object.

One also tries to obtain information from the first transmitted light of a short light pulse. In literature this is known as detecting the 'snake-like photons'.[7] This first arriving light has crossed the system almost in a straight line, and thus carries unblurred information of the hidden object. In the previous chapter we have studied the time resolved transmission by numerical simulations. The fact that the scattering in biological tissue is predominantly in the forward direction turns out to be crucial for this method to work.

Besides the impractical large and complicated apparatuses, (generation of ultra short laser pulses, sophisticated time-windowed raman-gain amplifiers, kerr-gating etc.) these techniques only detect the low order of scattered light, and thus put a severe limit on the probing depth. In state-of-the-art experiment, it is possible to filter out the unscattered beam through a sample that is 33 mean free paths thick. That means detecting a signal 10^{-15} on a background of 0.01[5] However, being able to see through 33 mean-free paths is not sufficiently powerful for real applications that require an observation depth ten to hundred times larger. If one wants to enlarge this probing depth, one should measure the *diffuse* intensity (i.e., the multiply scattered light).

We approach the problem of imaging through multiply scattering media by investigating the *diffuse* light. We will calculate the disturbance on the diffuse intensity for an object small compared to the system size (the surrounding scattering medium wherein the object is placed). To characterize the object we introduce a size s and an absorption length L_a. An absorption parameter α accounts for absorption at the surface of the object. The diffusion constant *inside* the object differs from the diffusion constant of the surrounding medium. In this way non-absorbent or scattering objects can also be treated.

The important parameter for the visibility of an object turns out to be the ratio s/L, L being the characterizing dimension of the system wherein the object has been placed. The local intensity disturbance due to the object is *diffusively broadened*, therefore the visibility is independent of the scattering mean-free path.

This chapter is organized as follows. In section 7.2 we present general ideas on how to calculate the disturbance of an object on the diffuse intensity using diffusion theory. In section 7.2.1 we calculate explicitly the transmitted and reflected intensity for a slab. We compare our diffusion results with a diagrammatic approach in section 7.2.2. In section 7.2.3 we derive relevant formulae for the experimental situation; a slab-like scattering system with a translationally invariant object in one direction. This system behaves in essence two dimensionally. We will call this system a 'two dimensional slab'. In section 7.2.4 the disturbance on the diffuse intensity is calculated when a point, or line source, is used instead of a plane wave. A spherical geometry is considered in section 7.2.5. Measurements were carried out for a 'two-dimensional slab' to test the theory. We report, in section 7.3, on our experimental results, which are in good agreement with diffusion theory.

7.2 Calculation of the diffuse intensity

For the transport of light through the scattering medium and *through* the object we use the diffusion approximation, and we take smooth boundaries for the medium and for the object. We consider a spherical object with a radius s. Our goal is to solve the stationary diffusion equation with boundary conditions given by the geometry of the scattering medium and extra boundary conditions at the surface of the embedded object. The logical procedure is to solve first the diffusion equation for light inside and outside the object. Afterwards, the two solutions can be glued together using the boundary conditions at the surface of the object.

In this chapter, we will neglect internal reflections and corrections of the skin layer, as they tend to enlarge the formulae and diminish the clarity of the approach. A correct treatment of the boundaries is possible, but it gains no deeper insight into the imaging problem. Errors introduced by neglecting the skin layer and internal reflectivity will be small when the mean-free path l_{tr} is much smaller than the object, and the object much smaller than the scattering medium. In the experiment, the effective index of refraction of the scattering medium should be close to that of the container.

The mathematical boundaries of the system are set at the physical boundaries. Doing this, the transmitted and reflected light intensity should be defined as the normal derivative at the boundaries of the scattering medium; the outgoing flux.

The slab is situated between $z = 0$ and $z = L$ and is infinitely extended in the xy-plane. The spherical geometry that confines a scattering medium is centered at the origin, and has radius R. Light described by a source term $S(x, y)$, plane wave or point like, enters at $z = 0$ for the slab and at $z = R$ for the sphere. The object will be located at $(0, 0, z_0)$. Thus, z_0 is not the extrapolation length as it was in previous chapters. In the present chapter we neglect the extrapolation length and z_0 will evidently be the z-position of the object.
The stationary diffusion equation reads, with $I(\mathbf{r})$ the diffuse intensity

$$\Delta I(\mathbf{r}) = 0. \tag{7.1}$$

The boundary conditions at the outer surfaces of the scattering medium are thus taken to be, for a slab

$$I(x,y,0) = S(x,y), \quad I(x,y,L) = 0, \tag{7.2}$$

and for a sphere

$$I(R,\theta,\phi) = S(\theta,\phi). \tag{7.3}$$

One can distinguish at least two types of absorption by the object: uniform absorption in its volume or absorption only at its surface. Absorption at the surface could be used, for instance, as a model for dyed polystyrene spheres. For uniform absorption an absorption length $L_a \equiv 1/\kappa$, (see Chapter 2), can be introduced, and for the intensity *inside* the object the diffusion equation

$$\Delta I(\mathbf{r}) = \kappa^2 I(\mathbf{r}), \tag{7.4}$$

should be considered. In this case the problem is to solve Eq. (7.1) and Eq. (7.4), together with the boundary condition (7.2) or (7.3) and with extra boundary conditions on the surface of the object that are given by

$$I_{out}(s^+) = I_{in}(s^-), \tag{7.5}$$

$$D_1 \left.\frac{\partial I_{out}}{\partial n}\right|_{s^+} = D_2 \left.\frac{\partial I_{in}}{\partial n}\right|_{s^-}. \tag{7.6}$$

The diffusion constants D_1 and D_2 are for the medium and the interior of the object respectively. The normal derivative $\partial/\partial n$ is taken outwards on the surface of the object. Equation (7.5) provides continuity of intensity, and Eq. (7.6) conserves the flux through the surface of the object.

To account only for absorption at the surface of the object, one modifies Eq. (7.6) such that the flux through the surface is not conserved, and use Eq. (7.1) for the intensity inside the object. The modified boundary conditions are

$$I_{out}(s^+) = I_{in}(s^-), \tag{7.7}$$

$$D_1 \left.\frac{\partial I_{out}}{\partial n}\right|_{s^+} = D_2 \left.\frac{\partial I_{in}}{\partial n}\right|_{s^-} + \alpha I_{in}(a). \tag{7.8}$$

The absorption parameter α has the dimension of a speed. We can distinguish a number of relevant cases.

$\alpha = \kappa = 0,\ D_2 \neq D_1$	: pure scatterer, no absorption,
$\alpha = \kappa = 0,\ D_2 = \infty$	: glass object, or air bubble,
$\alpha \neq 0$ and/or $\kappa \neq 0$	: absorber.

Since Eq. (7.1) is a Laplace equation we can use the formalism of electrostatics, and introduce the analog of charges, dipoles and their mirror images. Positive charges describe light sources, negative sources describe absorption of light. Dipoles describe scattering objects.

Translating the imaging problem to an electrostatic problem, we are faced with: a dielectric medium bound by conductors at different potentials (the scattering medium with diffusion constant D_1 and incoming light), with a small charged region with a different dielectric constant (the object). The question now is to calculate the electric field inside the conductors. The object is small compared to the system, hence the disturbance by the object on the intensity can be expressed in a multipole expansion. The first multipole is a charge or source term. It describes the intensity at r due to a point source located at r_0. This is, by definition, the intensity Green's function for the system considered. If one describes multiple scattering of light, it is usually called the diffusion propagator. The diffusion propagator in a slab is found by applying the boundary condition (7.2) (with $S(y,z)=0$) to the solution of the diffusion equation with a delta functions source term. This results in summation over mirror images. Expressions for the next and higher multipoles can easily be obtained from the expression for the charge term by taking successive derivatives with respect to the position of the charge.

7.2.1 Three-dimensional slab

In this subsection we will calculate explicitly the disturbance on the light intensity for the three dimensional situation. The slab is illuminated by a plane wave from the negative z-direction. A spherical object with radius s is located at $\mathbf{r}_0 = (0,0,z_0)$. A schematic view is given in Fig. 1. The intensity in the slab can be expressed as

$$\begin{aligned} I(\mathbf{r}) &= I_0\frac{L-z}{L} - qI_0\sum_{n=-\infty}^{\infty}\frac{1}{|\mathbf{r}-\mathbf{r}_0+2Ln\hat{z}|} - \frac{1}{|\mathbf{r}+\mathbf{r}_0+2Ln\hat{z}|} \\ &\quad -pI_0\sum_{n=-\infty}^{\infty}\frac{z-z_0+2nL}{((z-z_0+2nL)^2+\rho^2)^{\frac{3}{2}}} + \frac{z+z_0+2nL}{((z+z_0+2nL)^2+\rho^2)^{\frac{3}{2}}}, \end{aligned} \tag{7.9}$$

$$\hat{z} \equiv \text{ unit vector along the z-axis, and } \rho^2 \equiv x^2+y^2.$$

The first term in Eq. (7.9) describes the undisturbed intensity, the second term represents the effect of absorption analogous to a charge in electrodynamics and the third is the dipole term due to scattering. Further details of the object will be found back in higher multipoles for the intensity, but their contribution to the disturbance far away from the object will be small. When $s \ll L$, it is sufficient to retain only the first two multipoles.

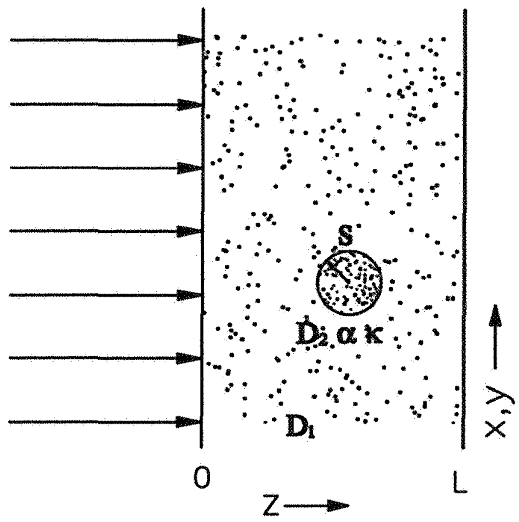

Figure 1: A schematic view of a multiply scattering system with an embedded spherical object. The scattering system is characterized by a diffusion constant D_1, the object by radius s, diffusion constant D_2, absorption parameter α, and inverse absorption length κ. A plane wave is incident at $z = 0$, the intensity is derived at $z = 0$ and $z = L$.

The Ansatz for the intensity inside the object depends on whether we take uniform absorption or absorption only at the boundary of the object. When we introduce an absorption length L_a, the Ansatz for the intensity inside the object is given by the first two spherical Bessel functions with imaginary arguments

$$I_{in}(\mathbf{r}) = I_0 A \frac{\sinh \kappa r}{\kappa r} - I_0 \frac{3B}{\kappa}\left(\frac{\sinh \kappa r}{\kappa^2 r^2} - \frac{\cosh \kappa r}{\kappa r}\right) \cos \theta. \tag{7.10}$$

Note that θ is the angle between $\mathbf{r}$ and the z-axis.

If the object absorbs only at its boundary, we can take the intensity inside the object in leading order to be a linear solution of the diffusion equation

$$I_{in}(\mathbf{r}) = I_0 A + I_0 B (z - z_0). \tag{7.11}$$

For small κ Eq. (7.10) shows similar behaviour

$$\lim_{\kappa \to 0} I_{in}(\mathbf{r}) = A + \left(\frac{-3B}{\kappa}\right)\left(\frac{-\kappa r}{3}\right)\left(\frac{z - z_0}{r}\right). \tag{7.12}$$

Most general is to allow both absorptions mechanisms, uniform and absorption at the surface. The Ansatz is given by Eq. (7.10) and the boundary conditions at the surface of the sphere by Eq. (7.7) and Eq. (7.8).

When Eq. (7.9) is approximated for $\mathbf{r}$ close to $\mathbf{z}_0$, it reduces to

$$I(\mathbf{r}) \approx I_0 \frac{(L-z_0)-(z-z_0)}{L} - qI_0\left[\frac{1}{|\mathbf{r}-\mathbf{r}_0|} + O(\frac{s}{L})\right] - pI_0\left[\frac{z-z_0}{|\mathbf{r}-\mathbf{r}_0|^3} + O(\frac{s}{L})\right]. \tag{7.13}$$

A straightforward calculation gives the coefficients

$$\begin{aligned}
q &= (L-z_0)\frac{s}{L}\frac{D_2(\cosh\kappa s - \mathrm{sinhc}\kappa s)/\mathrm{sinhc}\kappa s + \alpha s}{D_1 + D_2(\cosh\kappa s - \mathrm{sinhc}\kappa s)/\mathrm{sinhc}\kappa s + \alpha s}, \\
p &= \frac{s^3}{L}\frac{D_1 - D_2(2\cosh\kappa s - 2\mathrm{sinhc}\kappa s - \kappa s\sinh\kappa s)/(\mathrm{sinhc}\kappa s - \cosh\kappa s) - \alpha s}{2D_1 + D_2(2\cosh\kappa s - 2\mathrm{sinhc}\kappa s - \kappa s\sinh\kappa s)/(\mathrm{sinhc}\kappa s - \cosh\kappa s) + \alpha s}, \\
A &= -\frac{D_1 q}{\alpha s^2\mathrm{sinhc}\kappa s + sD_2(\cosh\kappa s - \mathrm{sinhc}\kappa s)}, \\
B &= -\frac{1}{3}\frac{\kappa^2 s^2}{\mathrm{sinhc}\kappa s - \cosh\kappa s}(\frac{1}{L} + \frac{p}{s^3}),
\end{aligned} \tag{7.14}$$

with $\mathrm{sinhc}x \equiv \sinh(x)/x$. Practicable formulae are found for κ small. The expressions in Eq. 7.14 reduce to

$$\begin{aligned}
q &= (L-z_0)\frac{s}{L}\frac{1}{1 + D_1/\alpha s}, \\
p &= \frac{s^3}{L}\frac{D_1 - D_2 - \alpha s}{2D_1 + D_2 + \alpha s}, \\
A &= -\frac{D_1 q}{\alpha s^2}, \\
B &= -\frac{1}{L} - p\frac{1}{s^3}.
\end{aligned} \tag{7.15}$$

The transmitted intensity as a function of the transversal distance to the object is given by

$$\begin{aligned}
T(\rho) &\equiv -\frac{l_{tr}}{I_0}\frac{\partial I}{\partial z}\bigg|_{z=L}, \\
&= \frac{l_{tr}}{L} + 2ql_{tr}\sum_{n=-\infty}^{\infty}\frac{z_0 + (2n+1)L}{((z_0 + (2n+1)L)^2 + \rho^2)^{\frac{3}{2}}} \\
&\quad + 2pl_{tr}\sum_{n=-\infty}^{\infty}\frac{\rho^2 - 2(z_0 + (2n+1)L)^2}{((z_0 + (2n+1)L)^2 + \rho^2)^{\frac{5}{2}}}.
\end{aligned} \tag{7.16}$$

and the reflected intensity by

$$\begin{aligned}
B(\rho) &\equiv 1 + \frac{l_{tr}}{I_0}\frac{\partial I}{\partial z}\bigg|_{z=0}, \\
&= 1 - \frac{l_{tr}}{L} - 2ql_{tr}\sum_{n=-\infty}^{\infty}\frac{z_0 + 2nL}{((z_0 + 2nL)^2 + \rho^2)^{\frac{3}{2}}} \\
&\quad - 2pl_{tr}\sum_{n=-\infty}^{\infty}\frac{\rho^2 - 2(z_0 + 2nL)^2}{((z_0 + 2nL)^2 + \rho^2)^{\frac{5}{2}}},
\end{aligned} \tag{7.17}$$

Note that both sums in Eq. (7.16) and the second one in Eq. (7.17) are negative. When the object does not absorb (α=0 and κ=0) only the dipole term in Eq. (7.16) and Eq. (7.17) is present. When for instance $D_2 \gg D_1$, there will be a local increased transmission and a decreased reflection. The peak height relative to background, is of the order s^3/L^3. For absorbent objects, we usually have $s\alpha \gg D_1 s^2/L^2$, ($s \ll L$) in which case the charge term dominates with strength s/L. Since there is absorption the transmission and reflection will be reduced locally. Furthermore, from Eq. (7.16) and Eq. (7.17) we see that when the object is located in the middle of the slab, the absolute strength of the disturbance on the reflected and transmitted intensity is equal, but in transmission it is more pronounced since it is superimposed on a much lower background.

7.2.2 Diagrammatic approach

The research described in this chapter was initiated by a theoretical paper by Berkovits and Feng.[8]. Berkovits and Feng calculated the transmission of a system consisting of N moving non-absorbent point scatterers and one extra static scatterer *identical* to the moving ones. Berkovits and Feng used a diagrammatic approach, ladder diagrams, in their calculation. They found the static point scatterer to cause a locally increased transmission. This provides the possibility of locating the point scatterer.

Ladder diagrams describe propagation of the diffuse intensity in the scattering medium. The calculation of the effect of one static point scatterer on the diffuse intensity can be rephrased on a diagrammatic level to: how to attach the arriving and leaving ladder diagrams to the static scatterer?

Because the answer is elegant and of fundamental interest, we will review this derivation. We start with the result of Berkovits and Feng and shortly discuss the problems with their outcome. We proceed by following Nieuwenhuizen and Van Rossum[10] and compare the diagrammatic approach with the diffusion approach explored in the previous section. Berkovits and Feng.[8] used the following diagrams

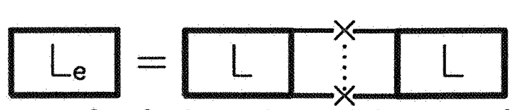

(7.18)

These diagrams account for the intensity arriving at and leaving from the particle. However, after integrating the position of the static scatterer over the whole volume of the slab, energy is found to have been created. A higher transmission and reflection is found than direct calculation for a system consisting of n+1 point scatterers. In Ref. [8] this extra intensity has been subtracted by hand. As a result a static particle appears to act as a light source.

What has been overlooked, or what is wrong with the diagram depicted in Eq. (7.18)? The answer is logical and found in the derivation of the ladder diagrams[10]. In a ladder diagram every thick solid line represents a summation over all possible scattering events of the amplitude to arrive from one particle at the next particle, see Chapter 2. However, this extra static particle should participate independently in the upper and lower line of the coupling Green's functions between the ladder diagrams. According to ref. [10], we get in leading order, 4 extra diagrams:

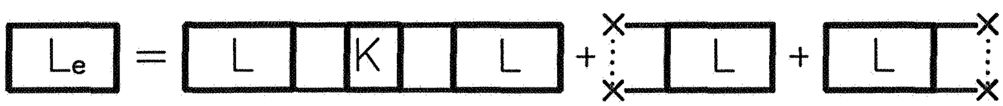

(7.19)

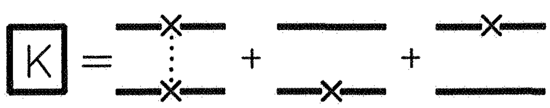

(7.20)

These extra diagrams in Eq. (7.20) turn out to be of great importance, since they interfere destructively with the diagram of Eq. (7.18). Hence, the leading contribution of this diagram is cancelled. With these extra diagrams the problem of the creating of energy is automatically solved.
We find for the coupling diagrams K:

$$\begin{aligned}
K_1 &= |t_0|^2 \int d^3p G(\mathbf{p}+\frac{1}{2}\mathbf{q}_1)G^*(\mathbf{p}-\frac{1}{2}\mathbf{q}_1) \int d^3p' G(\mathbf{p}'-\frac{1}{2}\mathbf{q}_1)G^*(\mathbf{p}'+\frac{1}{2}\mathbf{q}_2) \\
&\approx |t_0|^2 \frac{l_{tr}^2}{16\pi^2}\{1-\frac{1}{3}(q_1^2+q_2^2)l_{tr}^2 - 2(1-a)\} \\
K_2 &= t_0 \int d^3p G^*(\mathbf{p})G(\mathbf{p}+\mathbf{q}_1)G(\mathbf{p}-\mathbf{q}_1) \\
&\approx -\frac{it_0 l_{tr}^2}{8\pi k_0}\{-1+\frac{1}{3}(q_1^2+q_2^2-\mathbf{q}_1\cdot\mathbf{q}_2)l_{tr}^2 - 2(1-a)\} \\
K_3 &= K_2^*
\end{aligned}$$

The extra scatterer has t-matrix t_0 and albedo a_0, different from the embedding scatterers with density n and albedo a and t-matrix t (definitions of the t-matrix and relations to cross sections can be found in Chapter 2). The total sum of the contributions K_1 to K_3 is

$$K = -\frac{|t_0|^2 l_{tr}^2}{48\pi^2}\{\mathbf{q}_1\cdot\mathbf{q}_2 l_{tr}^2 + 3(1-a_0)\}. \tag{7.21}$$

The expression for the two connected lader diagrams in space-coordinates is

$$L_e(\mathbf{r},\mathbf{r}') = L(\mathbf{r},\mathbf{r}') + \frac{n_0|t_0|^2}{n|t|^2}\{\delta(\mathbf{r}'-\mathbf{r}_0)+\delta(\mathbf{r}-\mathbf{r}_0)\}L(\mathbf{r},\mathbf{r}')$$

$$
\begin{aligned}
&+\frac{|t_0|^2 l_{tr}^2}{48\pi^2}\int d\mathbf{r}_1 d\mathbf{r}_2\{l^2\nabla_1\cdot\nabla_2 - 3(1-a_0)\}\times \\
&L(\mathbf{r},\mathbf{r}_1)L(\mathbf{r}_2,\mathbf{r}')\delta(\mathbf{r}_1-\mathbf{r}_0)\delta(\mathbf{r}_2-\mathbf{r}_0). \qquad (7.22)
\end{aligned}
$$

Averaging over the position of the extra particle now gives the correct result, i.e. diffusive propagation. Calculating the transmission and reflection for the slab with a static particle, leads to the same expressions as is in previous subsection. The charge and dipole strength are given by:

$$
\begin{aligned}
q_d &= \frac{L-z_0}{L}\frac{3|t_0|^2}{16\pi^2 l_{tr}}(1-a_0) \\
p_d &= \frac{l_{tr}|t_0|^2}{L16\pi^2} \qquad (7.23)
\end{aligned}
$$

The second and third diagram of Eq. (7.19) has been neglected, they only contribute when the extra scatter is near the boundary.

To compare both approaches we put an imaginary sphere with arbitrary radius R_s around the static particle. The diffusion constant in this sphere is $D_2 = vl_e/3$ with $l_e = 4\pi/(n|t|^2+n_0|t_0|^2)$, and $n_0 = 3/4\pi R_s^3$. The inverse absorption length in this sphere is $\kappa = ((3n|t|^2(1-a) + 3n_0|t_0|^2(1-a_0))/4\pi l_{tr})^{1/2}$. The extra absorption by the static particle will be small, and $D_2 \approx D_1$. In the same limits the expression for q, Eq. (7.14) of section 7.2.1, reduces to

$$
\begin{aligned}
q &= \frac{L-z_0}{3L}\kappa^2 R_s^3, \\
&\quad \kappa^2 = 3\frac{n|t|^2(1-a)+n_0|t_0|^2(1-a_0)}{l_e} \approx 3\frac{n_0|t_0|^2}{4\pi l_{tr}}(1-a_0) \\
q &\approx \frac{(L-z_0)R_s^3}{3L}\frac{3\frac{3}{4\pi R_s^3}|t_0|^2(1-a_0)}{4\pi l_{tr}} \\
&= \frac{L-z_0}{L}\frac{3|t_0|^2}{16\pi^2 l_{tr}}(1-a_0),
\end{aligned}
$$

and p reduces to

$$
p = \frac{R_s^3}{L}\frac{D_1-D_2}{3D_1} \approx \frac{R_s^3}{3L}\frac{n_0|t_0|^2}{n|t|^2} = \frac{l_{tr}R_s^3}{3L}\frac{3|t_0|^2}{4\pi R_s^3 4\pi} = \frac{l_{tr}|t_0|^2}{L16\pi^2}. \qquad (7.24)
$$

Comparing these expressions with the diagrammatic approach we conclude that, within these limits, both approaches give the same result.

7.2.3 Two-dimensional slab

The intensity disturbance in a two-dimensional slab is derived by a completely analogous approach to that of section 7.2.1. Two dimensional systems, or better, translationally invariant systems, provide a convenient experimental situation since cylindrically shapes objects like rods and glass fibers should be used. Rods and fibers can be mounted without disturbing the system.

To obtain the Green's function in a two dimensional system, one applies the first boundary condition, Eq. (7.2) with $S(0,y,z) = 0$ to the potential of a line source. The summation over mirror images, in this case, can be performed exactly. Here it is convenient to introduce the complex variable $\zeta \equiv z + iy$. The potential for a line dipole can again be found by taking the derivative of this result with respect to the position. The Ansatz for the solution of the diffusion equation, Eq. (7.1) with a line charge and a line dipole outside the object, reads

$$\begin{aligned} I_{out}(\zeta) &= I_0 \frac{L-z}{L} - qI_0 \mathrm{Re}\left(\ln \frac{\sin\frac{\pi}{2L}(\zeta - z_0)}{\sin\frac{\pi}{2L}(\zeta + z_0)}\right) \\ &\quad - pI_0 \mathrm{Re}\left(\cot\frac{\pi}{2L}(\zeta - z_0) + \cot\frac{\pi}{2L}(\zeta + z_0)\right), \end{aligned} \tag{7.25}$$

with z_0 the position of the scatterer, ($y_0 = 0$). Re$\{x\}$ denotes the real part of x. For absorption at the boundary only, the Ansatz is

$$I_{in}(\zeta) = I_0 A + I_0 B(z - z_0). \tag{7.26}$$

For uniform absorption the Ansatz for the intensity inside the object is

$$I_{in}(\zeta) = I_0 A \mathrm{I}_0(\kappa\rho) + I_0 \frac{2B}{\kappa} \mathrm{I}_1(\kappa\rho)\cos\phi. \tag{7.27}$$

Here $\mathrm{I}_0(r)$ and $\mathrm{I}_1(r)$ are the modified Bessel functions of order 0 and 1, $\rho = \sqrt{y^2 + z^2}$ and ϕ is the angle between $\vec{\rho}$ and the z-axis.

To obtain the constants q, p, A and B we again approximate Eq. (7.25) for ζ close to z_0, and for s/L small

$$\begin{aligned} I_{out}(\zeta) &= I_0 \frac{(L - z_0) - (z - z_0)}{L} - qI_0 \left[\ln \frac{\pi}{2L} \frac{\sqrt{(z-z_0)^2 + y^2}}{\sin\frac{\pi}{L} z_0} + O(\frac{s^2}{L^2})\right] \\ &\quad - pI_0 \left[\frac{2L(z - z_0)}{\pi((z-z_0)^2 + y^2)} + \cot\frac{\pi}{L} z_0 + O(\frac{s}{L})\right]. \end{aligned} \tag{7.28}$$

Inserting Eqs. (7.26) and (7.28) in Eqs. (7.7) and (7.8), which accounts for uniform absorption and absorption on the surface of the object, gives

$$\begin{aligned} q &= -\left[\frac{L - z_0}{L} + p\cot(\frac{\pi z_0}{L})\right] \frac{\alpha s + D_2 \kappa s \mathrm{I}_1(\kappa s)/\mathrm{I}_0(\kappa s)}{D_1 + (\alpha s + D_2 \kappa s \mathrm{I}_1(\kappa s)/\mathrm{I}_0(\kappa s)) \ln\frac{L}{s^*}}, \\ p &= \frac{\pi s^2}{2L^2} \frac{D_1 - D_2(\kappa s \mathrm{I}_0(\kappa s) - \mathrm{I}_1(\kappa s))/\mathrm{I}_1(\kappa s) - \alpha s}{D_1 + D_2(\kappa s \mathrm{I}_0(\kappa s) - \mathrm{I}_1(\kappa s))/\mathrm{I}_1(\kappa s) + \alpha s}, \\ A &= -\frac{\mathrm{I}_0(\kappa s)}{\kappa s \mathrm{I}_1(\kappa s) D_2 + \mathrm{I}_0(\kappa s)\alpha s} D_1 q, \\ B &= -\frac{\kappa s}{2\mathrm{I}_1(\kappa s)}(\frac{1}{L} + p\frac{2L}{\pi s^2}), \end{aligned} \tag{7.29}$$

with the rescaled radius

$$s^* = \frac{\pi s}{2\sin\frac{\pi z_0}{L}}. \tag{7.30}$$

Although the dipole term depends separately on α and κ, we take $\kappa = 0$ from now on. This simplification is justified because the dipole contribution to the intensity disturbance can be neglected whenever absorption is present. One may conclude that the intensity disturbance far outside the object does not depend dramatically on the details of the absorption mechanism. For $\kappa = 0$, the coefficients reduce to

$$\begin{aligned}
q &= -\left[\frac{L - z_0}{L} + \cot\left(\frac{\pi z_0}{L}\right)\frac{D_1 - D_2 - \alpha s}{D_1 + D_2 + \alpha s}\frac{\pi s^2}{2L^2}\right]\frac{\alpha s}{D_1 + \alpha s \ln\frac{L}{s^*}}, \\
p &= \frac{\pi s^2}{2L^2}\frac{D_1 - D_2 - \alpha s}{D_1 + D_2 + \alpha s}, \\
A &= -\frac{D_1 q}{\alpha s}, \\
B &= -\frac{1}{L} - p\frac{2L}{\pi s^2}.
\end{aligned} \tag{7.31}$$

When $\alpha s > D_1 s^2/L^2$, the charge term dominates and has strength $(ln(L/s^*) + D_1/\alpha s)^{-1}$. We obtain for the transmitted light

$$\begin{aligned}
T(y) &\equiv -\frac{l_{tr}}{I_0}\frac{\partial I(\mathbf{r})}{\partial z}\bigg|_{z=L}, \\
&= \frac{l_{tr}}{L}\left[1 + q\frac{\pi\sin\frac{\pi z_0}{L}}{\cosh\frac{\pi y}{L} + \cos\frac{\pi z_0}{L}} - 2\pi p\frac{1 + \cosh\frac{\pi y}{L}\cos\frac{\pi z_0}{L}}{(\cosh\frac{\pi y}{L} + \cos\frac{\pi z_0}{L})^2}\right],
\end{aligned} \tag{7.32}$$

and for the reflected light

$$\begin{aligned}
B(y) &\equiv 1 - \frac{l_{tr}}{I_0}\frac{\partial I(\mathbf{r})}{\partial z}\bigg|_{z=0}, \\
&= 1 - \frac{l_{tr}}{L}\left[1 - q\frac{\pi\sin\frac{\pi z_0}{L}}{\cosh\frac{\pi y}{L} - \cos\frac{\pi z_0}{L}} - 2\pi p\frac{1 - \cosh\frac{\pi y}{L}\cos\frac{\pi z_0}{L}}{(\cosh\frac{\pi y}{L} - \cos\frac{\pi z_0}{L})^2}\right]
\end{aligned} \tag{7.33}$$

A few examples are plotted in Fig. 2 for different positions and absorption coefficients.

7.2.4 Point source

It is often more convenient to use a point source instead of a plane wave, also the quality of the image can be improved when the response of the system to a point source is known.[11]

First the intensity distribution in the slab should be known if light enters in a point at the boundary of the slab. We make again the assumption that all the

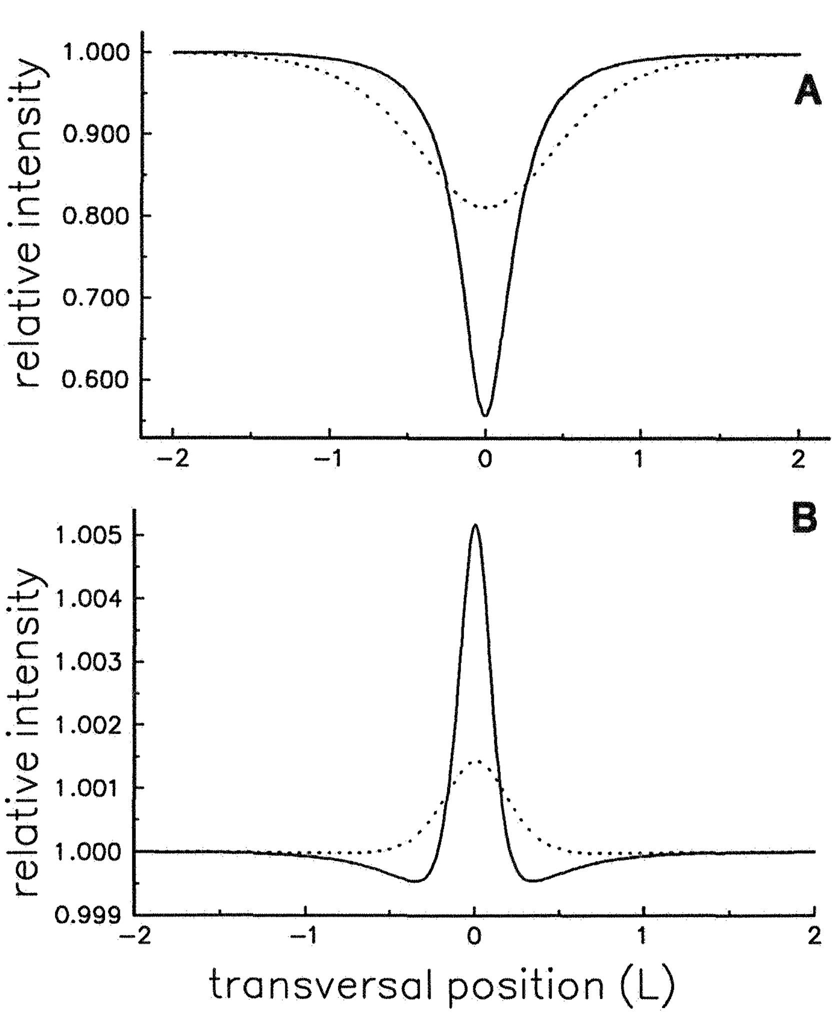

Figure 2: Transmitted intensity as a function of the transversal distance to the object, Eq. (7.33). Plot A: absorbent rod: $s = 0.01L$, $\alpha = \infty$, $\kappa = 0$. Full line: z_0=0.8L, dotted line: $z_0 = 0.2L$. Plot B: scattering rod: $s = 0.01L$, $\alpha = \kappa = 0$, $D_2 = \infty$. Full line: $z_0 = 0.8L$, dotted line: z_0=0.6L.

incoming light starts to propagate diffusely at a depth of one transport mean-free path inside the slab.[12] Without an object, the intensity distribution inside the slab is thus given for a two dimensional system by

$$P_2(\mathbf{l}_{tr}, \zeta) = \mathrm{Re}\left(\ln \frac{\sin \frac{\pi}{2L}(\zeta - \mathbf{l}_{tr})}{\sin \frac{\pi}{2L}(\zeta + \mathbf{l}_{tr})}\right), \tag{7.34}$$

with $\mathbf{l}_{tr} \equiv (0i, l_{tr})$, and for a three dimensional system by

$$P_3(\mathbf{l}_{tr}, \mathbf{r}) = \sum_{n=-\infty}^{\infty} \frac{1}{|\mathbf{l}_{tr} - \mathbf{r} + 2Ln\hat{z}|} - \frac{1}{|\mathbf{l}_{tr} + \mathbf{r} + 2Ln\hat{z}|} \tag{7.35}$$

with $\mathbf{l}_{tr} \equiv (0, 0, \mathbf{l}_{tr})$. As a consequence of using a point source, the Ansatz for the solution of the total problem, medium plus object, will change. One should realize that the direction of the dipole depends on the local light flux. The direction of the flux at a particular point is now a function of position because a point source is used. The new Ansatz in two dimensions reads

$$\begin{aligned} I_{out}(\zeta) &= I_0 P(\mathbf{l}_{tr}, \zeta) - q I_0 \mathrm{Re}\left(\ln \frac{\sin \frac{\pi}{2L}(\zeta - z_0 - iy_0)}{\sin \frac{\pi}{2L}(\zeta + z_0 + iy_0)}\right) \\ &\quad - p I_0 \mathrm{Re}\left(\xi \cot \frac{\pi}{2L}(\zeta - z_0 + iy_0) + \xi^* \cot \frac{\pi}{2L}(\zeta + z_0 - iy_0)\right), \end{aligned} \tag{7.36}$$

with

$$\xi \equiv \xi_z(y_0, z_0) + i\xi_y(y_0, z_0). \tag{7.37}$$

The coefficients $\xi_z(y_0, z_0)$ and $\xi_y(y_0, z_0)$ follow from a first-order Taylor expansion of the local intensity giving the direction of the dipole

$$\begin{aligned} \xi_z(y_0, z_0) &= \frac{\sin \frac{\pi}{L}(z_0 - l_{tr})}{\cosh \frac{\pi}{L} y_0 - \cos \frac{\pi}{L}(z_0 - l_{tr})} - \frac{\sin \frac{\pi}{L}(z_0 + l_{tr})}{\cosh \frac{\pi}{L} y_0 - \cos \frac{\pi}{L}(z_0 + l_{tr})}, \\ \xi_y(y_0, z_0) &= \frac{\sinh \frac{\pi}{L} y_0}{\cosh \frac{\pi}{L} y_0 - \cos \frac{\pi}{L}(z_0 - l_{tr})} - \frac{\sinh \frac{\pi}{L} y_0}{\cosh \frac{\pi}{L} y_0 - \cos \frac{\pi}{L}(z_0 - l_{tr})}. \end{aligned} \tag{7.38}$$

Also the intensity inside the object should be adjusted to the local flux direction

$$I_{in} = I_0 A + I_0 B\left(\xi_z(y_0, z_0)(z - z_0) + \xi_y(y_0, z_0)(y - y_0)\right). \tag{7.39}$$

Now a straightforward calculation can be performed to obtain the coefficients q, p, A, B. They are

$$\begin{aligned} q &= -\left[P_2(\mathbf{l}_{tr}, \zeta_0) + p\xi_y(y_0, z_0) \cot \frac{\pi z_0}{L}\right] \frac{\alpha s}{D_1 + \alpha s \ln(L/s^*)}, \\ p &= \frac{\pi^2 s^2}{2L^2} \frac{D_1 - D_2 - \alpha s}{D_1 + D_2 + \alpha s}, \\ A &= -D_1 q / \alpha s, \\ B &= \frac{\pi}{2L} \frac{2D_1}{D_1 + D_2 + \alpha s}. \end{aligned} \tag{7.40}$$

In three dimensions the new Ansatz reads

$$I_{out}(\mathbf{r}) = I_0 P_3(\mathbf{l}_{tr}, \mathbf{r}) - q I_0 P_3(\mathbf{r}_0, \mathbf{r}) - p I_0 \left.\frac{\partial}{\partial \mathbf{r}}\right|_{\mathbf{r}=\mathbf{r}_0} P_3(\mathbf{l}_{tr}, \mathbf{r}) \cdot \nabla_{\mathbf{r}_0} P_3(\mathbf{r}_0, \mathbf{r}), \tag{7.41}$$

$$I_{in}(\mathbf{r}) = I_0 A + I_0 B (\mathbf{r} - \mathbf{r}_0) \cdot \left.\frac{\partial}{\partial \mathbf{r}}\right|_{\mathbf{r}=\mathbf{r}_0} P_3(\mathbf{l}_{tr}, \mathbf{r}). \tag{7.42}$$

The coefficients q, p, A and B again follow from the boundary conditions (7.7) and

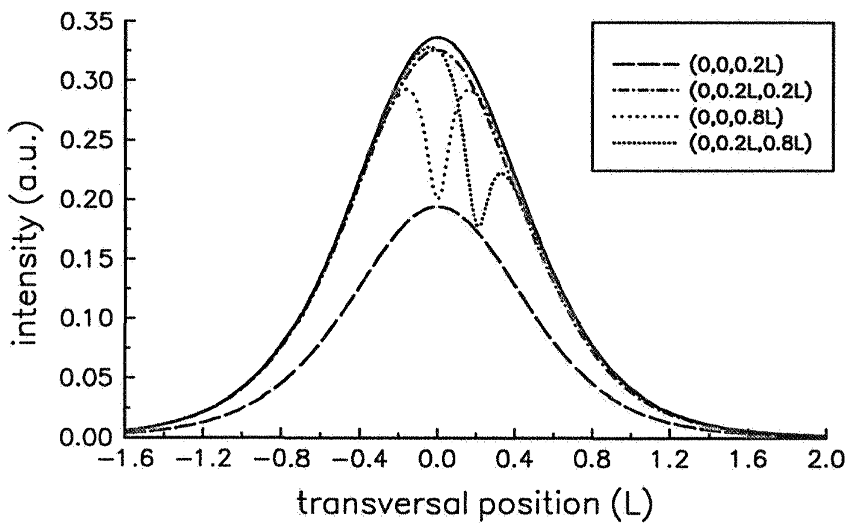

Figure 3: Transmitted intensity profiles of a slab containing an absorbent object at various positions, Eq.(7.16). The light source at $\mathbf{r} = (0, 0, 0.02L)$, is point-like. Radius object s=0.02L, $\alpha = \infty$, $p = 0$. Full line: no object present. Other lines: object at position (x,y,z) as indicated in legend.

(7.8). This results in

$$\begin{aligned}
q &= AP_3(\mathbf{l}_{tr}, \mathbf{r}_0)\frac{\alpha s}{D_1 + \alpha s}, \\
p &= s^3\frac{D_1 - D_2 - \alpha s}{2D_1 + D_2 + \alpha s}, \\
A &= -\frac{D_1 q}{\alpha s^2}, \\
B &= \frac{3D_1}{2D_1 + D_2 + \alpha s}.
\end{aligned} \tag{7.43}$$

The disturbance on the intensity depends strongly on the position of the light source. The disturbance can be more pronounced than for plane wave incidence, depending on the relative orientation of object and light source. This is a more convenient situation because now a displacement of the source can give either a 'background' measurement (without an object) or a measurement with an object. A few examples are plotted in Fig. 3. The transmitted intensity is plotted for various positions of the object with respect to the point source and the boundaries of the slab. The strong dependence of the transmitted intensity on the position of the object is readily seen from the figure.

7.2.5 Spherical geometry

In this section we derive an expression for the light intensity for a spherical medium wherein an object has been placed. The sphere is centered around the origin, light is incident in one point, $Z{=}R$, from the positive z-axis. An expression for the diffusion propagator is readily found when absorption in the embedding medium is absent or negligible. Only one mirror image is needed.[13] Again it is assumed that the incident light propagates diffusively at one transport mean-free path beneath the surface. The diffuse light source is thus located at: $\mathbf{r}_s = (0, 0, R - l_{tr})$. The intensity inside the sphere of radius R, in the absence of an object, is given by:

$$I(\mathbf{r}) = I_0 P_R(\mathbf{r}_s, \mathbf{r}). \tag{7.44}$$

The intensity Green's function for a sphere is given by

$$P_R(\mathbf{r}_1, \mathbf{r}_2) = \frac{1}{\mid \mathbf{r}_1 - \mathbf{r}_2 \mid} - \frac{R}{r_2} \frac{1}{\mid \mathbf{r}_1 - \frac{R^2}{r_2^2}\mathbf{r}_2 \mid}. \tag{7.45}$$

When an object is placed at $\mathbf{r}_0$ inside the sphere, we can express the intensity as follows

$$I_{out}(\mathbf{r}) = I(\mathbf{r}) - qI_0 P_R(\mathbf{r}_0, \mathbf{r}) - I_0 \mathbf{p} \cdot \nabla_{\mathbf{r}_0} P_R(\mathbf{r}_0, \mathbf{r}). \tag{7.46}$$

Inside the object we use the Ansatz

$$I_{in} = I_0 A + I_0 \mathbf{B} \cdot (\mathbf{r} - \mathbf{r}_0), \tag{7.47}$$

(only absorption at the surface of the object). Using boundary conditions (7.7) and (7.8) we derive for the coefficients

$$\begin{aligned}
q &= s\left[P_R(\mathbf{r}_s, \mathbf{r}_0) - \mathbf{p} \cdot \mathbf{r}_0 \frac{R}{(r_0^2 - R^2)^2}\right] \frac{\alpha s}{D_1 + \alpha s(1 - aR/(r_0^2 - R^2))}, \\
\mathbf{p} &= s^3 \left.\frac{\partial}{\partial \mathbf{r}}\right|_{\mathbf{r}=\mathbf{r}_0} P_R(\mathbf{r}_s, \mathbf{r}) \times \\
&\quad \frac{D_1 - D_2 - \alpha s}{2D_1(1 - \frac{1}{2}s^3R^3/(r_0^2 - R^2)^3) + (D_2 + \alpha s)(1 + s^3R^3/(r_0^2 - R^2)^3)} \\
&\quad -q\mathbf{r}_0 \frac{R}{r_0^2 - R^2} \frac{D_1 + D_2 + \alpha s}{2D_1(1 - \frac{1}{2}s^3R^3/(r_0^2 - R^2)^3) + (D_2 + \alpha s)(1 + s^3R^3/(r_0^2 - R^2)^3)}, \\
A &= \frac{D_1 q}{\alpha s^2}, \\
\mathbf{B} &= -\left.\frac{\partial}{\partial \mathbf{r}}\right|_{\mathbf{r}=\mathbf{r}_0} P_R(\mathbf{r}_s, \mathbf{r}) q\mathbf{r}_0 \frac{R}{(r_0^2 - R^2)^2} + \mathbf{p}\left(\frac{1}{s^3} + \frac{R^3}{(r_0^2 - R^2)^3}\right).
\end{aligned} \tag{7.48}$$

The coefficients q and $\mathbf{p}$ are still to be solved from Eq. (7.48). But the above form allows an easy comparison with the formerly obtained coefficients. The transmission through the surface of the sphere can be found by taking the normal derivative.

Note that when the object is located at the origin of the sphere, the disturbance is spherically symmetric. This is why the bone in your finger does not show up when transluminated, but only the blood vessels.

7.3 Experimental procedure

We have performed several experiments to test the theoretical calculations for the diffuse light intensity. The expected signal strength and possibilities of manipulation of the position of the object lead us to the choice of two dimensional slabs, i.e. the total system, slab and object, is translationally invariant in one direction.

7.3.1 Experimental Setup

We use a 7 mW continuous wave He-Ne-laser, $\lambda = 633\ nm$. The laser beam is spatially filtered and expanded to a radius of approximately 20 cm in order to obtain a flat beam profile. Part of this beam impinges on the cuvette containing the object hidden in the scattering medium. For point source imaging, we focused the beam with a cylindrical lens onto the cell. The line focus should be aligned parallel to the rod. The illuminated side or backside of the medium is imaged position to position onto a one-dimensional diode array. The diode array is 2.5 mm high and 25 mm wide, consisting of 1024 pixels. The pixels have dimensions 2.5 mm by approximately 25 μm. Measurements are corrected for dark current, readout noise, and the sensitivity of the individual diodes. Plane wave experiments were also corrected for the remaining initial beam profile. Integration time, and reading out of the diode array, was computer controlled. Depending on the signal strength, integration times vary from 10 s to 3 min.

The experimental setup for plane wave transmission measurement is shown schematically in Fig. 4. The diode array, drawn vertically in the figure, is in reality placed horizontally, i.e. perpendicular to the rod or fiber.

The distances between the lens and the object-plane b, (back- or frontside of the scattering medium) determines the distance between the lens and the image-plane i (diode array). They should follow the well known image law to create a sharp image

$$\frac{1}{b} + \frac{1}{i} = \frac{1}{F}, \tag{7.49}$$

with F being the focal length of the lens. In the experiment we needed an intensity mask to optimize the positions of the cuvette and the diode array. We used a grating of 8 slits with a slitwidth of 1 mm and equal spacing. The grating was illuminated through a diffusively scattering medium, a piece of paper, and imaged through a window of equal thickness as the windows of the cuvette. Imaging

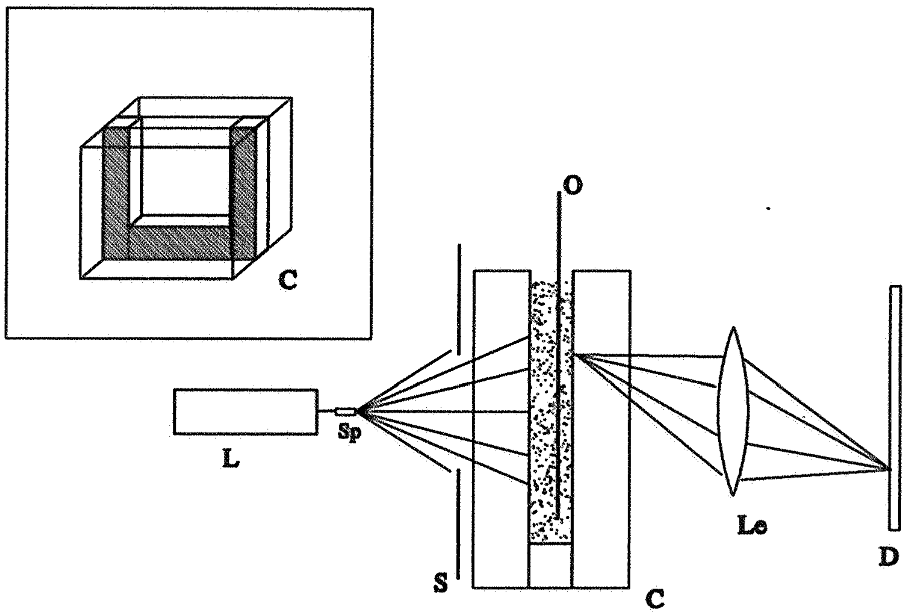

Figure 4: Experimental setup; L: laser, Sp: spatial filter, S: screen, C: cuvette with the scattering medium and the object O. Le: lens for imaging the diffuse intensity on D: the one-dimensional diode array. The inset: front view of the cuvette.

through a window of equal thickness is necessary because an optical flat translates, in first extent, the position of the image or the focus. The grating is also used to determine the magnification of the image and the spatial resolution, which is approximately 60 μm.

Due to the dimensions of the cuvette and diode array, the image is slightly pincushion distorted and the image surface is curved. This results in moderate variation in the spatial resolution over the diode array. Spatial filtering is used to minimize this variation.

7.3.2 Sample container

The thickness of the entrance and exit windows of the cuvette turned out to be very important. Light is totally reflected by the window-air interface when the angle between surface normal and light ray is beyond the critical angle. The reflected light either enters the sample again or is reflected by it. As a consequence, every point source is surrounded by an intense halo of totally internal reflected light. The thickness and the index of refraction of the windows determine the radius of

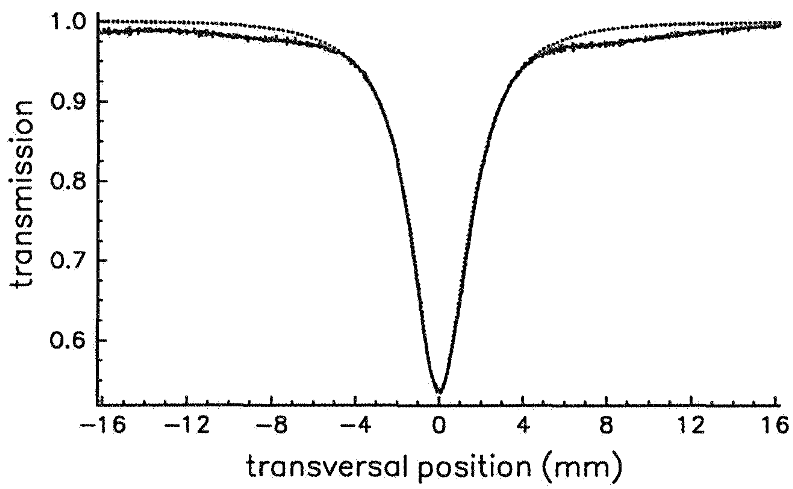

Figure 5: Multiple reflections inside the glass window blur the transmission profile of a slab containing an absorbent rod. Dotted line: theoretically prediction (without multiple reflections).

this halo. As a result, a non-negligible deformation of the intensity profile occurs.

Our first cuvette has an (inner) thickness of 4 *mm* (determining the parameter L), and square windows, 40×40 *mm*, of sufficient thickness, 4 *mm*, to see at least a deformed intensity profile. For windows of only 1 *mm* thick, it would have been very hard to notice any profile in the transmitted light at all.

An example of a deformed intensity profile is plotted in Fig. 5. An absorbent rod is placed in the scattering medium and the transmitted light is recorded. One clearly sees a wedge-shaped background. We could reproduce this deformation by convoluting the calculated profiles with a profile describing the blurring of a point source at the boundary of the slab. The latter is calculated on the basis of specular reflections at the glass-air interface and diffuse reflections at the glass-sample interface.[1] However, incorporating these extra experimental deformations onto the intensity profile, will extend the fitting procedure by the introduction of more parameters. It is therefore not favourable.

We have chosen to reduce the effect of these reflections on the intensity profile by using a cuvette with very thick windows. Now the total internal reflected light is well separated from its source, and in most cases it is reflected adjacent to the sample. In other words: the radius of the halo is larger than the transversal dimensions of the cuvette. (Anti-reflection coating on the windows would not have solved this problem because coating cannot reduce total internal reflection.) Our

[1] In ref. [14] an expression for the Green's functions for a slab with this type of extra boundary conditions is calculated for scalar waves.

second cuvette has square windows of 60×60 *mm* and 20 *mm* (!) thick. The inner thickness is either 5 or 10 *mm*. A front view of the cuvette is shown in Fig. 4. The black 'U'-shape, made of anodized aluminium, absorbs the total internal reflected light.

7.3.3 Scattering Medium

A few experimental conditions should be met. The scattering medium should be a fluid since we want to place objects inside and we want to vary the positions of the objects. The value for the mean-free path of the scattering medium should imply workable sizes for the objects and containers. Constraints on the mean-free path of the scattering medium are forced by the requirements for diffusive light propagation inside the slab, and we do not want to be bothered by boundary corrections, ($l_{tr} \ll L$). This leads to the condition that the thickness of the slab should be at least 100 times the transport mean-free path, which in its turn determines, more or less, the transversal dimension of the slab. The diameters of the rods should be larger than the scattering mean-free path and considerably smaller than the thickness of the slab. The average index of refraction of the scattering medium must be around the value for glass to suppress internal reflection of light escaping the medium, see Chapter 5. Since we are not particularly interested in the smallest size of objects that can still be imaged, but rather in the precise shape of the intensity profile, we used moderately large objects (size object $\approx 0.3\times$ thickness of slab).

Meeting these experimental conditions, the total volume of the scattering medium turned out to be large (30 *ml*). Aqueous-suspensions of mono-disperse latex spheres are commonly used as a scattering medium. Although it does not exhibit experimental problems encountered with other fluids, it is far too expensive to use. Moreover, there is no need for mono-disperse scatterers. The encountered problems were a varying number of particles adhering to the windows which results in a time and position dependent transmission, sedimentation of particles which will increase the transmitted intensity during a measurement, and moving air bubbles which also distort the intensity profile. The best performing scattering medium turned out to be suspended TiO_2-particles in glycerine. Average particle size: 220 *nm*, index of refraction of glycerine: 1.46 at wavelength around 633 *nm*, density of glycerine: 1.26 g/ml. Glycerine is very viscous and thus prevents sedimentation of the TiO_2-particles.

After mixing the TiO_2-particles in glycerine the suspension is placed in a vacuum chamber for several minutes to remove most of the air bubbles that have entered during mixing. We derived the scattering mean-free path of the suspension, by measuring the fraction of unscattered light in transmission, as a function of the

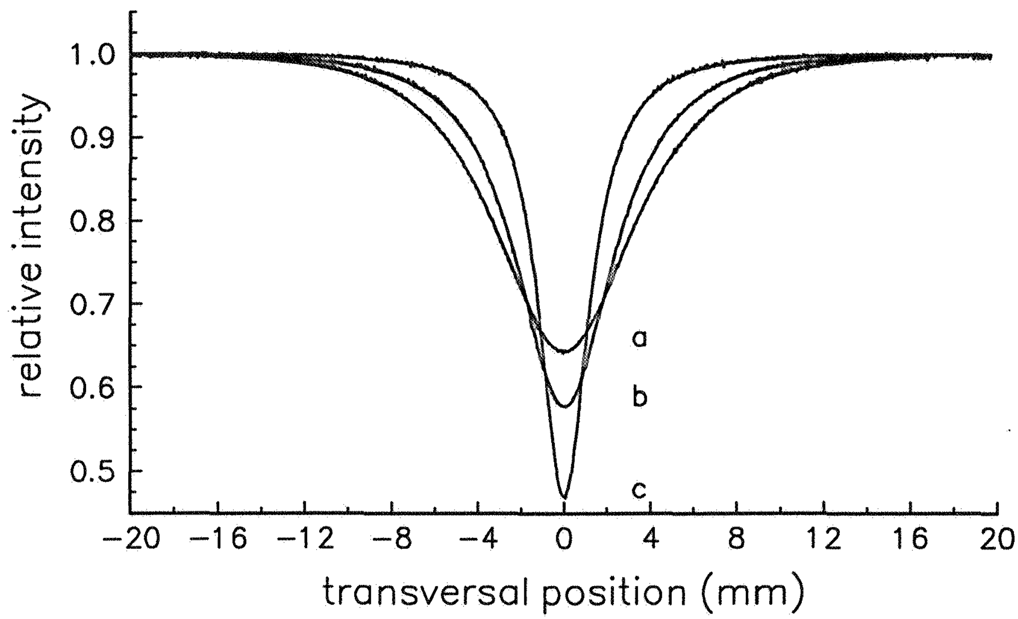

Figure 6: Transmitted intensity for various normal positions of an absorbent rod (s=0.175 mm): a) z_0 = 5.90 mm, b) z_0 = 7.40 mm, c) z_0 = 9.00 mm. The experimental data are shown together with the best numerical fits for Eq. (7.32): a) $z_0 = 5.67 \pm 0.05$ mm, $D_1/\alpha s = 1.11 \pm 0.03$; b) $z_0 = 7.14 \pm 0.05$ mm, $D_1/\alpha s = 1.04 \pm 0.03$; c) $z_0 = 8.39 \pm 0.05$ mm, $D_1/\alpha s = 0.95 \pm 0.03$. For all cases $p = 0$, $l_{tr} = 20 \pm 3$ μm, $L = 10.0$ mm.

thickness of the medium. We calculated the transport mean-free path from the measured scattering mean-free path using Mie theory: $l_{tr} \approx 2l_{sc}$ for these scattering media. Typical values for the transport mean-free paths are in the range 20 μm to 50 μm.

7.4 Experimental results

7.4.1 Transmission measurements

In Fig. 6 we present transmission measurements for absorbent rods. We use a 0.35 mm pencil embedded in a scattering medium having a transport mean-free path of 20 μm. The thickness of the cell is 10.0 mm. The solid curves are the best numerical fits of Eq. (7.32) to the measured profiles. Here the position and the absorption strength are adjustable fit parameters. The size of the rod was fixed at the physical diameter in the expression for q, Eq. (7.31). The diffusion constant inside the object can be neglected with respect to the surrounding medium, $D_2 \ll D_1$, and the dipole contribution, which is s^2/L^2 times smaller than the charge term, is also neglected. All theoretical curves are convoluted with the experimental spatial resolution. The agreement between measured and calculated profiles is excellent. We derive from the fits the positions of the objects; the minimum (or maximum) gives us the y-position, the width of the profile reflects the depth (z-position) of the object.

In Fig. 7 we plot the values for the positions of the absorbent rod obtained from the numerical fits of Eq. (7.32) to the measured line shapes, as a function of the experimental positions. The data points are on a straight line with slope one, variations are less than 100 μm. However, there is a clear offset. An explanation for this offset can be found in experimental errors that are still present even after careful alignment of the optical components. Image faults of the intensity profile on the diode-array are caused by the lens but also by a small misalignment of the rod with respect to the diode-array. Reflection inside the 20 mm thick windows will still give a slight deformation of the intensity profile. All these effects smear out the intensity profile, and therefore the apparent position of the object will correspond to a deeper (z_0 smaller) position inside the slab than the real position.

Using the strength of the intensity profile, peak height relative to the background, one can derive the 'charge' of the rod, and from the charge one should be able to recover the size of the rod. The charge depends also on the unknown absorption parameter α. Only for very black materials, which are hard to find in a tractable shape, this minimum value becomes independent of α. However, an experimental investigation of the size dependence of the 'charge strength' is difficult, because the charge depends logarithmically on the size.

In Fig. 8 we plot the minima of the intensity profiles as a function of the fitted normal position of the absorbent rod. The solid line is obtained from Eq. (7.32), using $D_1/\alpha s = 1.00 \pm 0.03$ as the best overall value for the absorption strength. We see a good correspondence between the measured and calculated minima of the intensity profiles as a function of the normal position. Taking also the size of the rod as a free fitting parameter, one obtains the following values: $D_1/\alpha s = 2.15 \pm 0.03$, $s = 0.52 \pm 0.04$ mm. When the experimental instead of the fitted positions are used, one obtains: $D_1/\alpha s = 0.50 \pm 0.03$, $s = 0.075 \pm 0.04$ mm. Note that the strength of the charge gives the minimum possible size of the object, because a finite absorption length will always decrease the strength.

In Table 7.1 displacements parallel to the slab are compared with those obtained from the corresponding fits of Eq. (7.32) to the measured line shape. The transversal position can be determined with an accuracy of 20 μm, even if the rod is placed far from the boundaries. The slight disagreement between the real position and the position obtained from the fits in Table 7.1 is mainly due to the curved focal surface of the lens used.

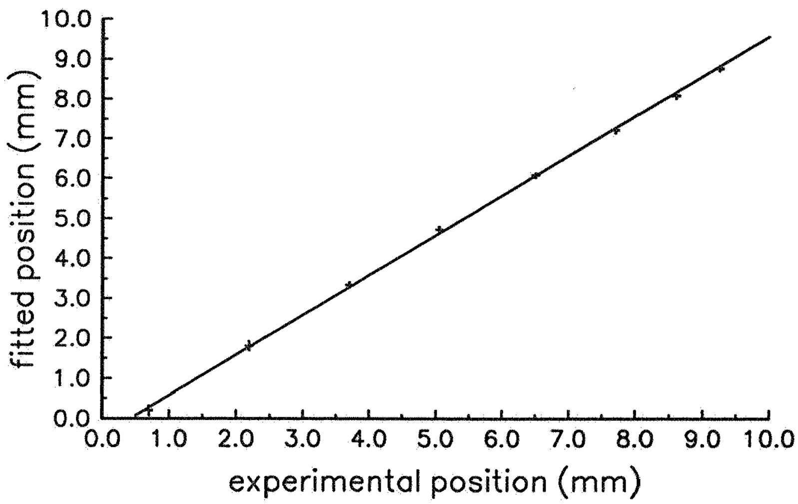

Figure 7: Measured positions as a function of the real positions. Data obtained from a transmission experiment with an absorbent rod (s=0.175 mm). The scattering contribution is neglected, $p = 0$, and the diffusion constant inside the rod $D_2 \ll D_1$ for all points. The absorption parameter α was used as a free fitting parameter.

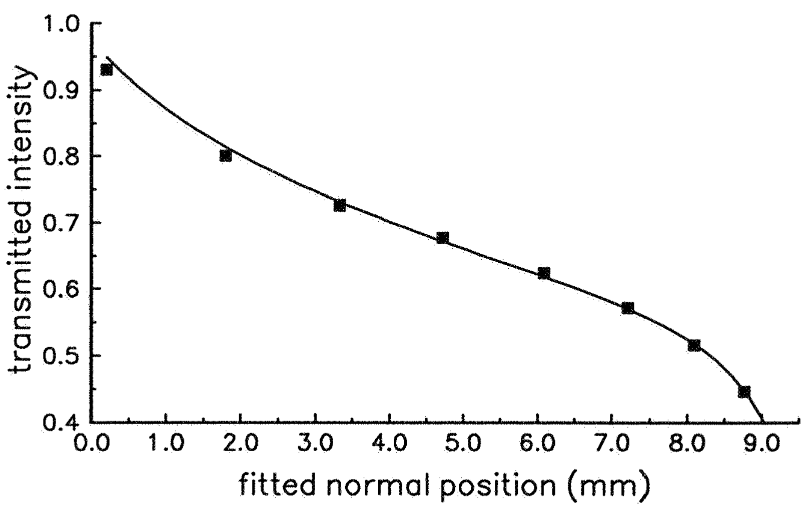

Figure 8: Measured minima of the intensity profiles for a number of normal positions of the absorbent rod. Solid line: calculation using Eq. (7.32), with L = 10.0 mm, s = 0.175 mm, $D_1/\alpha s$ = 1.00, and $p = D_2 = 0$.

In Fig. 9 we plot the transmitted intensity profiles for a transparent fiber, s=0.175 mm, in cell with thickness 5.0 mm for two different normal positions. Clearly we see the dipole behaviour in the disturbance of the transmitted intensity. However, it turned out that no good fits could be made without absorption present. That the glass fiber can act as an absorber can be understood by considering the

real displacement (mm)	recovered displacement (mm)
2.00 ± 0.02	2.05 ± 0.03
4.00 ± 0.02	4.04 ± 0.06
5.00 ± 0.02	5.02 ± 0.07
7.00 ± 0.02	7.03 ± 0.09
9.00 ± 0.02	9.1 ± 0.1
11.00 ± 0.02	11.1 ± 0.2

Table 7.1: Displacement of an absorbent rod parallel to the slab: z_0=6.70±0.02 mm, L=10.0 mm. For all cases: $D_1/\alpha s$=1.4 ±0.1 (relative absorption strength) and $p = D_2 = 0$.

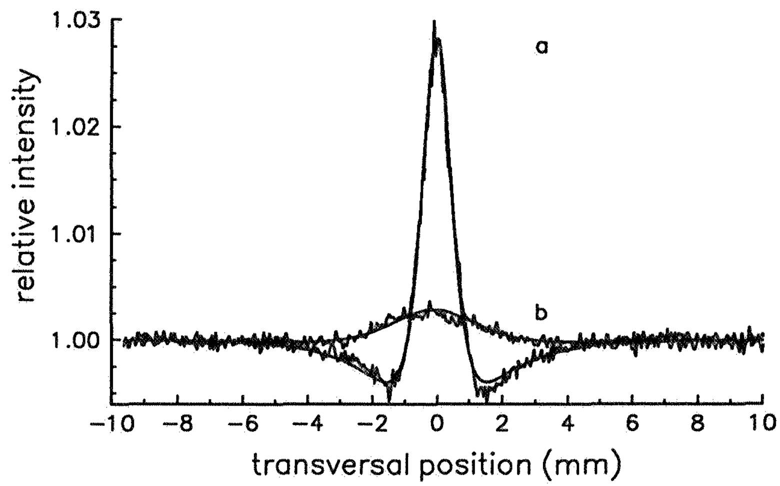

Figure 9: Position resolved transmitted intensity of a scattering suspension with a transparent fiber $s = 0.175$ mm at normal positions: a) $z_0 = 4.26 \pm 0.05$, b) $z_0 = 2.5mm$; $l_{tr} = 20\pm3$ μm, $L = 5.0$ mm. Experimental data are shown together with the best numerical fits of Eq. (7.32); a) $z_0 = 4.40 \pm 0.02$ mm, $D_2 = \infty$, $D_1/\alpha s = 1 \cdot 10^2$. b) $z_0 = 2.6 \pm 0.1$ mm, $D_2 = \infty$, $D_1/\alpha s = 1 \cdot 10^2$.

finiteness of the sample. In reality the fiber acts as a sink: once inside the fiber, the light can easily escape the sample by leaking out through the top or the bottom of the cell. During the experiments, a bright spot was clearly visible at the top of the fiber.

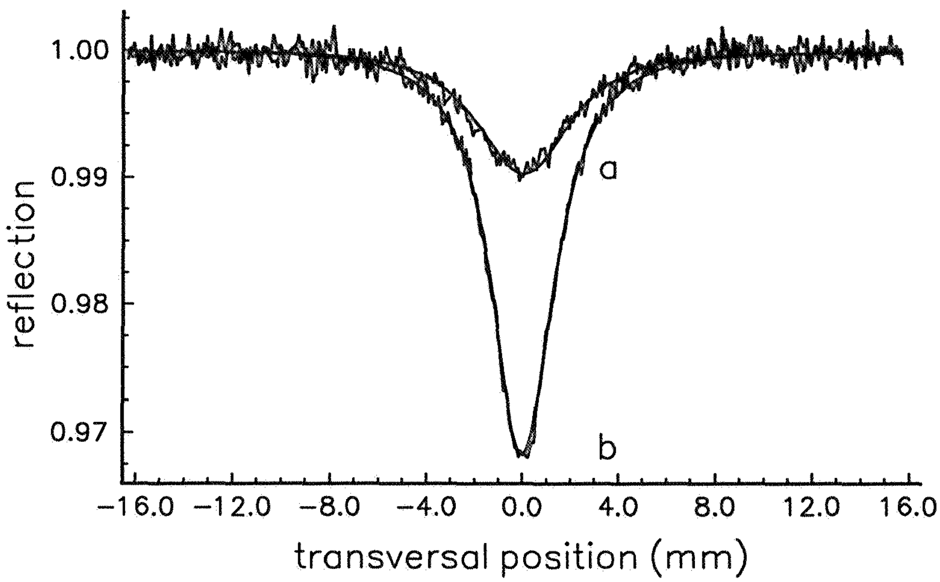

Figure 10: Reflected intensity of an absorbent wire $s = 0.175$ *mm* inside a scattering suspension at different positions: a) z_0=1.68 *mm*, b) z_0=0.78 *mm*. Transport mean-free path $l_{tr} = 47 \pm 3$ μm, thickness cuvette $L = 4.0$ *mm*. Experimental data are shown together with numerical fits of Eq. (7.33) to the experimental data, see also Table 7.2.

7.4.2 Reflection and point source measurements

In reflection we consider only absorbent rods, since the expected disturbance due to the object is small compared to the total reflected intensity from the slab. We use a 0.3 *mm* pencil embedded in a scattering suspension with a transport mean-free path of 47 ± 3 μm; the cell with the 4 *mm* windows was used. Transmission experiments on absorbent objects suffer most from this blurring effect, because the intensity profile relative to the background is the largest.

Results are shown in Fig. 10 together with the best numerical fits. The shape of the experimentally observed intensity profiles is excellently reproduced by the calculations. The transversal position can be determined with an accuracy of 20 μm. The values for the z-positions of the rod, obtained from the fits, are shown in Table 7.2 and are compared with the experimental positions.

To get an idea about the sensitivity of the profile on the position of the rod, we took two successive scans with a normal displacement of the rod of 50 ± 2 μm as the only difference. The measurement excellently recovers the displacement, the fits of the two successive scans give a displacement of the object of 48 ± 3 μm. This result is shown in the lowest line row of Table 7.2.

The last figure, Fig 11, shows the profile of the transmitted intensity of a

real position (mm)	recovered position (mm)	absorption strength $D_1/\alpha s$
0.28 ± 0.05	0.34 ± 0.02	0.5 ± 0.1
0.78 ± 0.05	0.82 ± 0.02	0.6 ± 0.1
1.38 ± 0.05	1.32 ± 0.02	2.0 ± 0.1
1.68 ± 0.05	1.7 ± 0.1	1.7 ± 0.1
$\Delta z_0 = 50 \pm 5\ \mu m$	$\Delta z_0 = 48 \pm 3\ \mu m$	

Table 7.2: Normal positions of a rod (s=0.175 mm) compared with positions recovered from backscatter measurements. Last line: small displacements of the rod (at z_0=0.650 mm and z_0=0.655 mm). Parameters taken for fits: L=4 mm, $p = 0$, $D_2 = 0$.

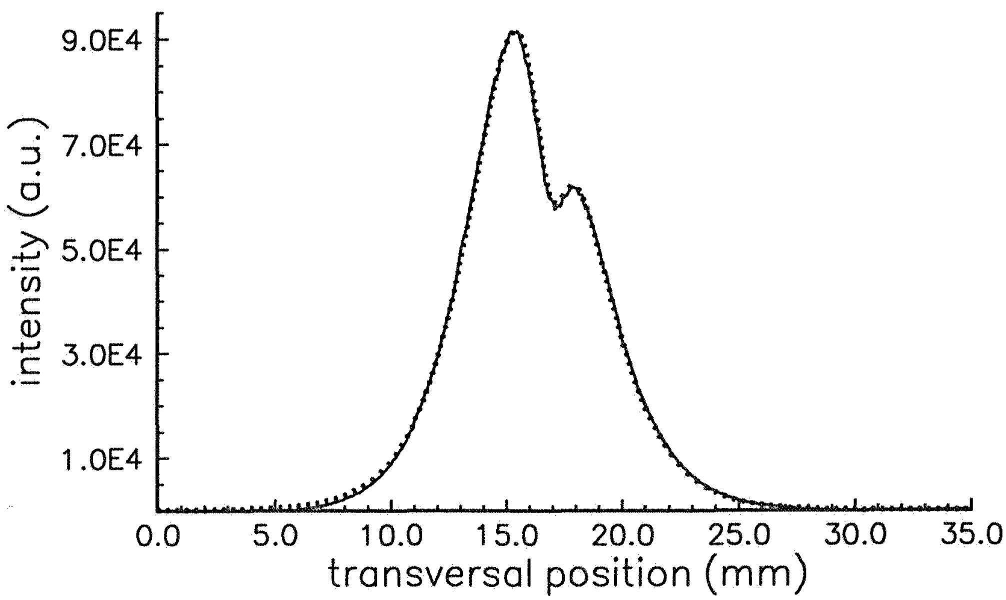

Figure 11: Transmission profile of an absorbent rod (s = 0.175 mm) embedded by a scattering medium, $l_{tr} = 20 \pm 3\mu m$, L = 5.0 mm. A line source is used instead of a plane wave. Normal position of rod: $z_0 = 4.95 \pm 0.05\ mm$. Numerical fit (dotted line), derived from Eq. (7.36), yields $z_0 = 4.97 \pm 0.02 mm$.

5 *mm* thick sample when a line source is used. An absorbent rod is positioned besides the source. The fit is obtained by taking the derivative of Eq. (7.36) at the boundary of the slab, so the transmitted intensity profile is obtained. The strength of the light source is varied to give an optimal match to the envelope of the intensity profile. To accomplish the fit, besides the position of the object, the absorption strength is also fitted.

7.5 Conclusion

We have considered the situation of a single object embedded in a diffusely scattering medium confined in a simple geometry. The disturbance of the diffuse intensity can be expressed in a multipole expansion. The intensity profile of the multipoles is completely determined by the dimensions of the scattering medium. Thus, a small object gives a broad profile as a result of diffusional broadening. The scattering properties and shape of the object determine the magnitude of the multipoles. Every sequel multipole contribution is $(s/L)^{d-1}$ times smaller than the previous one, where d is the dimensionality of the geometry containing the scattering medium. Since s/L is small, only one multipole is usually seen in the intensity disturbance. As a consequence, it is not feasible to obtain the shape of the object from the diffuse light. For absorbent objects, one can always obtain a minimum possible size from the strength of the charge term. An estimate of the size *and* absorption strength can be made when the transmitted intensity can be recorded for various normal positions of the object inside a slab.

The calculated profiles are in excellent agreement with the measured profiles. Therefore one can recover very small displacements of the object in an arbitrary direction. Very small means an order of magnitude smaller than the dimensions of the scattering medium. The transversal position determination in a slab becomes rather simple, the absolute normal position determination is influenced by experimental errors and is less accurate.

References

[1] S.R. Arridge, M. Cope, P van der Zee, P.J. Hilson and D.T. Delpy, *Visualization of the oxygenation state of brain and muscle in newborn infants by near infra-red transillumination*, Inf. Proc. Med. Imag. 155 (Nijhoff, The Netherlands, 1985).

[2] J. Fishkin, E. Gratton, M.J. van de Ven, and W.W. Mantulin, *Diffusion of intensity modulated near-infrared light in turbid media*, Proc. Time. Res. Spec. and Imag. (SPIE, Los Angeles) (1991).

[3] E.M. Sevick, B. Chance, J. Leigh, S. Nioka, and M. Maris '*Quantisation of time- and frequency-resolved optical spectra for the determination of tissue oxygenation*, Anal. bioch. **195**, 330 (1991).

[4] H. Chen, Y. Chen, D. Dilworth, E. Leith, J. Lopez, and J. aldmanis, '*Two-dimensional imaging through diffusing media using 150-fs gated electronic holography techniques*, Opt. Lett. **16**, 487 (1991).

[5] Conference on Lasers and Electro-Optics 1991 (CLEO'91), session *Biomedical Imaging.*, CTUH1-5, 101-104 Technical Digest.

[6] E.N. Leith, C. Chen, H. Chen Y. Chen, J. Lopez, and P.C. Sun, *Imaging through scattering media using spatial incoherence techniques*, Opt. Lett. **16**, 1820 (1991).

[7] K.M. Yoo, Qirong Xing, and R.R. Alfano, *Imaging objects hidden in highly scattering media using femtosecond-harmonic-generation cross-correlation time gating*, Opt. Lett. **16**, 1019 (1991).

[8] R. Berkovits and S. Feng, *Theory of speckle-pattern tomography in multiple-scattering media*, Phys. Rev. Lett. **65**, 3120 (1990).

[9] I. Freund, *Image reconstruction through multiple scattering media*, Opt. Comm. **86**, 216 (1991).

[10] Th. M. Nieuwenhuizen and M. C. W. van Rossum, *Role of a single scatter in multiple scattering media*, Phys. Lett. A **177**, 102 (1993).

[11] *see for instance*, J. W. Goodman, 'Statistical optics', (Wiley, New York, 1985).

[12] E. Akkermans, P.E. Wolf, and R. Maynard, *Coherent backscattering of light by disordered media: analysis of the peak line shape*, Phys. Rev. Lett. **56**, 1471 (1986).

[13] *see for instance*, J.D. Jackson, 'Classical Electrodynamics', (Wiley, New York, 1975).

[14] Th. M. Nieuwenhuizen and J.M. Luck, *Skin layer of diffusive media*, Phys. Rev. E. **48**, 569 (1993).

Samenvatting

De lichtverstrooiende eigyenschappen van een deeltje of korrel worden in het algemeen bepaald door de (complexe) brekingsindex, vorm en grootte van de korrel ten opzichte van de golflengte van het licht. Wanneer we nu veel korrels wanordelijk plaatsen in de ruimte, creeëren we een medium waarin het licht door het hoog aantal verstrooiingen zal diffunderen. Alleen op korte afstand is er nog een aanzienlijke bijdrage van het niet verstrooide licht. Wanneer de korrels een reële brekingsindex hebben, wordt het licht alleen verstrooid en niet geabsorbeerd. Zo'n medium ziet er uit als witte verf.

In eerste instantie lijkt voor een situatie waar licht veelvuldig en op willekeurige plaatsen verstrooid wordt, interferentie onbelangrijk voor de beschrijving van het licht. Het bestaan van laserspikkel, een wanordelijk interferentie (!) patroon, is echter al een sterk tegenvoorbeeld. Een ander interferentie effect van veelvoudig verstrooid licht is juist alleen waarneembaar na een middeling over vele spikkelpatronen of wanneer we het wanordelijk medium beschijnen met een goed gecollimeerde bundel wit licht. De gereflecteerde intensiteit zal dan verhoogd zijn rond de exacte terugstrooirichting (de richting tegengesteld aan die van het invallend licht). Dit is als volgt in te zien: wanneer we een wanordelijk medium beschijnen met een vlakke lichtbundel zullen lichtgolven het medium indringen en tenslotte, via een meestal groot aantal verstrooiingen, gereflecteerd worden. Een lichtgolf heeft een wanordelijke wandeling gemaakt in het medium en daardoor een bepaalde wanordelijke fasedraaiing ondergaan. Omdat we het medium beschijnen met een vlakke bundel, is er ook een tegengestelde golf die hetzelfde pad bewandelt maar in de omgekeerde richting. Deze golf ondergaat dus precies dezelfde fasedraaiing. Het fase*verschil* tussen deze twee golven is onafhankelijk van de vorm en aantal verstrooiingen in het pad zolang begin- en eindpunt van het pad hetzelfde blijven. De gereflecteerde intensiteit van een wanordelijk medium wordt dus opgebouwd uit paarsgewijs interfererende puntbronnen op willekeurige afstanden. Alleen in de exacte terugstrooirichting geldt dat voor alle gepaarde puntbronnen de interferentie constructief is, en in die richting zal de gereflecteerde intensiteit het grootst zijn. Voor richtingen die een hoek maken met de terugstrooirichting, zullen de interferentie patronen van de puntbronnen elkaar uitmiddelen. De interferentie geeft aanleiding tot een typerende vorm van de gereflecteerde intensiteit, namelijk een kegelvorm. Dit interferentie effect wordt om deze reden de terugstrooikegel genoemd.

De kans op een bepaalde afstand tussen twee puntbronnen zal afhangen van het medium; naarmate het een optisch dichter medium betreft, zal deze afstand gemiddeld genomen kleiner zijn en dus de terugstrooikegel breder. In de experimenten beschreven in dit proefschrift is vaak de vorm of hoekbreedte van de terugstrooikegel gebruikt om informatie te verkrijgen over het wanordelijk medium en over de propagatie van het licht door het medium.

In **hoofdstuk 2** bespreken we eerst lichtverstrooiing aan één korrel, en daarna geven we een introductie op de veelvoudige verstrooiingstheorie.

Voor metingen aan wanordelijke media is een opstelling gebouwd met een hoekoplossendvermogen van $50\mu rad$. Als lichtbron wordt een nauwbandige kleurstof-laser gebruikt. Dit wordt beschreven in **hoofdstuk 3**. Ook zullen we ingaan op de specifieke experimentele moeilijkheden die zich voor doen bij metingen aan veelvoudig verstrooiende media rond de terugstrooirichting.

Hoofdstuk 4 handelt over een aantal korte experimenten. We hebben de invloed van polarisatie op het veelvoudig verstrooide licht en op de mogelijkheid om nieuwe interferentie verschijnselen waar te nemen onderzocht. In ditzelfde hoofdstuk laten we zien dat het doorgelaten licht van een wanordelijke medium gepolariseerd is. De polarisatiegraad is groter naar mate het oppervlak van het wanordelijk medium gladder is.

Doordat in het wanordelijk medium het licht veelvoudig verstrooid wordt, is niet meteen duidelijk hoe de effectieve brekingsindex van het wanordelijke medium uitgerekend moet worden en hoe die experimenteel bepaald kan worden. De effectieve brekingsindex zal in ieder geval verschillen met die van lucht. Het licht, dat het wanordelijk medium verlaat, zal daardoor intern gereflecteerd worden. Hoe hoger de effectieve brekingsindex, hoe groter de interne reflectie zullen zijn. In **hoofdstuk 5** gaan we in op de invloed van deze interne reflecties op de diffuse lichtintensiteit. We hebben experimenten gedaan waarbij we het verschil in brekingsindex tussen het verstrooiend en het niet-verstrooiend medium gevarieerd hebben om zo de invloed van interne reflecties op de breedte van de terugstrooikegel experimenteel te bepalen. Uit vergelijking met theoretische modellen, die de invloed van interne reflectie beschrijven, volgt de effectieve brekingsindex van het wanordelijk medium. Het blijkt dat we op deze manier veel lagere waarden voor de effectieve brekingsindex vinden dan we zouden verwachten op grond van gemiddelde-veld-theorieën. Brewsterhoek-metingen aan wanordelijke media bevestigen echter dat deze lage waarden voor de effectieve brekingsindex reëel zijn.

In **hoofdstuk 6** beschrijven we experimenten en simulaties die we hebben uitgevoerd om de invloed van anisotrope strooiing op het transportgedrag van het licht door het wanordelijke medium nader te onderzoeken. De eenvoudigste benadering, die ook meestal gebruikt wordt, is de introductie van een grotere lengte schaal waarop de diffusie dan plaatsvindt. In die beschrijving van de diffuse lichtintensiteit wordt er nog steeds van uitgegaan dat elke verstrooiing isotroop is, in werkelijkheid is zo'n fictieve isotrope verstrooiing een aantal verstrooiingen dat samen een isotrope karakter vormt. Dit is een zeer goede benadering wanneer het gemiddeld aantal verstrooiingen hoog is. In reflectie en tijdopgeloste transmissie metingen zijn echter bepaalde belangrijke bijdragen alleen afkomstig van de lage orde verstrooiingsprocessen. Voor reflectie metingen weerspiegelt zich dit in de vorm van de terugstrooikegel. In tijdopgeloste transmissie meting zijn dit de lichtgolven die het medium in bijna rechte lijnen doorkruisen; deze golven zullen in een transmissie experiment als eerste worden gedetecteerd. Om deze lage orde verstrooiingsprocessen goed te beschrijven blijkt er een andere aanpak dan hierboven geschetst noodzakelijk te zijn.

In het laatste hoofdstuk, **hoofdstuk 7**, gaan we in op een toegepast onderwerp dat te maken heeft met het afbeelden van voorwerpen door veelvoudig verstrooiende media. De afwezigheid van rechtlijnige voortplanting van het licht maakt het mogelijk voorwerpen te verstoppen in een veelvuldig verstrooiend medium. Dit is niets anders dan dat de hoeveelheid vruchtjes in de yoghurt een verrassing zal zijn. Toch blijkt zo'n ingesloten voorwerp niet onvindbaar (zonder in de yoghurt te lepelen). Het voorwerp heeft namelijk andere optische eigenschappen dan het omringende verstrooiend medium en zal daardoor de diffuse lichtintensiteit in dit omringende medium verstoren. De verstoring zal weer diffunderen naar de randen van het verstrooiend medium, en kan daar gemeten worden. Wij hebben onderzocht welke informatie over het voorwerp nog via een dergelijke meting achterhaald kan worden door een theoretisch model op te zetten dat het lichttransport door zowel het omringende verstrooiend medium als door het voorwerp beschrijft met behulp van de diffusietheorie. Dit theoretisch model lijkt sterk op een elektrostatisch probleem waar het elektrisch veld uitgerekend moet worden voor een gegeven configuratie van geleiders, ladingen, diëlektrica en potentialen. Het model is in goede overeenstemming met de uitgevoerde experimenten waarbij de gereflecteerde of doorgelaten lichtintensiteit is gemeten. Hierdoor kunnen we de plaats van een voorwerp in het veelvoudig verstrooiende medium nauwkeurig bepalen, en uiterst kleine verplaatsingen van het voorwerp waarnemen.

Nawoord

Na de laatste loodjes is het nu tijd om de mensen binnen en buiten de groep 'spectroscopie van de verdichte materie' te bedanken die mij terzijde hebben gestaan en wiens hulp onontbeerlijk is geweest voor de totstandkoming van dit proefschrift. Om niet elke keer in herhaling te vallen zal ik de woorden 'wil ik bedanken voor' te pas en te onpas weglaten.

Allereerst wil ik mijn promotor Ad Lagendijk bedanken. Ik heb veel van je geleerd zowel op een fysisch vlak als daarbuiten. De heldere manier waarop jij bekende formules uit kan leggen maakt de fysica een wonder schone zaak. Ik heb geprobeerd deze heldere kijk van je over te nemen, ik hoop dat ik daar een beetje in geslaagd ben. Meint van Albada heeft meestal als eerste door wat er nu daadwerkelijk gemeten wordt, of welk experiment er *eigenlijk* zou moeten plaatsvinden. Je kennis over het onderwerp is groot, hiervan heb ik veel profijt gehad. Meint, ik ben je zeer erkentelijk voor je directe en indirecte bijdragen aan dit proefschrift. Theo Nieuwenhuizen was altijd bereid mij nog eens het een en ander uit te leggen over veelvuldige verstrooiing van licht. Dit beviel je kennelijk zo goed dat je besloten had maar een geheel college plus dictaat te verzorgen. Het succes van hoofdstuk 7 is voor een groot deel aan jou te danken geweest. Voor experimentele problemen die om een suggestie vroegen die verder gingen dan 'controleer de aan/uit knop' kon ik altijd terecht bij Rudolf Sprik. Ook voor nijpende algemeen theoretische vraagstukken bleek je een uiterst complete vraagbaak. Mijn voorganger Martin van de Mark wil ik bedanken voor het schrijven van zijn proefschrift 'Propagation of light in disordered media: a search for Anderson localization'. Geheel toevallig bleek juist dit proefschrift voor mij erg nuttige informatie te bevatten, ik heb het dan ook letterlijk stukgelezen. Jouw gedreven manier van praten over licht verstrooiing had op mij een zeer enthousiasmerende uitwerking. Peter Molenaar heeft mij geïntroducteerd in de veelvuldig verstrooiingsexperimenten, en heeft samen met mij de Brewsterhoekmeting uitgevoerd. Het zal hem enigszins verbazen dat deze metingen toch nog consistentie vertonen met andere experimenten.

Voor de technische en administratieve ondersteuning bedank ik Harry Beukers, Ad Wijkstra, Ron Manuputy, Willem Martijn, Eddy Inoeng, Bert Zwart, Flip de Leeuw, Ton Jongeneelen, Paul Langemeijer, Ton Riemersma, Hugo Schlatter, Mariet Bos, Ineke Weijer, Ina Zwart, en Klaas van Paasschen. Michiel Groeneveld wil ik bedanken voor de vervaardiging van de glasvensters en het polijsten van een cuvette. Tenslotte Wim Koops voor het onderhoud van de lasers, de haastklusjes tussendoor, en de andere taken die je binnen de groep op je genomen hebt.

A, B, B, C, F, G, H, H, I, J, J, J, M, M, M, M, M, M, M, P, P, P, R, R, R, R, T, T, W, hebben door de groepsbesprekingen, AIO/OIO-nachten, 'No mercy productions', o ja, interessante tafel DISCUSSIES zowel over het dagelijks leven als over het werk en wat voor een onzin nog meer, een geheel eigen karakter gegeven aan mijn promotietijd. Heren en dames, ik dank u feestelijk en veel succes in het verdere leven!

M'n H27uisgenootjes hebben veel interesse getoond in mijn dagelijkse besognes en hierop een relativerende uitwerking gehad. Birgit and Matthew hebben veelvuldig vreemd taalgebruik in mijn schrijven weggepoetst of opgelapt. Karin van Beers bedank ik voor de grafische vormgeving van de omslag.

Tenslotte wil ik Susana, Karen en Frank bedanken voor hun steun en hun niet aflatende vertrouwen in mij en in het welslagen van dit project.